

ABSTRACT

Title of Dissertation: SOLAR NEUTRINOS
AT SUPER-KAMIOKANDE:
SOLVING THE SOLAR NEUTRINO PUZZLE
VIA NEUTRINO FLAVOR OSCILLATIONS

Dušan Turčan, Doctor of Philosophy, 2003

Dissertation directed by: Professor Gregory W. Sullivan
Department of Physics

The Super-Kamiokande neutrino detector was built with the intent to explain the long-standing apparent solar neutrino flux deficit through signatures of neutrino flavor oscillations, such as a distortion in the energy spectrum and an asymmetry in the day and night fluxes. With the absence of any such “smoking-gun” evidence, an oscillation analysis of solar neutrinos was performed using the data sample from Super-Kamiokande I (SK), Sudbury Neutrino Observatory (SNO), and all other neutrino detectors. A model-independent analysis of SK’s total solar neutrino rate and SNO’s solar electron-neutrino rate showed at 3.7σ level that the apparent deficit is due to the effects of neutrino flavor oscillations. This analysis was possible because for a careful choice of energy thresholds, SK and SNO have virtually the same response to ${}^8\text{B}$ solar neutrinos, whose energy spectrum is undistorted, as demonstrated by the data. By utilizing the full data sets of SK and SNO, however, the oscillation scenario is favored at 6.0σ level, with the best-fit oscillation parameters of $\Delta m^2 = 6.3 \times 10^{-5} \text{ eV}^2$ and $\tan^2\theta = 0.44$ (in the LMA region). The measured ${}^8\text{B}$ neutrino flux is $\Phi_\nu = 5.45_{-0.69}^{+0.64} \times 10^6 \text{ cm}^{-2}\text{s}^{-1}$, which confirms its theoretical prediction

from the Standard Solar Model. With the addition of the neutrino rates from the radiochemical experiments (gallium and chlorine), and the anti-neutrino oscillation result from KamLAND, the LMA solution is further constricted, the ^8B neutrino flux is again confirmed ($\Phi_\nu = 5.66_{-0.59}^{+0.62} \times 10^6 \text{ cm}^{-2}\text{s}^{-1}$), and the no-oscillation scenario is ruled out at more than 10σ level.

SOLAR NEUTRINOS
AT SUPER-KAMIOKANDE:
SOLVING THE SOLAR NEUTRINO PUZZLE
VIA NEUTRINO FLAVOR OSCILLATIONS

by

Dušan Turčan

Dissertation submitted to the Faculty of the Graduate School of the
University of Maryland, College Park in partial fulfillment
of the requirements for the degree of
Doctor of Philosophy
2003

Advisory Committee:

Professor Gregory W. Sullivan, Chairman/Advisor
Professor Jordan A. Goodman
Professor Abolhassan Jawahary
Professor Rabindra N. Mohapatra
Professor Andrew S. Wilson

© Copyright by

Dušan Turčan

2003

DEDICATION

To my parents and to the glory of God

ACKNOWLEDGEMENTS

Completing the physics graduate program, which culminated in the present dissertation, has been the biggest accomplishment of my life. It has required much effort and self-motivation, many sacrifices and adjustments. As much as it is my personal accomplishment, it is clear, however, that I could not have done it alone. With this realization, first and foremost, I want to thank God for getting me through this important stage of my life, and helping me grow. It was primarily through faith in him and his promises that I have completed the doctorate with as much enthusiasm and confidence as I did.

I also want to extend wholehearted gratitude to my advisor, Prof. Greg Sullivan. His help, encouragement, guidance, trust, and patience have been instrumental in my work and its completion. By demanding high standards while leaving enough freedom for personal research interests, he has been the best advisor I could wish for. When my career path leads me to rewarding places, I will know that he provided a large contribution to it.

Besides my advisor, there were numerous colleagues that helped and guided me on my journey toward the completion of this work. As unfair as it may be to all the others, I feel compelled to single out Dr. Michael Smy, Dr. Yusuke Koshio, and Dr. Yasuo Takeuchi, and thank them for a huge contribution they have made in my education and accomplishment.

It was also through a tremendous support from my close friends that I was able to complete my doctorate. Therefore, I want to thank Jonathan Ozik, Jonathan Tuminaro, Bram Lillard, Adrienne Anderson, Safraz Ishmael, Tobias Durkop, David Rupke, and David Noyes for loving me, encouraging me, supporting me, helping me, and not letting me quit. I am greatly indebted to them all and many others.

Finally, I want to thank my parents, Dušan and Viera, and my sister, Ľudmila, for their endless love and faith in me, and for providing me with opportunities in life.

TABLE OF CONTENTS

List of Tables	viii
List of Figures	ix
1 Introduction	1
1.1 Motivation for Neutrino Mass	2
2 Solar Neutrinos	5
2.1 Overview of the SSM	5
2.2 History of the Solar Neutrino Deficit	10
2.2.1 Chlorine Experiment	10
2.2.2 Kamiokande Experiment	11
2.2.3 Gallium Experiments	12
2.2.4 Neutrino Deficit	13
2.3 The Theory of Neutrino Oscillations	15
2.3.1 Two-Flavor Oscillations in Vacuum	17
2.3.2 Oscillations in Matter: MSW Effect	18
2.3.3 Regeneration in the Earth (MSW)	20
2.4 Solution of the Solar Neutrino Deficit	21
3 Super-Kamiokande Detector	24
3.1 Neutrino Detection Method	27

3.2	Description of the SK detector	30
3.2.1	Detector Overview	30
3.2.2	Water and air purification systems	33
3.2.3	Photomultiplier Tubes	33
3.2.4	DAQ electronics	37
3.2.5	Triggers	41
3.3	Calibration of the SK detector	44
3.3.1	PMT calibration	45
3.3.2	Water Transparency Calibration	46
3.3.3	Energy/Position/Direction Calibration	50
3.3.4	Trigger Efficiency Calibration	60
4	Solar Neutrino Signal Extraction at SK	62
4.1	Event Reconstruction	62
4.1.1	Vertex Reconstruction	63
4.1.2	Direction Reconstruction	64
4.1.3	Energy Reconstruction	66
4.1.4	Muon Track Reconstruction	70
4.1.5	SLE Reconstruction Tools	70
4.2	Data Reduction	74
4.2.1	Organization of the Data	75
4.2.2	First Reduction	75
4.2.3	Removal of Spallation Events	80
4.2.4	Second Reduction	83
4.2.5	Final Data Sample	86
4.3	Simulation of Solar Neutrino Events	89
4.3.1	Neutrino Interaction Simulation	89
4.3.2	Detector Response Simulation	95

4.4	Signal Extraction Method	100
4.4.1	Likelihood Fitting	100
4.4.2	Summary of SK Signal Measurements	103
4.4.3	Systematic Uncertainties	107
5	Solar Neutrino Oscillation Analysis	117
5.1	Introduction	117
5.1.1	Overview of SNO	118
5.2	Model-Independent Analysis	119
5.2.1	Detector Response Function Equivalence	120
5.2.2	Flux Data Extraction	122
5.2.3	Results of the Fit	123
5.3	Full, Model-Dependent Analysis	126
5.3.1	Detector Response Functions	127
5.3.2	Oscillation Predictions and Data Measurements	128
5.3.3	SK Fit Results	132
5.3.4	SK+SNO Fit Results	136
5.3.5	Global Fit Result	140
5.3.6	Adding the KamLAND Rate	140
5.3.7	Final Solar Neutrino Oscillation Result	144
6	Summary and Conclusions	149
	Bibliography	152

LIST OF TABLES

2.1	Observed solar parameters	5
2.2	SSM neutrino flux predictions	9
2.3	Measured solar neutrino deficit	14
3.1	SK triggers	25
3.2	SK triggers	42
3.3	Energy, position, and direction resolutions	54
4.1	SK recoil electron energy spectrum	111
4.2	Systematic uncertainties in the energy spectrum	116
5.1	SNO energy spectrum	131
5.2	Solar neutrino flux deficit solved	147

LIST OF FIGURES

2.1	The solar pp chain	7
2.2	The solar CNO chain	7
2.3	Energy spectra of pp chain solar neutrinos	8
2.4	Neutrino oscillation solutions from radiochemical experiments	22
3.1	Energy spectrum distortions of the four oscillation solutions	26
3.2	Cherenkov ring pattern	29
3.3	Super-Kamiokande detector	30
3.4	PMT mounting	31
3.5	Water purification system	34
3.6	Air purification system	34
3.7	Inner detector	36
3.8	ADC histogram of an ID PMT	36
3.9	Quantum efficiency of an ID PMT	37
3.10	Inner detector DAQ system	39
3.11	Water transparency calibration setup	47
3.12	Attenuation length of Cherenkov light	48
3.13	Long term variations of the attenuation length	49
3.14	Fit to the attenuation length measurements	50
3.15	LINAC calibration system	51
3.16	Reconstructed energy distributions for LINAC	53

3.17 DTG setup	55
3.18 DTG energy calibration	57
3.19 Position dependence of the energy scale	58
3.20 Azimuthal and zenith angle dependence of the energy scale	58
3.21 Stability of the energy scale	59
3.22 Zenith angle dependence of the energy scale	60
3.23 Trigger efficiency	61
4.1 Neutrino candidate event selection process	64
4.2 Goodness of fit	65
4.3 Cherenkov photon direction distribution	66
4.4 N_{eff} -to-energy translation function	69
4.5 Clusfit fitter	72
4.6 Clusfit reconstructed vertices	73
4.7 Separation of electron and muon events	76
4.8 Distribution of event times since last event	77
4.9 Distribution of the number of hit OD PMTs	78
4.10 Distributions of the NSratio variable	79
4.11 Distributions of the PMT hits for a flashing event	80
4.12 Muon track likelihood distributions	82
4.13 GRINGO cut	84
4.14 Cherenkov ring cut	85
4.15 Summary of the solar neutrino data reduction	87
4.16 Total neutrino-electron ES cross section	91
4.17 ^8B decay neutrino energy spectrum	92
4.18 $\lambda(E_\nu) \cdot \sigma_{tot}(E_\nu)$ distribution	93
4.19 $\frac{d\sigma(E_\nu)}{dT}$ distribution used for a 12 MeV neutrino	93
4.20 Distribution of ^8B neutrino scattered electrons	94

4.21	The hep neutrino energy spectrum	95
4.22	Tuned light attenuation coefficient	97
4.23	Neutrino-electron ES interaction	98
4.24	Directional distribution of MC simulated events	99
4.25	Probability density function for solar neutrino signal events	101
4.26	Probability density function for solar neutrino background	102
4.27	Likelihood distribution of the signal fraction	104
4.28	The $\cos\theta_{sun}$ distribution of all events	105
4.29	The $\cos\theta_{sun}$ distributions of events between 5.0 and 10.0 MeV	108
4.30	The $\cos\theta_{sun}$ distributions of events between 10.0 and 20.0 MeV	109
4.31	Measured recoil electron energy spectrum	110
4.32	Measured recoil electron energy spectrum normalized by the SSM	110
5.1	SK and SNO detector response functions	122
5.2	Allowed 1σ regions for the SK and SNO separate model-independent flux results	124
5.3	Allowed regions for the combined model-independent SK+SNO flux result	125
5.4	Allowed regions for the solar $\nu_{\mu,\tau}$ flux from the model-independent result	126
5.5	SK energy resolution	128
5.6	SK recoil electron total energy spectral shape used in the analysis	132
5.7	SNO kinetic energy spectral shape used in the analysis	133
5.8	The $\Delta\chi^2$ map for SK model-dependent result	135
5.9	The $\Delta\chi^2$ map for SK+SNO+D/N result	137
5.10	The $\Delta\chi^2$ map for SK+SNO+zenith result	139
5.11	The $\Delta\chi^2$ map for solar neutrino global result	141
5.12	The $\Delta\chi^2$ map of KamLAND rate	142

5.13	The $\Delta\chi^2$ map for the combined KamLAND rate and solar neutrino global fit	143
5.14	The $\Delta\chi^2$ map for total KamLAND fit	144
5.15	Final solar neutrino and reactor anti-neutrino oscillation χ^2 fit	145
5.16	Spectral distortion predictions of the final solar neutrino oscillation model	148

Chapter 1

Introduction

Since their theoretical postulation by Pauli in 1932, neutrinos have been some of the most elusive particles in nature. Little has been known about them, and few neutrino sources have been discovered. There is no obvious place for neutrinos in the standard model, either. They enter into the standard model only as a massless left-handed particle. It is not until we probe beyond the standard model, that massive neutrinos (with both the left-handed *and* the right-handed part) fit naturally into the array of all other known fundamental particles. Therefore, “*looking for neutrino mass is one way of looking for physics beyond the standard model*” [1]. And furthermore, the discovery of neutrino mass has significant implications in cosmology, our understanding of supernovae, as well the thermo-nuclear processes in the sun.

The goal of this work is to present theoretical and experimental aspects of modern neutrino physics, which explain the well-known and long-standing solar neutrino deficit (Sec. 2.2) through neutrino flavor oscillations, using the results from Super-Kamiokande and other neutrino detectors.

The theoretical idea of neutrino flavor oscillations (Sec. 2.3) was first introduced by Pontecorvo in 1957, with analogy to neutral kaon oscillations [1], but strong experimental evidence has only recently emerged. Since the weak interaction cross section for neutrinos is very small (on the order of 10^{-43}cm^2 [1, 2]), it is extremely

difficult to detect neutrino interactions with electrons or nucleons. Therefore, there is a need for very large and expensive detectors, and a long data collection time for evidence to come forth. However, neutrino flavor oscillations are only possible if neutrinos have a finite mass, as described below, in Sec. 2.3.

Using its world's largest underground water Cherenkov neutrino detector, the Super-Kamiokande collaboration has already (1998) reported the first compelling and conclusive evidence for neutrino oscillations ($\nu_\mu \rightarrow \nu_\tau$), and thus evidence for finite neutrino mass, in the sector of atmospheric neutrinos [3]. Most recently, by combining Super-Kamiokande results with results from several other experiments, similarly strong evidence for neutrino oscillations (and non-zero mass) in the solar neutrino sector has rapidly gained credence.

1.1 Motivation for Neutrino Mass

There were several reasons why we believed that neutrinos were massless. On the one hand, they only interact via the weak force, which involves only the left-handed particle fields, and on the other, there has never been a hint of neutrino finite mass in any previous experimental tests. Moreover, for these reasons, the standard model of particle physics was constructed with massless neutrinos with only a left-handed neutrino field. This removes the possibility of a Dirac neutrino mass generation by the Higgs mechanism (which requires fields of both helicities). Even a Majorana mass term (requiring only one helicity state) is not possible for neutrinos in the standard model, because such a term would break lepton number, which is conserved in the standard model, by two units [1]. Because the predictions of the standard model pass numerous extremely rigorous experimental tests, it is difficult to believe that it needs to be changed.

However, another massless particle in the standard model, the photon, implies

a conserved gauge symmetry, which governs the dynamics of the electromagnetic interaction. There is no such symmetry surrounding the neutrinos; therefore the neutrinos' "*masslessness is unsatisfactory from a theoretical point of view*" [1]. On the other hand, a strong argument for believing the Standard Model is that massless neutrinos and one fermion family lead to the desired anomaly cancellations which imply charge quantization. However, if one does indeed introduce a right handed neutrino field and assumes that neutrinos are Majorana particles, the anomaly cancellations still occur and the charge is quantized regardless of the number of fermion families. The conclusion is that massive neutrinos and physics beyond the standard model are necessary. Moreover, many unification models of the fundamental interactions also predict neutrino mass.

Besides these theoretical motivations, a "need" for massive neutrinos also comes from several experimental fields. The pertinent puzzle of the solar neutrino flux deficit can be completely resolved if neutrino flavor oscillations are assumed, which necessitates their finite mass. The atmospheric neutrino flux, asymmetric in the zenith angle, fits well with the predictions from neutrino oscillations, suggesting again a finite mass for neutrinos.

Cosmology would also benefit from the discovery of neutrino mass. Neutrino mass of only a few eV would make a contribution to resolving the *dark matter problem* (the fact that the mass-to-light ratio of large gravitationally bound cosmological systems increases with size of the system). The Big Bang theory predicts relic background neutrinos in such an abundance (8 orders of magnitude more neutrinos than baryons [1]) that a neutrino mass of a few eV could account for a large fraction of the missing mass of the universe.

It is clear, therefore, that massive neutrinos are not only allowed in particle physics, but moreover, are favored and necessary in several different areas. Of nu-

merous experimental tests¹, the idea of neutrino flavor oscillations offers the currently best prospects for demonstrating finite neutrino mass and for explaining the solar neutrino deficit, which is the central focus of this work.

¹Other tests include: nuclear β -decay, pion decay, τ decay, neutrino decays, neutrinoless double β -decay, and search for electromagnetic properties. [1]

Chapter 2

Solar Neutrinos

2.1 Overview of the SSM

One of the most direct ways of learning about neutrinos and their properties is studying their currently only known astrophysical source, the sun. The well-established theoretical model of the sun, the Standard Solar Model (SSM), takes into account properties of the sun that have been independently calculated or measured, and predicts the fluxes of neutrinos produced in various well-known fusion reactions in the sun's core. The main observed solar parameters are presented in Tab. 2.1.

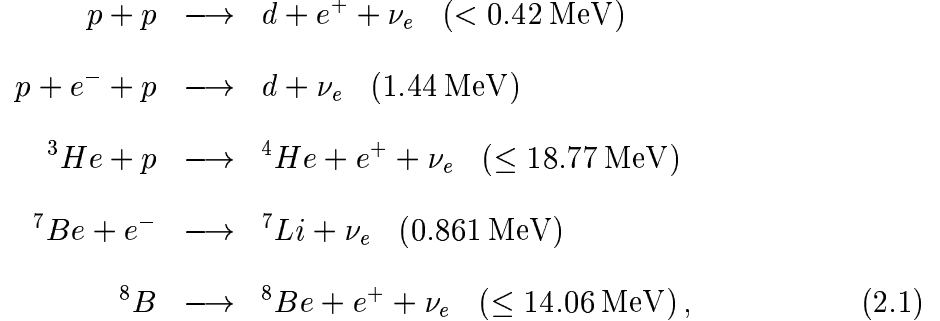
Table 2.1: Observed solar parameters [2, 4].

Parameter	Value
Radius	$(6.96 \pm 0.01) \times 10^8$ m
Mass	$(1.9889 \pm 0.0003) \times 10^{30}$ kg
Luminosity	$(3.84 \pm 0.02) \times 10^{33}$ erg/sec
Age	$(4.57 \pm 0.02) \times 10^9$ yr

The SSM is a solar model constructed with the best currently available physics and experimentally determined input data. The latest in a series of such solar models was created in 2000 by Bahcall and Pinsonneault (BP2000) [4]. In choosing what

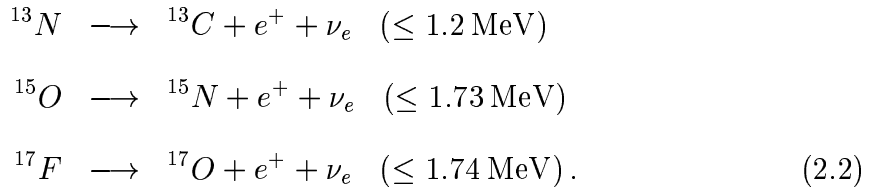
to include in the SSM, the authors required that the predictions “*fit the observed luminosity and radius of the sun at the present epoch, as well as the observed heavy-element-to-hydrogen ratio at the surface of the sun.*” The SSM is then constructed with the OPAL equation of state and opacities, using the present-epoch solar luminosity of 3.842×10^{33} erg/s. The 1σ uncertainties in neutrino flux predictions were calculated by including the published errors in all experimental quantities in all the models and by taking into account of the correlations between different input parameters. This procedure for calculating the uncertainties is described in detail in previous solar model papers by Bahcall et al.[5]. For more details on the current SSM, refer to Ref. [4].

According to the SSM, most of the neutrinos (98.4%) are produced by the pp chain, while the rest (1.6%) are believed to originate in the CNO cycle [4]. The five pp chain reactions responsible for neutrino production are [1]



and correspondingly, there are five types of neutrinos stemming from the pp chain: pp, pep, ${}^7\text{Be}$, ${}^8\text{B}$ and hep neutrinos. The pp chain is illustrated in Fig. 2.1.

The CNO chain, on the other hand, produces ${}^{13}\text{N}$, ${}^{15}\text{O}$, and ${}^{17}\text{F}$ neutrinos:



The CNO chain is shown in Fig. 2.2.

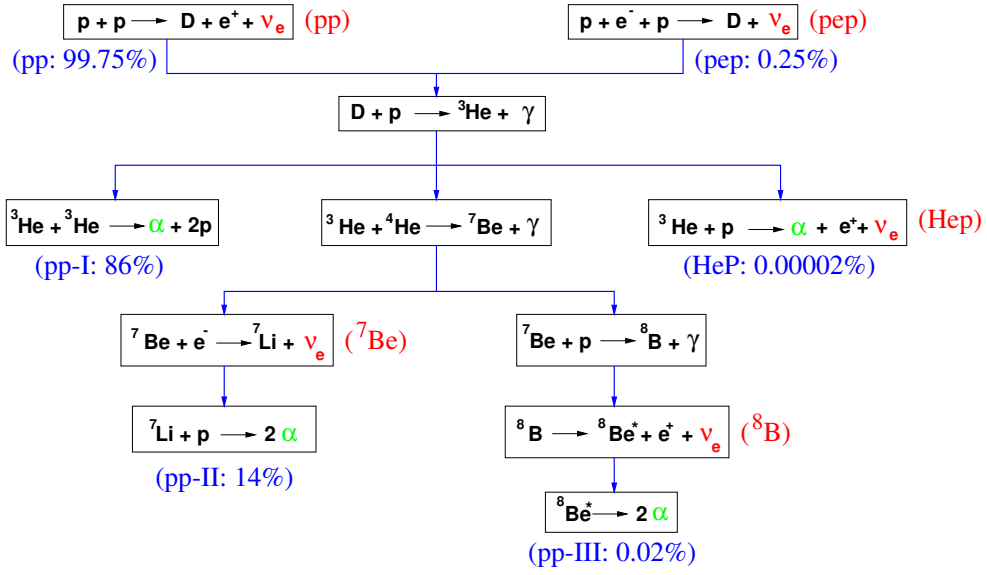


Figure 2.1: An schematic of the pp chain reactions in the sun. The neutrinos produced in this process are marked in red, and their relative contributions are given.

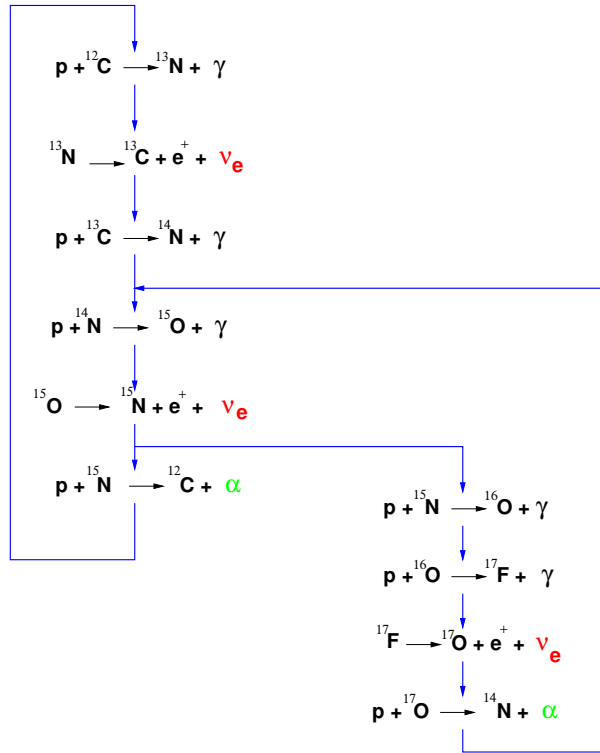


Figure 2.2: An schematic of the CNO chain reactions in the sun.

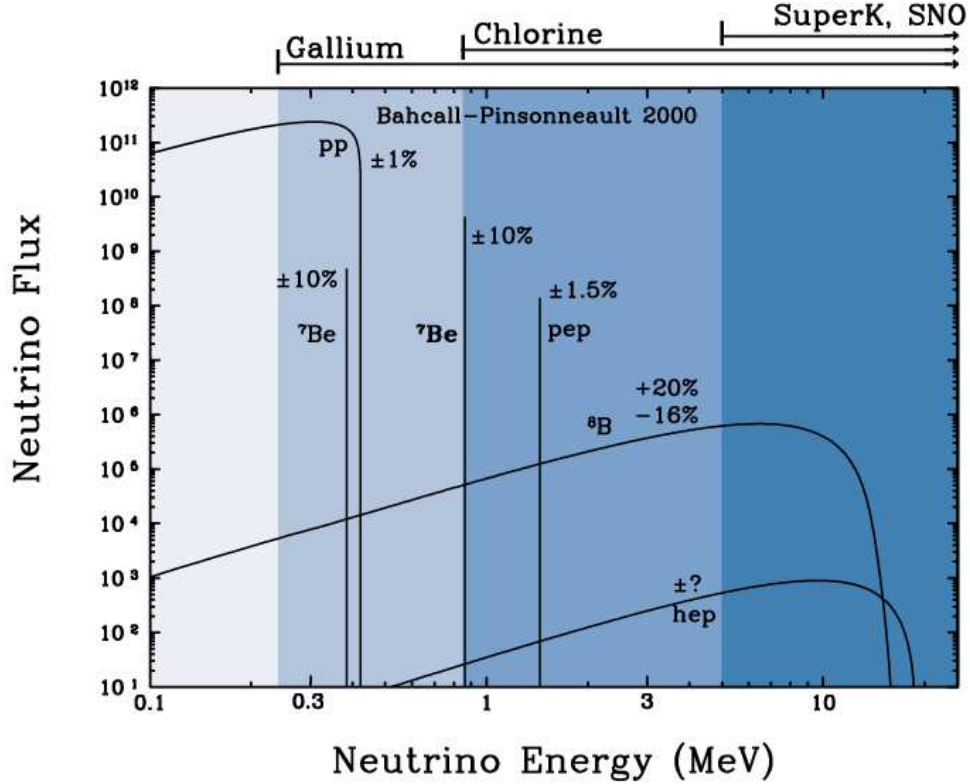


Figure 2.3: Energy spectra of the pp chain solar neutrinos. The colors indicate energy sensitivities of the various neutrino detection methods.

It must be noted that the sun produces only the electron neutrinos, ν_e , in each of the production channels.

Fig. 2.3 shows the neutrino energy spectra of the various pp chain production channels. The vast majority of the neutrinos produced in the sun are the pp neutrinos ($\sim 86\%$ [1]). However, due to their very low energies, only the current detectors with a gallium target can detect them (see Sec. 2.2). On the other hand, the ^8B neutrinos have a much lower flux, but span a much larger and higher energy range, and are readily detectable by all modern methods (gallium target, chlorine target, and water-Cherenkov method).

The fluxes of the neutrinos from all production channels, presented in Tab. 2.2, are calculated using the most recently determined value for the solar luminosity, $3.842 \times 10^{33} \text{ erg}^{-1}$ (which is 0.2% lower from the value used in the rest of the SSM,

$3.850 \times 10^{33} \text{ erg}^{-1}$) [4]. The fluxes at the earth are presented in $\text{cm}^{-2}\text{s}^{-1}$, and the rates for the chlorine and gallium (as well as lithium) detectors in *solar neutrino units* (SNU, number of interactions per second per 10^{36} target atoms). It is these BP2000 flux (and rate) predictions that are used as a standard in comparison with all current experimental measurements. The uncertainties in the fluxes are calculated by including the published errors in all experimental quantities and by taking into account the correlated influence of different input parameters.

Table 2.2: SSM neutrino flux predictions (BP2000) [4].

Source	Flux[$\text{cm}^{-2}\text{s}^{-1}$]	Cl[SNU]	Ga[SNU]	Li[SNU]
pp	$5.95 \times 10^{10}(1.0 \pm 0.01)$	0.0	69.7	0.0
pep	$1.40 \times 10^8(1.0 \pm 0.015)$	0.22	2.8	9.2
hep	9.3×10^3	0.04	0.1	0.1
^7Be	$4.77 \times 10^9(1.0 \pm 0.10)$	1.15	34.2	9.1
^8B	$5.05 \times 10^6(1.0_{-0.16}^{+0.20})$	5.76	12.1	19.7
^{13}N	$5.48 \times 10^8(1.0_{-0.17}^{+0.21})$	0.09	3.4	2.3
^{15}O	$4.80 \times 10^8(1.0_{-0.19}^{+0.25})$	0.33	5.5	11.8
^{17}F	$5.63 \times 10^6(1.0 \pm 0.25)$	0.0	0.1	0.1
Total	...	$7.6_{-1.1}^{+1.3}$	128_{-7}^{+9}	$52.3_{-6.0}^{+6.5}$

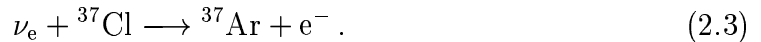
What makes the BP2000 SSM a successful model and the basis for all the experimental comparison in the solar neutrino field are its accomplishments in predicting quantities that have been independently experimentally confirmed. These various predictions were compared with experimental measurements from LOWL, BiSON, GOLF, GONG, and MDI [4]. The model's biggest success is, according to the authors, the excellent agreement between the calculated and the helio-seismologically measured sound speeds. The RMS fractional difference between the prediction and the measurement of the sound speeds is only $0.08 \sim 0.10\%$ for all solar radii.

2.2 History of the Solar Neutrino Deficit

Although the neutrino fluxes are well known from the SSM predictions, all solar neutrino experiments have detected a deficit in the flux. This so-called *solar neutrino problem* was first reported by the Homestake chlorine experiment in the late 1960's, and had remained unsolved for over 30 years.

2.2.1 Chlorine Experiment

The initial discovery of neutrinos from the sun was made in 1968 by Raymond Davis Jr., using an underground chlorine neutrino detector at the Homestake mine in South Dakota [6]. The detector, which has recently ceased operation, is located 2500 m below the surface and consists of 615 tons of tetrachloroethylene, C_2Cl_4 . The neutrino detection principle used in this experiment is the neutrino absorption on the chlorine:



An appearance of argon in the detector then signals a neutrino interaction. The energy threshold of this interaction is 0.814 MeV, making the chlorine detector sensitive to ${}^7\text{Be}$, pep, ${}^8\text{B}$, and hep neutrinos.

There is no directional information of the incoming neutrino in this method; only the total number of resulting argon atoms in the detector gives evidence of neutrino interactions. In the early days of solar neutrino research, Davis was able to extract the resulting argon atoms from the large chlorine target, and not only provide evidence of solar neutrinos, but also conclude that he was detecting too few of them ($\sim 1/3$) with respect to the prediction of the then-relevant SSM.

The ${}^{37}\text{Ar}$ atoms were extracted by bubbling He gas through the detector's tank. The ${}^{37}\text{Ar}$ is chemically isolated in a cryogenically cooled absorber and the number of atoms is counted by a proportional counter by observing Auger electrons as the ${}^{37}\text{Ar}$ decays. The extractions are only performed between data-taking runs, which

is every 1-3 months. About 1 ^{37}Ar is extracted from the detector per day. During each run, the extraction efficiency is checked by adding a small admixture of ^{38}Ar or ^{36}Ar carrier gas into the detector. The efficiency of this method was measured to be about 95%.

2.2.2 Kamiokande Experiment

For the next nearly 20 years, Homestake was the only solar neutrino detector, consistently reporting this flux deficit. It was not until 1987, when the upgraded Kamiokande II detector in Japan not only made an independent measurement of solar neutrinos but also reported a similar flux deficit [7]. Kamiokande used water Cherenkov techniques described in detail in Sec. 3.1 to detect electrons from the neutrino-electron elastic scattering interaction:

$$\nu + e^- \longrightarrow \nu + e^- . \quad (2.4)$$

Because of its relatively high energy threshold of 7.5 MeV, Kamiokande was only sensitive to ^8B neutrinos, as well as the much less abundant hep neutrinos (however, because of low statistic, only the ^8B neutrinos were considered in Kamiokande's analysis).

The detector was located ~ 1 km (2700 mwe) underground in the Kamioka mine, in Japan, and has since been dismantled. It was really a feasibility experiment [8] and a springboard for a much larger Super-Kamiokande detector. It was a cylindrical tank with 680 tons of ultra-pure water surrounded by 948 photo-multiplier tubes (PMTs). The PMTs detected Cherenkov light created by electron resulting from the elastic scattering of neutrinos. Because the direction of the reconstructed electron events is highly correlated with the direction of the parent neutrinos, solar neutrino events could be statistically separated by looking in the direction of the sun at the time of the event. After subtracting the background events and using a maximum likelihood

method to calculate the number of solar neutrino events, Kamiokande measured a flux deficit of $\sim 50\%$.

Besides independently confirming the solar neutrino deficit, Kamiokande was the first detector that could discern the direction of the incoming neutrino, and thus has shown that the detected neutrinos indeed come from the direction of the sun. Its other contribution to science was setting a stage for Super-Kamiokande and detecting neutrinos from SN1987A, the only supernova ever detected via neutrinos. Now, many of the parts from Kamiokande are used in Super-Kamiokande and KamLAND, including Kamiokande's rock cavity where KamLAND now stands.

2.2.3 Gallium Experiments

Two later, radiochemical experiments (similar to Homestake) SAGE in the Soviet Union [9] and Gallex/GNO in Italy [10], used a *gallium* target for detecting neutrinos via neutrino absorption on gallium:



SAGE (Soviet-American Gallium Experiment), which began operation in 1990, and is still running, is located deep underground (4700 mwe) at the Baksan Neutrino Observatory. It has a 50 ton liquid metal ${}^{71}\text{Ga}$ target in 7 reactors. The ${}^{71}\text{Ge}$ produced is separated from the ${}^{71}\text{Ga}$ by stirring vigorously with hydrogen peroxide and hydrochloric acid. The resulting GeCl_4 is extracted and converted to GeH_4 by sodium borohydride. The counting of the resulting Ge atoms is done by a proportional counter observing Auger electrons and x-rays emitted by the ${}^{71}\text{Ge}$ electron capture. The total efficiency in this method was measured to be $80 \sim 90\%$.

Gallex began operation in 1991 and was replaced in 1998 by its successor GNO (Gallium Neutrino Observatory), which is still in operation today. The so-called Gallex/GNO detector is located in the Gran Sasso Underground Laboratories, in

Italy. It consists of a 100 ton target in the form of $\text{GaCl}_3\text{-HCl}$ solution, containing 30.3 tons of gallium. Similarly to SAGE, the germanium resulting from the neutrino interaction is produced in the form of GeCl_4 , which is extracted by bubbling nitrogen through the solution, and converted to the counting gas, GeH_4 . The extraction and the subsequent counting is done at intervals of 4-6 weeks, and the extraction efficiency was measured to be $\sim 95\%$.

Both germanium detectors have the same unique advantage over other detection methods, which is the very low energy threshold of 0.233 MeV of the absorption reaction of neutrinos on gallium. Such a low threshold means that gallium detectors can detect neutrinos created in all of the different solar neutrino production channels (Sec. 2.1), and particularly the pp neutrinos, which make up 86% of the solar neutrinos, and whose flux is most reliably predicted. However, although the gallium detectors detect *all* of the solar neutrinos, they still report a neutrino flux deficit of $\sim 60\%$.

2.2.4 Neutrino Deficit

The status of the solar neutrino research in the 1990's was that five detectors and three independent neutrino detection methods consistently reported a solar neutrino flux that is significantly lower than the prediction of the well-tested and well-established BP2000. The independent measurements also involved different neutrino energy ranges, which made it clear that a modification outside of the SSM was inevitable if this solar neutrino problem was ever to be resolved.

Tab. 2.3 shows the SSM predictions and the experimental measurements of the neutrino rates for the different neutrino detectors prior to Super-Kamiokande (results from Gallex/GNO and SAGE are combined as a livetime weighted average into a single gallium rate). Across all detectors the neutrino deficit is obvious: the detectors detect only $< 60\%$ of the predicted neutrino rates, while the measured rates differ

by many standard deviations from the predictions.

Table 2.3: Measured solar neutrino deficit [4].

Experiment	BP2000	Measurement	Ratio
Chlorine	$7.6^{+1.3}_{-1.1}$	2.56 ± 0.23	0.34 ± 0.06
Gallium	128^{+9}_{-7}	74.7 ± 5.0	0.58 ± 0.07
Kamiokande	$5.05^{+1.01}_{-0.81}$	2.80 ± 0.39	0.55 ± 0.13

NOTE.—The units for the chlorine and gallium rates are SNU, while for the Kamiokande rate the units are $10^6 \text{ cm}^{-2}\text{s}^{-1}$. The asymmetric errors on the ratio are averaged.

A few modifications to the SSM were suggested in order to lower the expectation neutrino flux and thus resolve the problem, but all of them led to disagreements with the solar experiments. One of the prominent ideas in this direction was changing the input factor, S_{17} , of the ${}^7\text{Be} + \text{p} \longrightarrow {}^8\text{B} + \gamma$ interaction cross section. This factor is measured in the laboratory at much higher energies than are relevant for the sun, and are extrapolated down to MeV-range energies [11]. S_{17} is simultaneously the biggest source of the flux prediction uncertainty ($\sim 10\%$) for ${}^8\text{B}$ -neutrinos, and changing it would only decrease the expected ${}^8\text{B}$ flux.

Hata and Langacker [12] have compared flux predictions of several of these “non-standard” solar models with the experimental measurements of all the neutrino detectors, and have concluded that they could not reconcile fluxes of ${}^7\text{Be}$ - and ${}^8\text{B}$ -neutrinos, which should be related, since all of the ${}^8\text{B}$ in the sun is produced from ${}^7\text{Be}$. Because of these contradictions they have encountered, the solution to the solar neutrino problem needed to be sought after elsewhere.

In recent years, however, neutrino flavor oscillations have been proposed as a solution for the deficit. This solution was immediately attractive, because it left the SSM unmodified, and instead probed into physics beyond the standard model of particle physics. Prior to the mid 1990’s, the neutrino detectors have only detected

ν_e , which is the only neutrino flavor the sun produces, so if neutrinos oscillated into a different flavor on their way to the earth, the detectors would miss some of them, and naturally, report a flux deficit.

2.3 The Theory of Neutrino Oscillations

The discussion of the theory of neutrino oscillations was obtained from two of the leading theoretical neutrino experts, Mohapatra (*Massive Neutrinos in Physics and Astrophysics*) [1] and Bahcall (*Neutrino Astrophysics*) [2].

As stated earlier, neutrino oscillations are only possible if neutrinos have a finite mass. In such a case, the weak interaction neutrino eigenstates are in general a superposition of their mass eigenstates, since there is no fundamental reason why the particles observed via flavor interactions should correspond exactly to their physical states. This is called *neutrino mixing*. A neutrino of one flavor can, therefore, with time evolution, change into a *different* superposition of the mass eigenstates and become a neutrino of a different flavor. The discovery of neutrino oscillations is not only direct evidence for massive neutrinos, but moreover, it provides an indirect quantitative measurement of the mass.

In general, a flavor neutrino state ν_l (corresponding to a lepton l) is not a physical state, but rather a superposition of physical states (the energy eigenstates ν_α):

$$|\nu_l\rangle = \sum_{\alpha} U_{l\alpha} |\nu_{\alpha}\rangle, \quad (2.6)$$

where U is the mixing matrix dependent on a particular theoretical model. Schrödinger's theory suggests that the time evolution of such a state must have the following form:

$$|\nu_l(t)\rangle = \sum_{\alpha} e^{-iE_{\alpha}t} U_{l\alpha} |\nu_{\alpha}\rangle, \quad (2.7)$$

with E_{α} being the energy of the physical neutrino state ν_{α} . It is evident from this expression that one neutrino flavor state contains elements of another flavor state.

The amplitude of finding a neutrino $\nu_{l'}$ from a beam of propagating neutrinos ν_l is

$$\begin{aligned}
\langle \nu_{l'} | \nu_l(t) \rangle &= \sum_{\alpha, \beta} \langle \nu_\beta | U_{\beta l'}^\dagger e^{-iE_\alpha t} U_{l\alpha} | \nu_\alpha \rangle \\
&= \sum_{\alpha, \beta} e^{-iE_\alpha t} U_{l\alpha} U_{\beta l'}^* \langle \nu_\beta | \nu_\alpha \rangle \\
&= \sum_{\alpha} e^{-iE_\alpha t} U_{l\alpha} U_{l'\alpha}^*, \tag{2.8}
\end{aligned}$$

using the fact that the energy eigenstates are orthonormal. At time $t = 0$, the probability of finding a $\nu_{l'}$ is simply $\delta_{ll'}$, because of unitarity of the mixing matrix U . At time t , however, the probability becomes

$$P_{\nu_l \nu_{l'}}(t) = \sum_{\alpha, \beta} |U_{l\alpha} U_{l'\alpha}^* U_{l\beta}^* U_{l'\beta}| \cos[(E_\alpha - E_\beta)t - \varphi_{ll'\alpha\beta}] \tag{2.9}$$

where

$$\varphi_{ll'\alpha\beta} = \arg(U_{l\alpha} U_{l'\alpha}^* U_{l\beta}^* U_{l'\beta}). \tag{2.10}$$

Since in any physical situation neutrinos are highly relativistic, we can rewrite the energies as

$$E_\alpha = \sqrt{p^2 + m_\alpha^2} \quad \longrightarrow \quad E_\alpha \approx |\vec{p}| + \frac{m_\alpha^2}{2|\vec{p}|},$$

and replace the time t by the distance x traveled by the neutrino. Thus we obtain

$$P_{\nu_l \nu_{l'}}(t) = \sum_{\alpha, \beta} |U_{l\alpha} U_{l'\alpha}^* U_{l\beta}^* U_{l'\beta}| \cos\left(\frac{2\pi x}{L_{\alpha\beta}} - \varphi_{ll'\alpha\beta}\right), \tag{2.11}$$

where

$$L_{\alpha\beta} \equiv \frac{4\pi E}{\Delta_{\alpha\beta}}, \quad E \equiv |\vec{p}|, \tag{2.12}$$

and

$$\Delta_{\alpha\beta} \equiv (m_\alpha^2 - m_\beta^2). \tag{2.13}$$

The quantity $L_{\alpha\beta}$ is called the *oscillation length*, and it is the length scale over which the oscillation effects become significant. The quantity $\Delta_{\alpha\beta}$ is the *mass squared difference* between the ν_α and ν_β physical neutrinos, and it provides a quantitative way of experimentally determining the neutrino masses.

2.3.1 Two-Flavor Oscillations in Vacuum

It is most beneficial, both theoretically and experimentally, to consider two-flavor oscillations only. In this case, the mixing matrix U takes on the particularly simple form of a two dimensional rotation matrix:

$$U = \begin{pmatrix} \cos\theta & \sin\theta \\ -\sin\theta & \cos\theta \end{pmatrix}, \quad (2.14)$$

where θ is the *vacuum mixing angle*, generally taken to be $0 \leq \theta \leq \frac{\pi}{4}$. If $\theta = 0$, the neutrino is purely an energy eigenstate, and if $\theta = \frac{\pi}{4}$, the neutrino is an equal mixture of both energy eigenstates (full mixing).

In the case of $\nu_e \leftrightarrow \nu_\mu$ oscillations relevant in the solar neutrino sector, the time evolution of an electron neutrino is

$$|\nu_e(t)\rangle = \cos\theta e^{-iE_1 t} |\nu_1(t)\rangle + \sin\theta e^{-iE_2 t} |\nu_2(t)\rangle, \quad (2.15)$$

and the probability to find a ν_μ from the original ν_e (Eq. 2.11) becomes

$$P = |\langle \nu_\mu | \nu_e \rangle|^2 = \sin^2(2\theta) \sin^2\left(\frac{\Delta}{4E} x\right). \quad (2.16)$$

Indices 1 and 2 label the two energy eigenstates, Δ is the mass squared difference of the two masses, and E is the energy (momentum) of the neutrino. In an experimental analysis, one matches the theoretical oscillation probability (Eq. 2.16) to the observed data and obtains a best fit for two parameters, θ and Δ , thus indirectly measuring the amount of neutrino mixing and the neutrino mass.

In practice, there are two kinds of neutrino oscillation experiments: *appearance* and *disappearance* experiments. The discussion above was about an appearance experiment: measuring whether some of the original neutrinos oscillate into another flavor. An example is the $\nu_e \leftrightarrow \nu_\mu$ oscillations described by the probability, $P_{e \rightarrow \mu}$, in Eq. 2.16. While with an appearance experiment one can directly measure the properties of a specific neutrino oscillation channel, its disadvantage is the fact that

one has to know the oscillation channel a priori, and design the experiment for that particular channel. For the $\nu_e \leftrightarrow \nu_\mu$ oscillations, for example, it is extremely difficult to design a detector which will detect the resulting ν_μ at solar neutrino energies (~ 10 MeV). A muon-producing charged current interaction on a nucleus is impossible, because muon's rest mass is much higher (~ 100 MeV), and a simple scattering on muons is virtually impossible, because it is hard to imagine a muon target detector.

A disappearance experiment, on the other hand, simply measures how much of the original neutrino has not oscillated away into something else. An example of a disappearance experiment is $\nu_e \leftrightarrow \nu_e$ oscillations, i.e. measuring the survival probability of the electron neutrino. Super-Kamiokande can easily detect electrons resulting from $\nu_e + e^-$ interactions, and thus presents an example of a disappearance experiment in which the survival probability of ν_e is considered.

2.3.2 Oscillations in Matter: MSW Effect

The formalism presented above is valid for neutrinos propagating in vacuum. However, the oscillation effect may be significantly enhanced if neutrinos are propagating through matter. The reason for the difference is the fact that matter is mostly comprised of electrons and nucleons, but not of muons and taus. Therefore, the electron neutrinos can interact with the electrons in matter via both the neutral and the charged current, while the muon and tau neutrinos can only undergo the neutral current interactions with electrons. Due to the interactions in the medium, a particle propagating in matter develops an “effective mass”. Because the electron neutrinos interact through an extra channel, their effective mass will be modified differently relative to the muon and tau neutrinos. If we assume that the physical neutrino state is a mixture of ν_e , ν_μ , and ν_τ , then the oscillation probabilities will change with respect to those in vacuum.

In order to explore quantitatively the changes in the oscillation probabilities that matter effects bring about, we need to express the time evolution of a neutrino beam in vacuum in a slightly different form. First, we will again only consider the simple two-flavor oscillation case ($\nu_e \leftrightarrow \nu_\mu$) in vacuum. The time evolution of two energy eigenstates can be written as

$$i \frac{d}{dt} \begin{pmatrix} \nu_1(t) \\ \nu_2(t) \end{pmatrix} = H \begin{pmatrix} \nu_1(t) \\ \nu_2(t) \end{pmatrix}, \quad \text{where } H = \begin{pmatrix} E_1 & 0 \\ 0 & E_2 \end{pmatrix}, \quad (2.17)$$

and we can use the mixing matrix U , which connects the energy eigenstates to the flavor eigenstates, to write the time evolution in the flavor basis:

$$i \frac{d}{dt} \begin{pmatrix} \nu_e(t) \\ \nu_\mu(t) \end{pmatrix} = H' \begin{pmatrix} \nu_e(t) \\ \nu_\mu(t) \end{pmatrix}, \quad (2.18)$$

where (after a little algebra):

$$H' = U H U^\dagger = E + \frac{m_1^2 + m_2^2}{4E} + \frac{\Delta}{4E} \begin{pmatrix} -\cos 2\theta & \sin 2\theta \\ \sin 2\theta & \cos 2\theta \end{pmatrix}. \quad (2.19)$$

The mixing angle θ that diagonalizes this matrix is given by

$$\tan 2\theta = \frac{2H'_{12}}{H'_{22} - H'_{11}}. \quad (2.20)$$

Now let us turn our attention to neutrinos propagating through matter. Due to the contributions from the charged and neutral current interactions of the neutrinos with electrons and nucleons, the time evolution of a neutrino beam will be Eq. 2.18 where the matrix H' is replaced by

$$\tilde{H} = E + \frac{m_1^2 + m_2^2}{4E} - \frac{1}{\sqrt{2}} G_F n_n + \frac{\Delta}{4E} \begin{pmatrix} -\cos 2\theta + \frac{4E}{\Delta} \sqrt{2} G_F n_e & \sin 2\theta \\ \sin 2\theta & \cos 2\theta \end{pmatrix}, \quad (2.21)$$

where G_F is the Fermi coupling constant, and n_n and n_e are the neutron and the electron densities, respectively. In this illustration, we are constraining our analysis to the constant density case only. The extra density terms in the expression above

come from the charged and neutral current interaction Lagrangian contributions, the detailed derivation of which can be found in [1] (pp. 189-191). The effective mixing angle in matter, $\tilde{\theta}$, that diagonalizes this new matrix is then

$$\tan 2\tilde{\theta} = \frac{2\tilde{H}_{12}}{\tilde{H}_{22} - \tilde{H}_{11}} = \frac{\Delta \sin 2\theta}{\Delta \cos 2\theta - 2\sqrt{2}G_F n_e E}. \quad (2.22)$$

As can be seen, the mixing angle is altered in matter. In the special case when the electron number density of the medium is the resonance density,

$$\hat{n}_e = \frac{\Delta \cos 2\theta}{2\sqrt{2}G_F E}, \quad (2.23)$$

the change in the mixing angle is maximal. In this case, even if the vacuum mixing angle θ is small, the effective mixing in matter is maximal ($\tilde{\theta} = \frac{\pi}{4}$). This effect is called the *MSW effect*.

The result of the MSW effect is that even if the neutrinos would not oscillate considerably in vacuum, the oscillations can be very appreciable in a medium with electron density close to the resonance density \hat{n}_e . This result is important for the solar neutrinos, which propagate through the sun's interior on the way out of the sun's core. If the electron density of the sun's plasma is close to \hat{n}_e , we should detect effects of matter oscillations of neutrinos from the sun.

In the actual calculation of the ν_e survival probability used in this work, a more realistic, variable electron density profile of the sun was considered. The probability was calculated numerically and integrated throughout the sun's interior, stepping in the radial direction considering different angles with respect to the direction to the earth. The electron density as a function of the solar radius was obtained from the SSM [4].

2.3.3 Regeneration in the Earth (MSW)

A similar MSW effect appears when the solar neutrinos propagate through the core of the earth before they interact in the detector (i.e. at night). The effect is similar

to the one in the core of the sun: the plasma in the earth's core can enhance the oscillation from ν_μ back into ν_e , thus making it seem like fewer solar neutrinos, originally ν_e , have oscillated away. This is the basis for the so-called day/night effect, where we expect the neutrino night flux (when the sun is on the other side of the earth) to be higher than the day flux (when the sun is on the same side of the earth as the detector). The effect is usually presented as the day/night flux asymmetry, $2(N-D)/(N+D)$. The largest day/night effect is present in MSW oscillation models with large neutrino mixing angles ($\sin^2 2\theta \sim 1$).

2.4 Solution of the Solar Neutrino Deficit

So naturally, the question arises: does the theory of neutrino flavor oscillations solve the long-standing solar neutrino problem? Combining the neutrino fluxes obtained from all the radiochemical (chlorine+gallium) data and comparing them to the BP2000 SSM predictions in which oscillations were considered, yields four general oscillation parameter ($\Delta m^2, \tan^2\theta$) regions as possible solutions to the solar neutrino deficit. This was accomplished by performing a fit to the simple χ^2 function:

$$\chi_{\text{Cl+Ga}}^2 = \frac{(d_{\text{Cl}} - p_{\text{Cl}})^2}{\sigma_{\text{Cl}}^2} + \frac{(d_{\text{Ga}} - p_{\text{Ga}})^2}{\sigma_{\text{Ga}}^2}, \quad (2.24)$$

where the two gallium rates were combined into a single flux number, and the uncertainty (σ) involves uncertainties of all of the relevant solar neutrino types and their correlations; d is the measured flux normalized to the BP2000 SSM no-oscillation prediction, and p is the oscillation prediction of the total neutrino rate.

Fig. 2.4 shows the χ^2 map for this fit and the four general solution regions: LMA - large mixing angle solution with $\Delta m^2 \approx 10^{\{-4,-5\}}$ and $\tan^2\theta \approx 1$; SMA - small mixing angle solution with $\Delta m^2 \approx 10^{-5.5}$ and $\tan^2\theta \approx 10^{-3}$; LOW - large mixing, low mass squared difference solution with $\Delta m^2 \approx 10^{\{-7,-8\}}$ and $\tan^2\theta \approx 1$; VAC - vacuum oscillations solution with $\Delta m^2 \approx 10^{\{-9,-11\}}$ and $\tan^2\theta \approx 1$. The figure

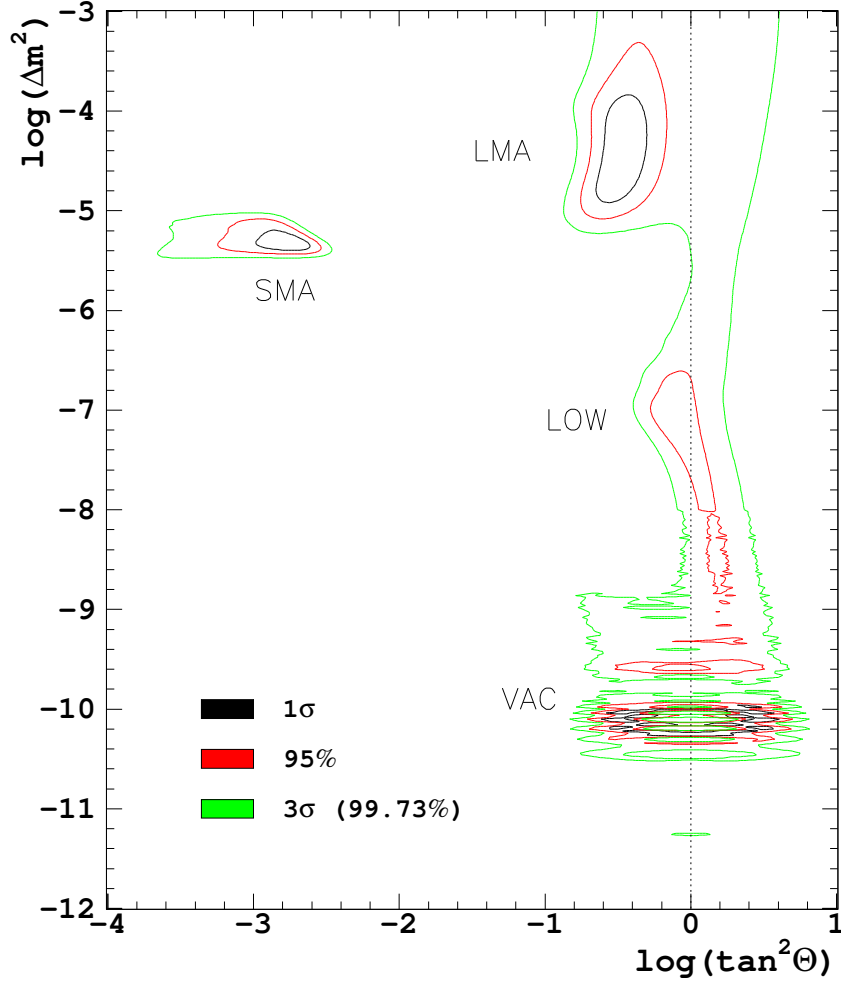


Figure 2.4: The χ^2 fit map of neutrino oscillation parameters using the chlorine and gallium total rates. The four possible solution regions are: LMA, SMA, LOW, and VAC.

shows the 1σ , 95%, and 3σ c.l. contours ($\Delta\chi^2 = 2.28, 5.99$, and 11.83 , respectively) although the standard, agreed-upon c.l. for these kinds of presentations is the 95% (red).

The neutrino oscillation models with oscillation parameters belonging to any of these four solution regions would completely solve the solar neutrino puzzle and explain the measured flux deficit. All of the subsequent effort in the solar neutrino community has been concentrated on: 1) confirming that oscillation hypothesis is the only scenario that truly explains the deficit, 2) discerning which of the four possible solution regions is the correct one, and 3) narrowing the allowed region for the best

model.

With this in mind, we now turn to the description of the Super-Kamiokande neutrino detector, designed to further explore the scenario of neutrino flavor oscillations and these four solution regions.

Chapter 3

Super-Kamiokande Detector

In order to test the hypothesis of solar neutrino flavor oscillations, and confirm that the deficit is really a result of the neutrino oscillation phenomenon and not a deficiency in the detection method the SSM, a much larger detector had to be built. The radiochemical experiments are large and have had a long data collection time, but are only sensitive to ν_e and cannot measure the direction or the energy of the neutrino, and thus, cannot distinguish between a possible deficiency in the detection method and a solution which proclaims neutrino oscillations as the reason for the flux deficit. Kamiokande was sensitive to all neutrino flavors and it could measure both the energy and the direction of the neutrino, but it was too small and it would require a very long data collection time to gain enough data to be able to make such a distinction. However, from the experiences gained in Kamiokande, was born the idea for the next generation neutrino detectors, such as Super-Kamiokande.

As stated in the previous chapter, the combined oscillation result of the radiochemical experiments yielded four distinct oscillation solution regions. These experiments measured only the total neutrino flux, which could not be used to distinguish between the four solutions or require modifications to the SSM. However, each of the four solutions predicts a different distortion in the neutrino energy spectrum (due to energy dependence of the oscillation probability, Eq. 2.16) or a different asymmetry

Table 3.1: SK predictions of the day and night fluxes for the four oscillation solutions.

Solution	Day flux (\times SSM)	Night flux (\times SSM)
LMA (-4.5, -0.5)	0.367	0.388
SMA (-5.3, -2.8)	0.499	0.503
LOW (-7.0, -0.1)	0.531	0.547
VAC (-10.0, -0.0)	0.444	0.444
D/N (-5.5, -1.3) ^a	0.197	0.558

^aNOTE.—The “D/N” solution ($\Delta m^2 = 10^{-5.5}$, $\tan^2\theta = 10^{-1.3}$) is shown as an example of a region with a high day/night flux asymmetry.

between the day and night neutrino fluxes (due to matter effects on oscillations in the earth, Sec. 2.3.3). The experience from the Kamiokande experiment hinted at the fact that a possible detection or a lack of detection of a spectral distortion or a day/night effect can conclusively point to just one of the solution and rule out the others.

Fig. 3.1 shows the predictions of the distortions in the event energy spectrum for the four oscillation solutions: LMA ($\Delta m^2 = 10^{-4.5}$, $\tan^2\theta = 10^{-0.5}$), SMA ($\Delta m^2 = 10^{-5.3}$, $\tan^2\theta = 10^{-2.8}$), LOW ($\Delta m^2 = 10^{-7.0}$, $\tan^2\theta = 10^{-0.1}$), and VAC ($\Delta m^2 = 10^{-10.0}$, $\tan^2\theta = 10^{-0.0}$). The values of the oscillation parameters were arbitrarily chosen from the center of the corresponding solution region. The spectrum of ${}^8\text{B}$ neutrinos was used as an input to the plots, and the resulting event spectrum was normalized by its SSM prediction (with no oscillations). Tab. 3.1 shows similar predictions for the day and night neutrino fluxes. An additional solution, D/N ($\Delta m^2 = 10^{-5.5}$, $\tan^2\theta = 10^{-1.3}$), is also shown for comparison, because it features a much larger day/night flux asymmetry than any of the other four solutions.

A detection of either a spectral distortion (shown in Fig. 3.1) or a day/night effect (shown in Tab. 3.1) would provide conclusive evidence for solar neutrino oscillations.

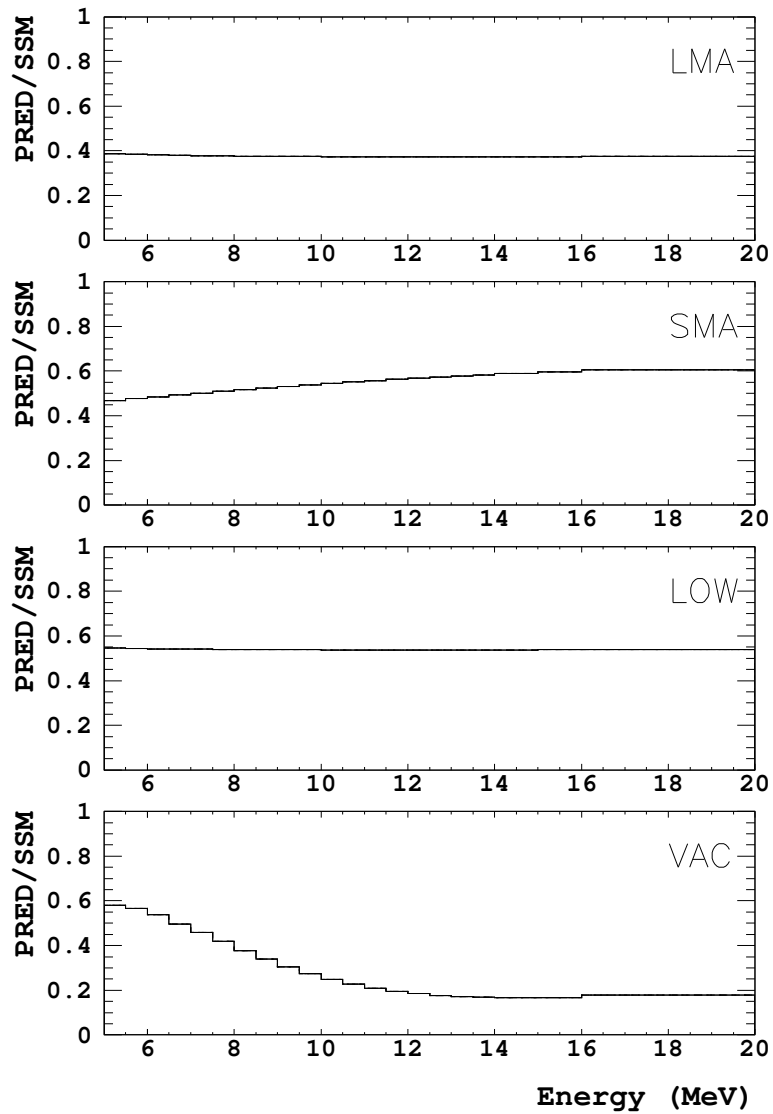


Figure 3.1: SK predictions of the energy spectrum distortions of the four oscillation solutions: LMA, SMA, LOW, VAC. Note that the last energy bin is from 16 – 20 MeV.

A non-detection of either could, on the other hand, rule out some of the solutions.

This was precisely the motivation for building the large Super-Kamiokande detector, which has a fiducial volume almost two orders of magnitude larger than Kamiokande, and thus, can gain very high statistics needed for the discerning of spectral distortions and a day/night effect with a $3 \sim 4\%$ uncertainty. Along with Super-Kamiokande, the other two modern-day neutrino detectors, SNO and KamLAND, were also designed for a similar purpose.

3.1 Neutrino Detection Method

Super-Kamiokande is a water Cherenkov neutrino detector, which means it detects neutrinos through the production of Cherenkov light in water. A neutrino traveling through the detector interacts in water via one of the interactions which are possible in the particular detector medium and produces a lepton (an electron). The neutrino interaction in the Super-Kamiokande detector is elastic scattering on electrons (ES):

$$\nu_{e,\mu,\tau} + e^- \longrightarrow \nu_{e,\mu,\tau} + e^- \quad (3.1)$$

Because the energy ranges relevant for solar neutrinos are generally higher than the electron's rest mass (0.511 MeV), the relativistic electrons thus produced travel at a speed, v , which is faster than the speed of light in water, c/n , where c is the speed of light in vacuum and n is the index of refraction of water. The index of refraction of SK's ultra-pure water is 1.33. Just as a sound shock wave is produced when an airplane travels faster than the speed of sound in the air, a similar *light* shock wave is produced in this case. This shock wave is called Cherenkov light, named after its discoverer, and is a bluish light of the wavelength of $300 \sim 700$ nm. It propagates as a cone around the propagation direction of the electron, with an opening angle (θ_c) of:

$$\cos\theta_c = \frac{1}{nv/c}. \quad (3.2)$$

For a relativistic electron ($v \approx c$), this opening angle is around 42° . The energy threshold for electrons producing Cherenkov light in water is 0.768 MeV , which is low enough for almost all solar neutrino types (see Ch. 2).

The number of Cherenkov photons produced in this process per unit length per unit energy (frequency) is a constant:

$$\frac{d^2 N_{\text{photon}}}{dL d\nu} = \frac{2\pi\alpha}{c} \sin^2 \theta_c, \quad (3.3)$$

and can be used to infer the electron's energy, if the total number of detected photons and the distance traveled by these photons is known. For highly relativistic electrons in SK, about 390 photons are expected per cm traveled.

The Cherenkov photons traveling through the water are detected with an array of photomultiplier tubes (PMTs), which surround the water in all directions. Because of the conical nature of the Cherenkov light, a ring pattern of photons is detected by the PMTs on the wall. An example of one such ring pattern from the real SK data is shown in Fig. 3.2. Electrons penetrating through water undergo multiple Coulomb scatterings, which will alter slightly the direction of the electron and in effect blur the generally “clean” edges of the ring pattern. From the pattern and the arrival time of the photons in an actual ring, it is possible to reconstruct the direction of the electron and the distance to its origin, i.e. the place of the original neutrino interaction. Using Eq. 3.3 to calculate the electron's energy, and knowing the nature of the relevant neutrino interaction that produced the electron, one can indirectly extract all information about the solar neutrino. This reconstruction process is described in more detail in Ch. 4.

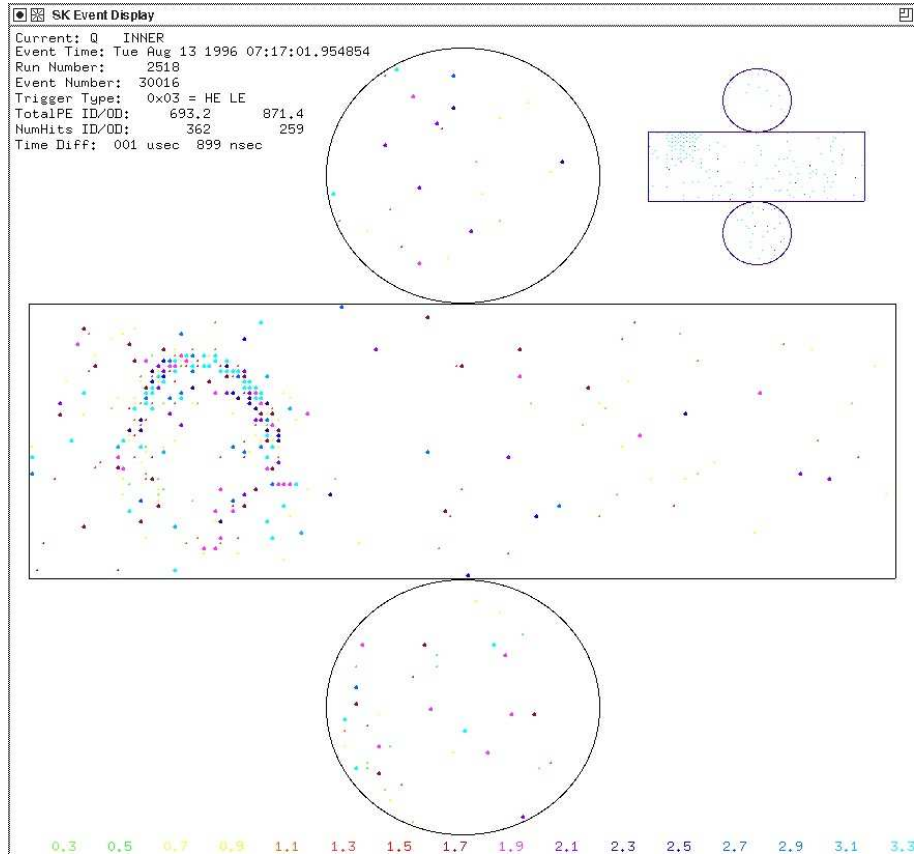


Figure 3.2: An example of a ring pattern on the PMTs generated by an electron traveling through Super-Kamiokande. Each dot in the display is a single PMT.

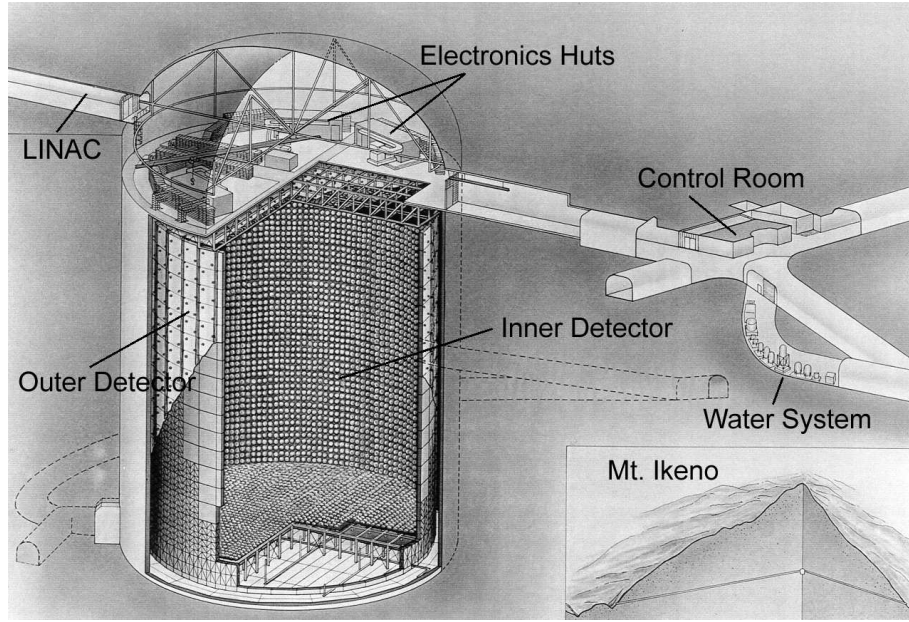


Figure 3.3: An illustration of Super-Kamiokande detector.

3.2 Description of the SK detector

3.2.1 Detector Overview

Super-Kamiokande (SK) is an underground ring-imaging water Cherenkov neutrino detector located in the Kamioka mine in Kamioka, Japan (137.32° E longitude, 36.43° N latitude). SK is a cylindrical tank (41.4 m in height, 39.3 m in diameter) filled with 50 kton of ultra-pure water, and situated under about 1 km of rock (2700 mwe). The rock provides a great shield against the cosmic ray muons: the muon rate in the detector is reduced to 2.2 Hz. An illustration of the SK detector is shown in Fig. 3.3.

The outer walls of the tank are constructed from 5 cm thick stainless steel sheets, which are attached to the rock cavity and backed by concrete. About 2 m in from the wall is a 1 m wide structure of stainless steel beams that provide the backbone for the mounting of the PMTs. The structure divides the whole detector tank into an inner detector (ID) and an outer detector (OD). The 11,146 inward-facing ID PMTs that

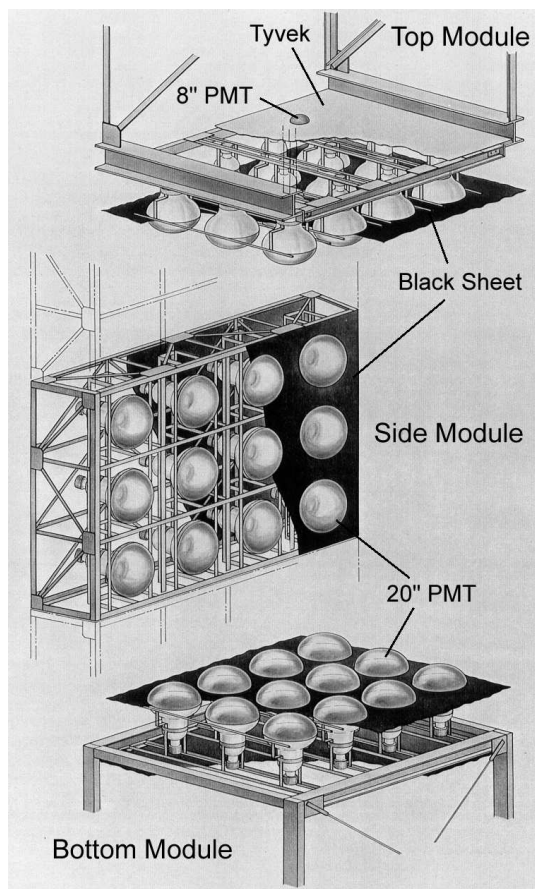


Figure 3.4: A view of the ID and OD PMT mounting at Super-Kamiokande.

are used in event detection are mounted on the inside of the steel beam structure and are surrounded with black polyethylene sheets to minimize light reflection within the ID region. They provide a photo-coverage of 40%. The mounting of the PMTs of both the ID and the OD is shown in Fig. 3.4. The region of the ID that is actually used in the analysis is 2 m inside the PMT structure and represents a fiducial volume of 22.5 kton. The entire ID region is a volume of 32.5 kton. One major reason for excluding the 2 m of volume adjacent to the steel structure is to reduce the background from radioactive decays of radon which is particularly prominent near the PMTs and the steel beams. The radon is still the main source of background in the fiducial volume, but the 2 m reduction of the volume brings these background levels to a manageable level. The other major reason for excluding the 2 m of space is

a need for multiple PMT hits: if an event happens very near a PMT, all of the light will be collected by that same PMT, and there will not be sufficient information for reconstructing that event. The PMTs used in SK's ID are 50 cm in diameter, and they are the largest PMTs in the world, designed and constructed especially for the SK experiment.

The OD, which surrounds the steel structure, has 1885 outward facing 20 cm PMTs, and the whole interior of the OD (with the exception of the PMT surfaces) is lined with white Tyvek sheets. The white Tyvek was put in place to maximize the reflection of the light in the OD, and in turn, enhance the light collection power of the PMTs, since the OD is mostly used as a veto trigger for tracking incoming muons. In addition, each of the OD PMTs has a wave shifter plate attached to it, which increases the light collection of the PMT even further. The "thickness" of the OD is 2.05 m on the top and the bottom, and 2.2 m in the mantle region. The OD also serves as a passive water shield for gamma activity in the surrounding rock.

The top of the tank is a flat steel sheet that covers the entire area of the detector. It is under a dome, which is lined with a polyurethane material, called Mineguard, to reduce the radon emanation and erosion from the rock walls. All the electronics huts, containing the data acquisition systems and all the calibration equipment are located inside the dome. The detector is also surrounded by 26 Helmholtz coils in order to reduce the magnetic field in the detector. An external magnetic field can affect the 50 cm PMTs as well as the trajectories of the charged electrons in the water. The coils reduce the field to 50 mG, which is low enough for proper operation of the detector.

The construction of SK was begun in 1991, with the excavation of the cavity, and was completed in December, 1995. The data taking for the so-called SK-I phase of the experiment was from April, 1996 until July 2001, when the detector was turned off for repair and upgrade. The official SK-I phase for the solar neutrino analysis is

May 31, 1996 - July 15, 2001.

3.2.2 Water and air purification systems

The ultra-clean water, which is essential for the proper transmission of the Cherenkov light, is supplied from the natural underground mine water and filtered through the water purification system in several stages. A schematic view of the water purification system is shown in Fig. 3.5. The output of this system is the purest water on earth. Its average resistivity is 18.20 M Ω cm, which is very close to the chemical limit of 18.24 M Ω cm. This extremely low level of impurities in the SK water is important in minimizing the background from radioactivity and scattering or absorption of the Cherenkov light. During normal operation, the average water transparency of the water has been 75 ~ 95 m.

The air in the detector, above the ultra-pure water, is supplied from the outside of the mine, and is purified through the radon-free air system illustrated in Fig. 3.6. The reason for the purification of the air is again minimizing the background from radioactivity, mainly due to the radon naturally occurring in the mine air. The purified injected air has a radon concentration of roughly 10 mBq/m³.

The water and air purification systems are described in detail in Ref. [13] and [14].

3.2.3 Photomultiplier Tubes

PMTs are the basic photosensitive devices that are at the core of the operation of any water Cherenkov detector. The tubes detect Cherenkov light and convert it into electrical signals, which are measured by the data acquisition system (DAQ) of the detector. If enough PMTs receive a “hit” (i.e. detect Cherenkov light), the detector’s trigger activates and the DAQ registers an “event”. The PMT signals are then collected and processed by the DAQ system, which converts the PMT signals

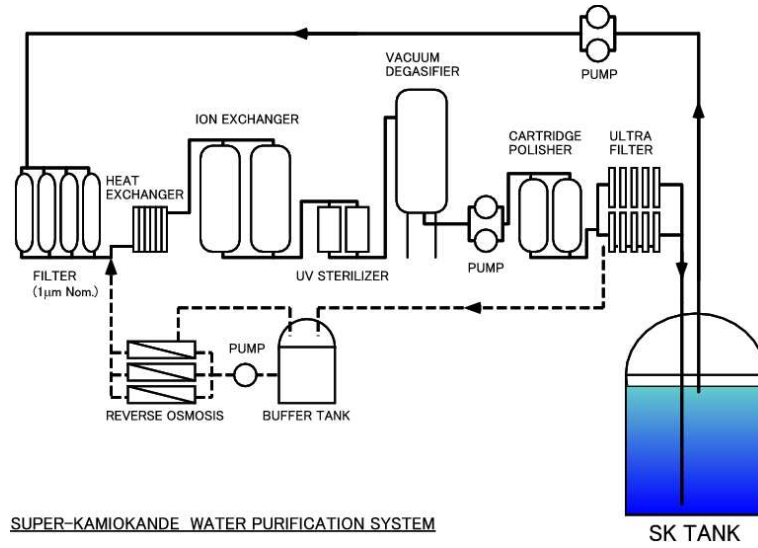


Figure 3.5: A schematic view of SK's water purification system.

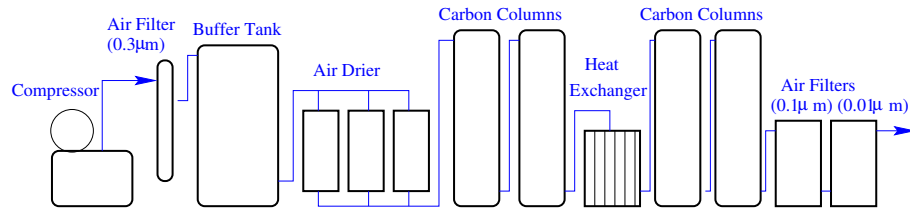


Figure 3.6: A schematic view of SK's radon-free air purification system.

into the timing and charge information of the PMT. In the final stage, computer programs then convert the timing and charge information of each hit PMT for a single event into physical variables, which can be used in a physics analysis.

The PMTs are made from thin borosilicate glass, and the light-sensitive surface is lined with a thin bialkali (Sb-K-Cs) photocathode, which matches the wavelength of Cherenkov light (300~700 nm). The photocathode absorbs a Cherenkov photon and generates a single electron called photo-electron. The photo-electrons are accelerated toward a series of dynodes by an electric field produced by a ~ 2 kV potential between the photocathode and the dynodes. The electron arriving at the dynodes triggers an emission of 3-5 more electrons, which travel to the next dynode. This creates a cascade of more and more electrons being created and accelerated. The process is repeated until a single photo-electron is multiplied into $\sim 10^7$ electrons. This multiplication factor is called the gain of the PMT. The resulting electrons are collected at the anode and are sent to the DAQ system as a macroscopic electric signal.

Inner Detector 50 cm PMTs

The PMTs used in the ID of Super-Kamiokande are Hamamatsu model R1449 50.8 cm (20 inch) PMTs, shown in Fig. 3.7. They have been specially designed and hand-made for this purpose, and represent an improvement from the 50 cm tubes used in Kamiokande. Since most of the solar neutrino events produce only a single electron in a single PMT (because of the relatively low energy of these neutrinos), the PMTs are designed to be able to clearly separate the dark noise from the peak of the 1 p.e. events. This separation is shown in Fig. 3.8.

The quantum efficiency, which is the probability that a photon hitting the photocathode will produce a photo-electron, of SK's PMTs is shown in Fig. 3.9. It is clear from the figure that the tubes are most sensitive to wavelengths of ~ 400 nm, which is in the range of Cherenkov light. The quantum efficiency for wavelengths

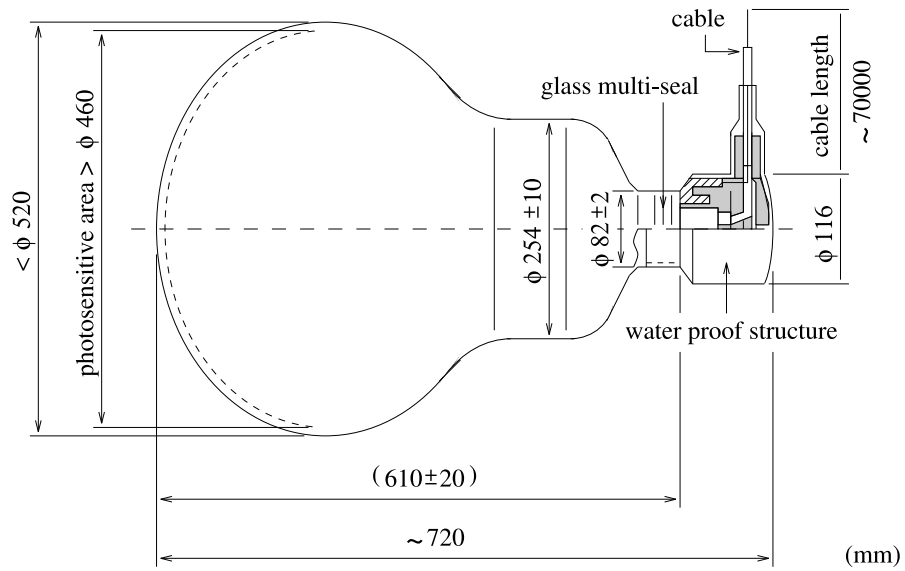


Figure 3.7: A schematic view of SK's inner detector 50 cm PMT.

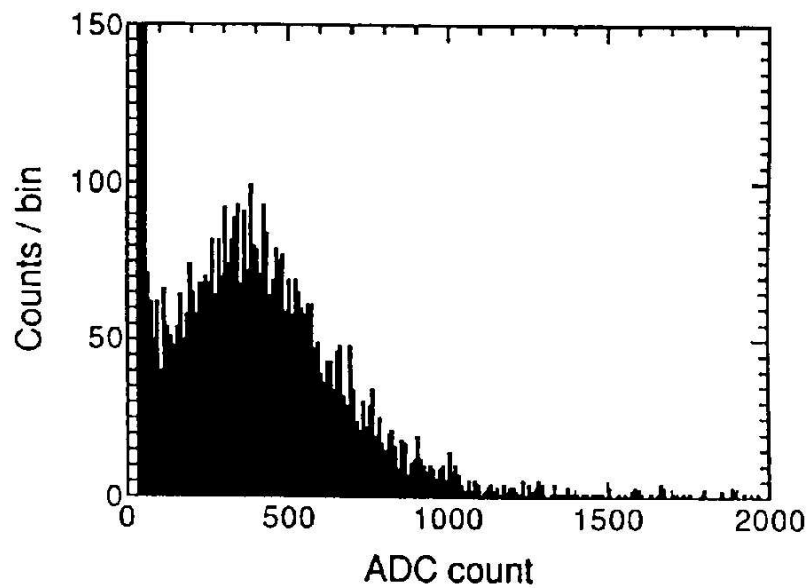


Figure 3.8: An ADC histogram demonstrating the separation of the dark noise from the 1 p.e. peak in SK's 50 cm ID PMT.

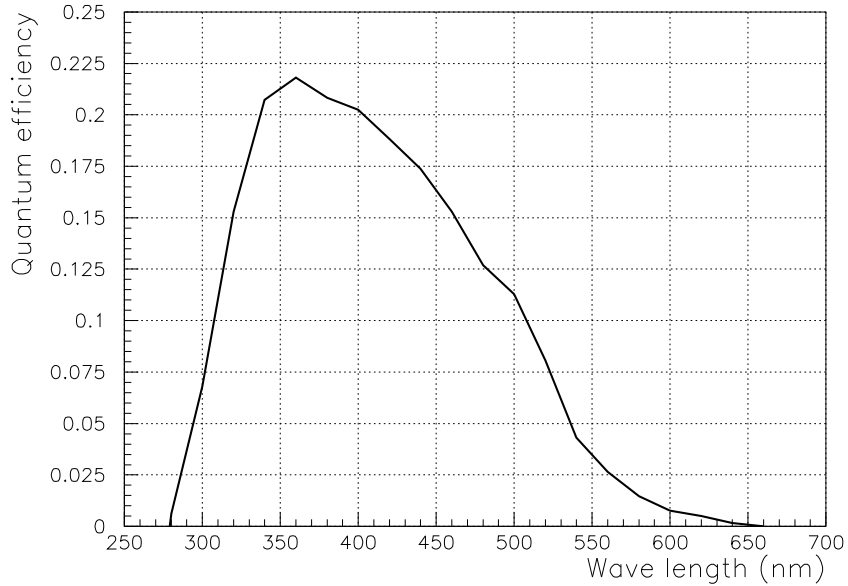


Figure 3.9: The quantum efficiency of the 50 cm PMTs in the wavelength range of the Cherenkov light.

of 360-400 nm is 21%, and the collection efficiency for photo-electrons at the first dynode is over 70%.

Outer Detector 20 cm PMTs

The PMTs used in the OD are 20 cm (8 inch) Hamamatsu model R1408 PMTs. These PMTs were originally used in the IMB detector [15], and have been adopted for use in SK. Each has a wavelength shifting acrylic plate ($\sim 60 \text{ cm} \times 60 \text{ cm}$) attached to it, for increased light collection power. These plates are attached directly to the face of the PMT. They absorb ultraviolet light and shift its frequency re-emitting photons in the blue wavelength range with an efficiency of 55%.

3.2.4 DAQ electronics

The role of the DAQ (data acquisition system) is to collect the electrical signals from all the PMTs that registered a photon, convert them into a time and charge deposited for each PMT, and combine this information into an event. The DAQ also

discriminates between a real physical event and a result of dark noise hits.

Inner Detector DAQ

The primary focus of the ID DAQ is to provide continuous data collection for the detector. A schematic view of the ID DAQ is shown in Fig. 3.10. The signal cable from each of the 11,146 ID PMTs is connected to a single channel of an analog timing module (ATM). The ATM has a functionality of a combined ADC (charge-to-digital converter) and TDC (time-to-digital converter), and each ATM channel has two self-enabling sub channels with a threshold of $1/4$ p.e. When a PMT receives a photon hit which is above the threshold, one of the ATM channels is activated, the PMT signal is recorded, and a digital “HITSUM” pulse (15 mV, 200 ns) is generated. The HITSUM pulses of all active channels are added together and if the summed pulse exceeds some preset threshold, a global trigger is issued. After a global trigger, all the activated ATM subchannels save and digitize the PMT charge and time signals, while the other subchannel takes over the data acquisition, thus eliminating “dead time”. If no global trigger is issued in $1.1 \mu\text{s}$, the information in the active subchannel is lost, and the subchannel is reset. The saved digitized ATM signals are sent to a super memory partner (SMP) module for transfer to the online computer system. The ATM channels have a 450 pC dynamic range for charge, with a resolution of 0.2 pC, and a 1300 ns dynamic range for time, with a resolution of 0.4 ns. To maintain accuracy of the timing and charge information, conversion tables are used to convert ADC and TDC counts into pC and ns, respectively. These tables are generated using pedestal data, which are taken every 30 min.

The ATM channels are connected in the custom built TKO (TRISTAN KEK Online) ATM cards in groups of 12 (12 PMTs are connected to a single TKO ATM card), and 20 ATM cards are placed into a single TKO crate. Each TKO crate contains a GONG (go/no-go) module, which distributes global trigger information into

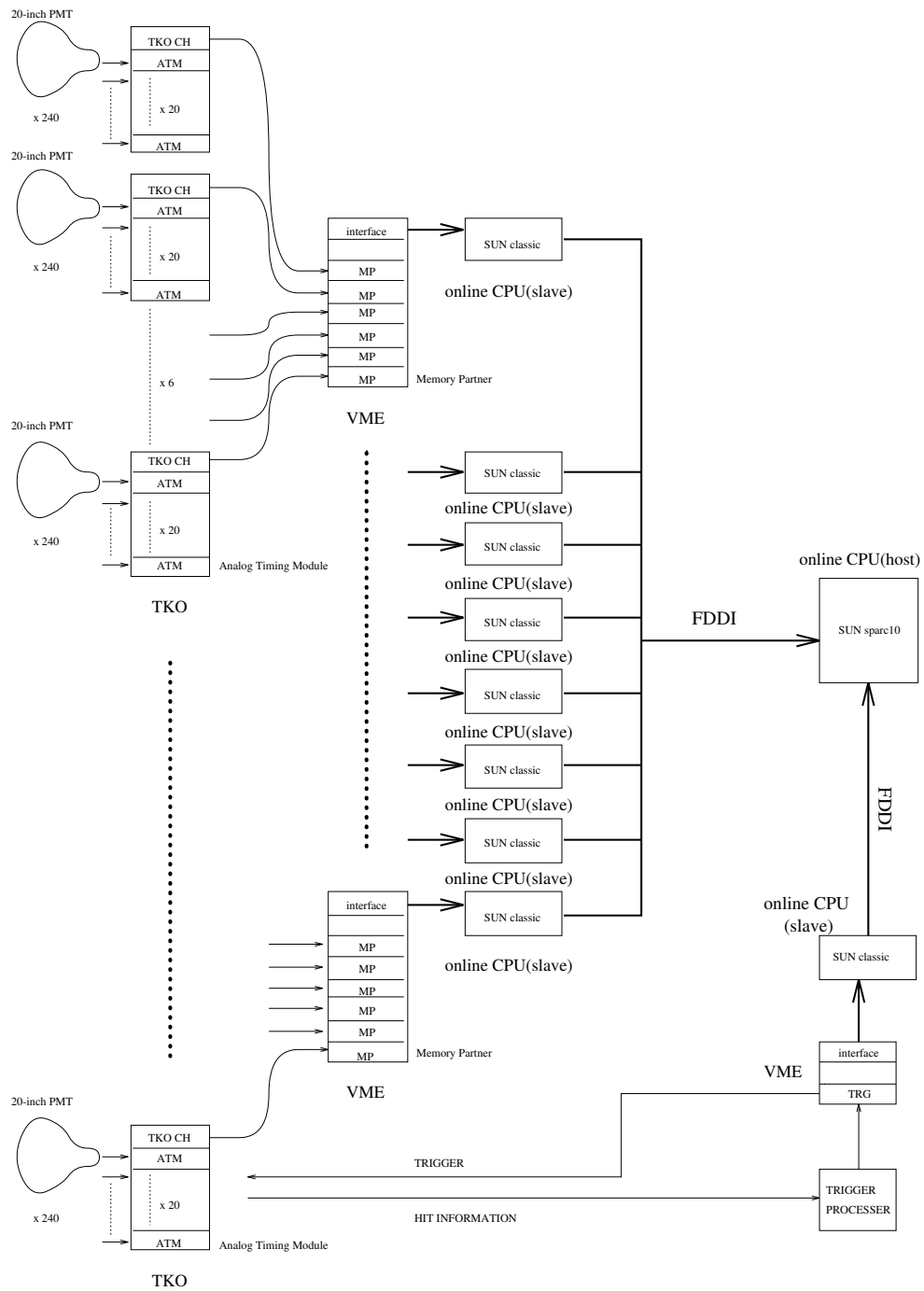


Figure 3.10: A schematic view of SK's ID DAQ system.

all ATMs, and a SCH (super control header) module, which transfers the digitized ADC/TDC data from the ATM, read by the SDS (sparse data scan) method, to a single SMP in the VME crate. There are 12 TKO crates in each of the 4 main electronics huts. Each hut has two VME crates with 6 SMP modules (1 SMP module for each TKO crate), and a Bit-3 Sbus-VMEbus interface card used to transfer the SMP data to the memory of an online Sun workstation. The data from the 8 Sun workstations are transferred via an FDDI optical network to the online host computer, which assembles the digitized data from all the hit PMTs into an event. Environment data, event time, trigger, and OD PMT information are added from the appropriate electronic system located in the central (5th) electronics hut.

Each SK event has a relative and an absolute time record. Relative timing between events is recorded with a 48 bit counter driven by a 50 MHz clock, with an accuracy of ~ 20 ns. The absolute time of each event is obtained from a GPS receiver, which gives each event a UTC stamp with an accuracy of ~ 10 μ s.

Outer Detector DAQ

The primary role of the OD is to tag and record events from incoming or outgoing charged particles, i.e. cosmic ray muons. In the solar neutrino analysis, the OD signals are only used as veto. An cosmic ray muon entering into the ID through the OD creates so much Cherenkov light that the DAQ is saturated and has no room for acquiring signals from solar neutrinos, which has much lower energies and thus creates much less light than a muon. The OD DAQ is designed to store hits before and after an event, in order to determine if a charged particle entered the ID during the event. If the number of OD hits is larger than the normal dark noise level, the current event is rejected as a possible solar neutrino candidate.

The signal cables from all 1885 OD PMTs are connected to “paddle cards”, in groups of 12, and each PMT hit signal is sent to a custom-built QTC (charge-to-time

converter) module. If the height of the PMT hit signal exceeds $\sim 1/2$ p.e., the QTC module generates an emitter-coupled-logic (ECL) pulse. The start time of the ECL pulse represents the time of the PMT signal, and the width is proportional to the log of the amount of charge deposited in the PMT. The ECL pulses from the QTCs are fed to LeCroy 1877 Pipeline TDCs (time-to-digital converters), where times for all leading and trailing edges of the ECL pulses are recorded. Each TDC module has 96 input channels (1 per PMT), with 5 TDC modules per Fastbus crate, and 1 Fastbus crate placed in each electronics hut.

The OD signals (hits) are only recorded if the global ID trigger has been issued. The hits are saved in a window that starts $10 \mu\text{s}$ before and ends $6 \mu\text{s}$ after the global trigger. After a global trigger, the saved TDC data is sent via a Fastbus Smart Crate Controller (FSCC) module to a Sun workstation in the central hut, where it is sent to the online host and added to the event data.

3.2.5 Triggers

There are several types of global triggers used during data acquisition at SK, and they are summed up in Tab. 3.2. The LE (low energy), HE (high energy), SLE (super-low energy), and OD (outer detector) triggers are self-generating, and are used in the normal detector operation. The HE triggered events are used in the atmospheric neutrino and proton decay analyses, and the LE and SLE triggered events are used in the solar neutrino analysis. The OD trigger is usually used as a veto trigger and to track incoming muons (as in the atmospheric neutrino analysis with upward going muons). The remaining triggers, i.e. CLK (clock), CAL (calibration), and Veto Start/Stop are externally imposed and set manually. Each trigger has a bit number, and 8 of these bits comprise the trigger word (byte), which is stamped onto each event. The trigger word indicates which triggers were on during the event.

Table 3.2: Summary of the 8 different triggers at SK.

Bit	Trigger Type	Threshold
1	LE	-320 mV (29 hits)
2	HE	-340 mV (31 hits)
3	SLE (from 5/97)	-260..-186 mV
4	OD	19 OD hits
5	CLK	external
6	CAL	external
7	Veto Start	external
8	Veto Stop	external

Hardware Triggers

Each ID ATM module generates a HITSUM signal whose height is proportional to the number of active channels in the module. The HITSUM signals from all ATM modules are analog-summed and the result is the ID HITSUM signal. If the height of the ID HITSUM reaches the threshold of a particular trigger, the trigger is issued. The threshold for the HE trigger is -340 mV (or 31 hits within 200 ns, after subtracting the average background rate), and the threshold for the LE trigger is -320 mV (or 29 hits, similarly). This is equivalent to the signal expected when 50% of the Cherenkov photons generated by 5.7 MeV electrons are detected. In May, 1997, the SLE trigger was installed in addition to the LE trigger. It had a much lower threshold of -260 mV, which was lowered several times until its final value of -186 mV, as the technology and methods improved. The SLE trigger is described in more detail below.

The OD trigger is issued in a similar manner. The OD QTCs generate a 20 mV by 200 ns square pulse each time a PMT signal exceeds the threshold of -25 mV

(1/4 p.e.). This threshold corresponds to 19 PMT hits in a 200 ns coincidence window. When the OD trigger is issued, the data is held for 100 ns, to see if a coincident ID trigger occurs. If an independent ID trigger does not occur, the OD trigger alone causes readout of the whole detector.

These 4 types of trigger (HE, LE, SLE, and OD) are fed into the hardware trigger module (TRG), where they are combined with the externally imposed triggers (CLK, CAL, Veto), a global trigger word is generated from the trigger bits, and the trigger word along with the trigger time is sent to the online computer to be merged with the PMT data.

Intelligent (SLE) Trigger

The original design of SK includes a 5.0 MeV energy threshold for solar neutrino analysis. However, the very high background rate at these low energies (gamma-rays from surrounding rock, radioactive decays from PMT glass and radon in the water) makes the data acquisition and transfer extremely difficult. Thus, a more conservative hardware threshold of 5.7 MeV (analysis threshold of 6.5 MeV) was originally adopted for the LE trigger, because the DAQ system could only handle a maximum steady-state trigger rate of ~ 30 Hz.

In special data sets taken with the SLE trigger, it was determined that the vast majority of the events below 6.5 MeV have their vertices concentrated at the perimeter of the ID (outside the nominal 22.5 kton fiducial volume). Therefore, in late 1996, effort was made to implement realtime software in order to reconstruct events online and reject those with the vertex outside the fiducial volume. This software, called the intelligent trigger (IT), was put in place in May 1997. The IT is a double vertex fit performed by two different fitter algorithms with different systematics. The fit information of each event is sent to a central computer (reformater), which discards those events that were fitted outside of the fiducial volume. The trigger rate is in this

manner decreased considerably from a raw trigger rate with the same low threshold.

In May 1997, the solar neutrino hardware threshold was lowered from 5.7 MeV to 4.6 MeV, which increased the raw trigger rate from 10 Hz (LE+HE+OD) to 120 Hz (LE+HE+OD+SLE). Because the additional 110 Hz of data (from SLE) were filtered by the fast IT computers, only 4.6 Hz of SLE events survived, and the total data transfer rate for offline reduction was increased from 10 Hz to 14.6 Hz. Given the small size of these low energy events (relatively small number of tubes are hit at these low energies), the total volume of data flow was only increased by 10%.

The efficiency and reliability of the IT was checked with both calibration sources and Monte Carlo data. The rate of rejection of good events over 4.5 MeV was measured to be $\sim 1\%$. In 1999 and again in 2000, the IT was upgraded with additional CPUs (12 in all), and it provided 100% triggering efficiency at 4.5 MeV, and 97% at 4.0 MeV. New error-correction codes raised the SLE livetime to 99.99%.

More details on the SK detector, the purification systems, the PMTs, the DAQ, and the triggers can be found in Ref. [13] and [16].

3.3 Calibration of the SK detector

In order to insure that the variables created from the simple signals of the PMTs carry real physical meaning, calibration of the detector is imperative. Proper calibration of the detector is the most important aspect of any experimental analysis, as it gives credence to the results the analysis produces. There are several quantities which need to be calibrated in any water Cherenkov detector: (a) the gain and timing of each PMT, as the basis for the electric signals; (b) the transparency of the detector water, to understand scattering and attenuation of light; (c) the energy of the electron, which can be related to the incoming neutrino energy; (d) the position of neutrino's interaction in the detector, to ensure random distribution of the neutrino events and

remove all background events, which are mostly created near the detector walls; (e) direction of the electron, which can be in general related to the direction of the neutrino; and (f) trigger efficiency, to understand how many neutrino interactions are being missed by the detector trigger electronics.

3.3.1 PMT calibration

In order to ensure the proper functioning of the detector's light sensitive parts, the relative gain, absolute gain, and timing of each PMT is calibrated using a Xe flash lamp, a Ni/Cf gamma-ray source, and a pulsed N₂ laser, respectively. The gain and timing calibrations are done for high to single photo-electron light levels. Proper understanding of the measured charge and the timing of each PMT is crucial in having confidence that the recorded signals correspond to a real, physical event in the detector.

Gain Calibration

The relative gain of each PMT is measured at light levels of 100-200 p.e., using a Xe flash lamp attached by optical fiber to a scintillator ball. The light level recorded by each PMT is corrected for attenuation, acceptance, and source uniformity, to produce a "corrected Q" for the PMT, which should be the uniform gain across all the PMTs. The high voltage of each PMT is adjusted until all of the "corrected Q" values are consistent with each other to within 7%. The remaining differences are corrected in the software.

The absolute gain of each PMT is measured at a single p.e. light level, using the nickel-californium gamma ray calibration source. Because the maximum energy of the gamma rays is ~ 9 MeV, each hit PMT detects light at the 1 p.e. level. An example of the count distribution of the single p.e. is shown in Fig. 3.8. The peak charge value in this distribution is recorded and used as the charge/p.e. conversion

factor for that channel. The mean charge/p.e. conversion factor of all ID PMTs is 2.05 pC/p.e.

Timing Calibration

The relative timing of each PMT is measured as a function of light level from 1 p.e. to several hundred p.e., by using a pulsed nitrogen laser (~ 3 ns pulse width) attached by optical fiber to a light diffuser. The timing must be adjusted for channel-to-channel variations in cable length and response time of the electronics. These measured offsets for each channel are used to generate the so-called “TQ map”, a lookup table of the relative timing offsets for each PMT as a function of the input light level. The light arrival time is shifted to earlier times as the light level increases (*slewing* effect). These corrections ensure that the timing of each PMT really corresponds to the global trigger time.

More details about the PMT calibration can be found in Ref. [13].

3.3.2 Water Transparency Calibration

Cherenkov photons in SK may traverse up to about 50 m of water before hitting a PMT on the wall. Even with ultra-pure water, the loss of light due to scattering and absorption becomes significant, and needs to be understood and corrected for. The transparency of the detector water is calibrated by injecting a laser light into the detector and measuring its intensity with a CCD camera. The long term variation in the water transparency is measured by studying the charge deposits from electrons originating from cosmic-ray muon decays.

Direct Measurement with a Laser

The parameter used to describe the transparency of the SK water is the optical attenuation length in water, and it combines the effects of scattering and absorption

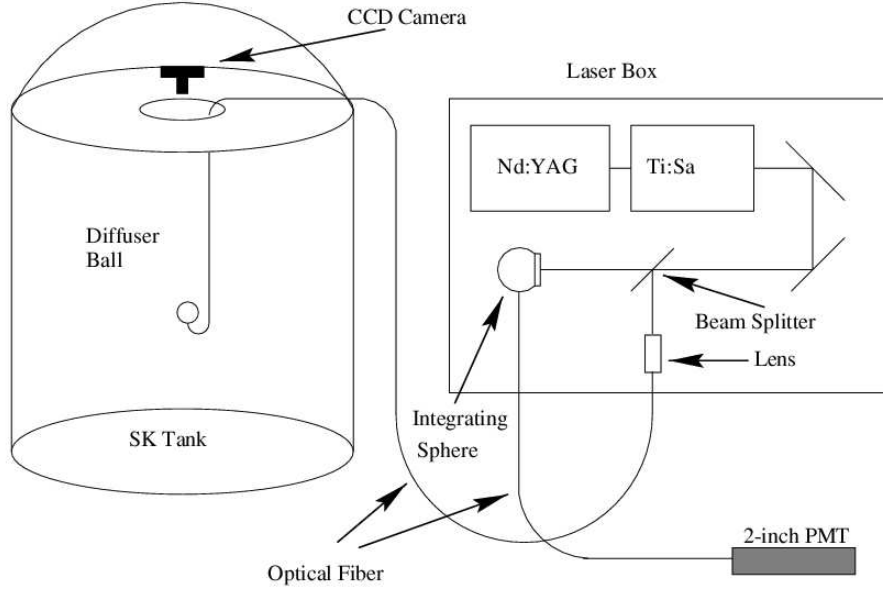


Figure 3.11: The calibration setup for the water transparency laser measurement in SK.

on the intensity of light. It can be parameterized in the following way:

$$I = \frac{I_o}{l^2} \exp(-l/\lambda), \quad \lambda = \frac{1}{\alpha_{abs} + \alpha_{scat}}, \quad (3.4)$$

where λ is the water transparency parameter, l is the distance the light travels in water, and I is the light intensity. The calibration equipment for this measurement consists of a titanium-sapphire laser, a diffuser ball, and a CCD camera. The schematic of the setup is shown in Fig. 3.11.

The laser used in this calibration is tunable, and allows for wavelength-dependent water transparency measurements (350-500 nm). The measurement is done by lowering the diffuser ball into the detector, illuminating it with the laser light via an optical cable, and imaging it with the CCD camera at the top of the detector. The stability of the laser is monitored with a PMT. The ADC counts from the PMT are used to normalize the intensity measured by the CCD camera.

The water transparency calibration is done for several wavelengths in regular time intervals, because the water quality changes in time and wavelength. The attenuation length of SK water is shown for various wavelengths in Fig. 3.12. It is measured to

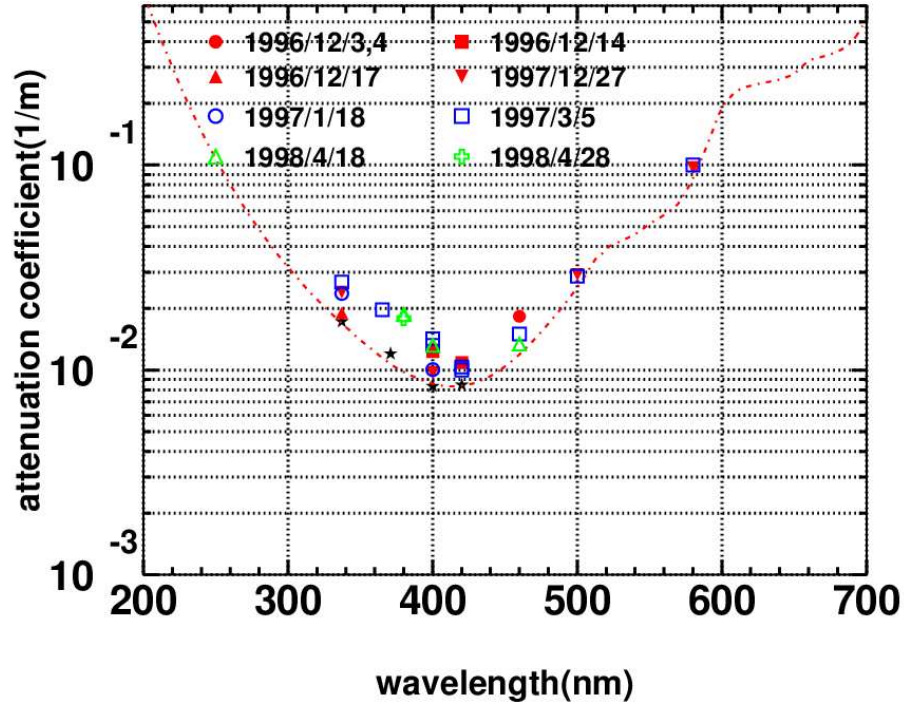


Figure 3.12: The attenuation length of Cherenkov light in SK water as a function of wavelength, measured by a tunable laser.

be 97.9 ± 3.5 m at 420 nm.

Indirect Measurement Using Cosmic Ray Muons

The long-term behavior of the light attenuation length in the water is monitored by using cosmic ray muons, and particularly the electrons resulting from the muon decays (Michel electrons). These muons rain down onto the detector continuously and abundantly (and occasionally stop in the detector), providing a great source for long-term calibration. Naturally, the Cherenkov light created by the decay electrons is not tunable in frequencies, but rather these calibrations are done for the entire Cherenkov frequency spectrum.

In this case, assuming the Cherenkov light reaching the PMTs is not scattered, the attenuation length can be parameterized in terms of the charge, Q , deposited in

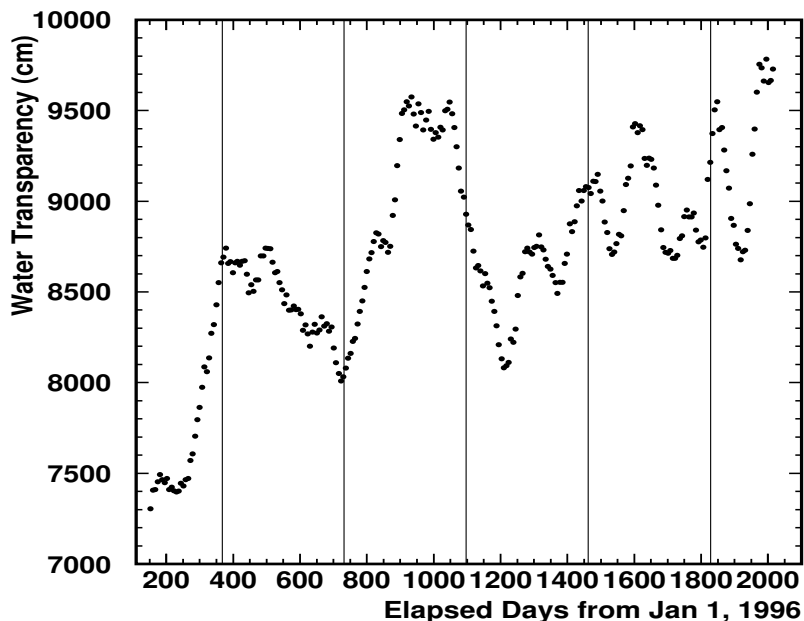


Figure 3.13: The long term variations of the attenuation length of Cherenkov light in SK water as a function of time, measured using decay electrons from cosmic ray muons.

the PMT:

$$Q = Q_o \frac{f(\theta)}{l} \exp(-l/\lambda), \quad \lambda = \frac{1}{\alpha_{abs} + \alpha_{scat}}, \quad (3.5)$$

where λ is the water transparency parameter, l is the distance the light travels in water, Q_o is a constant, and $f(\theta)$ is the relative photo-sensitive area, which depends upon the incidence angle, θ , of the light on the PMT.

The time variations of the light attenuation length of SK water is shown in Fig. 3.13. The entire data is binned up into week long bins, and each week of data is plotted as a $\log(Q)$ vs. l plot. Fitting a straight line to this plot yields the light attenuation length for that week. An example of this plot is shown in Fig. 3.14 ($N = Q$, $r = l$ in this figure), and the corresponding value for the attenuation length parameter is 9238 cm.

More details about the water transparency calibration can be found in Ref. [16].

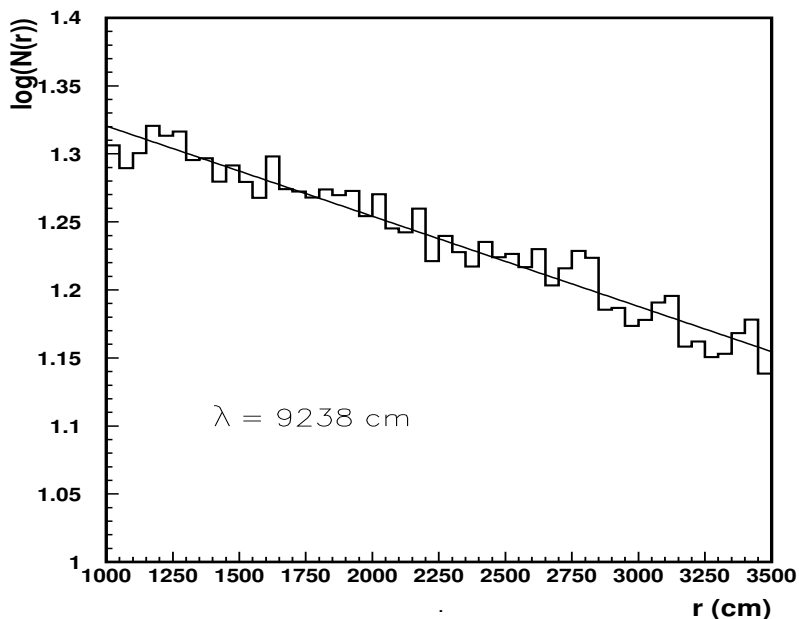


Figure 3.14: The fit to the attenuation length measurements.

3.3.3 Energy/Position/Direction Calibration

In order to perform the solar neutrino analysis at SK correctly, it is essential to understand precisely the absolute energy scale, energy resolution, position resolution, and angular resolution for low-energy (few MeV) electrons. Several calibration methods are used to accomplish this. The major ones are described here, and more details about the energy, position, and direction calibration can be found in Ref. [13], [14], [17], [18], and [19].

LINAC Calibration

An electron linear accelerator (LINAC) is used to accelerate and inject into the detector single electrons at a known energy, position, and direction. By studying the PMT signals that result from these “tuned” electrons, we can study and adjust the detector’s response to these 3 quantities. The basic setup of the LINAC system is shown in Fig. 3.15. The electron accelerator is housed in a mine cavity near the

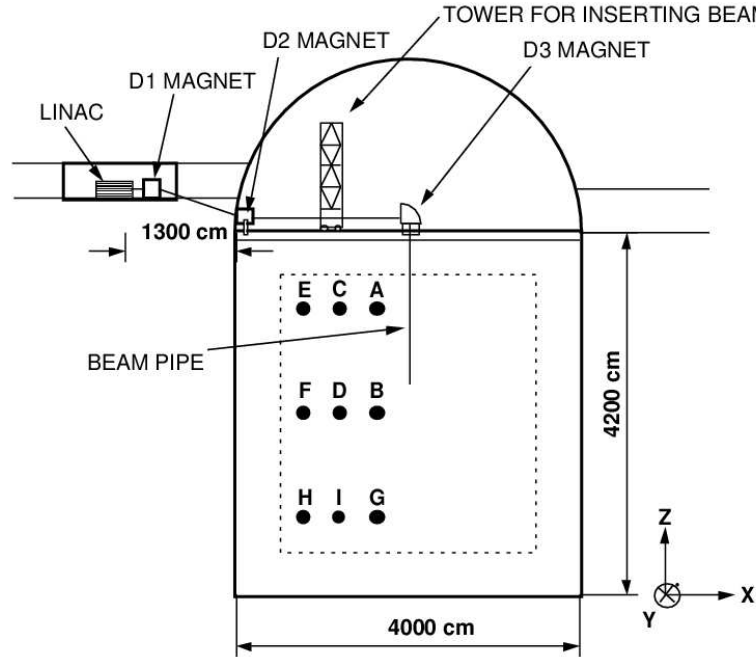


Figure 3.15: A schematic view of the LINAC calibration system. The calibration is done at the 9 injection positions indicated, in a single x-z plane.

detector. It is a Mitsubishi ML-15MIII accelerator originally designed for medical uses, with a low-current electron gun installed in order to obtain single electron flux levels. The electrons are accelerated and directed in a series of magnetically shielded, evacuated beam pipes, and finally injected downward into the detector at one of 9 different positions shown in Fig. 3.15. The end cap of the final beam pipe has a scintillator counter which is used as the external detector trigger during calibration data acquisition. The beam pipes feature an array of collimator and steering magnets at 4 different positions, in order to direct the electron beam into the end cap and straight down into the detector.

At each position, electrons are injected with 7 different energies ranging from 4.89 to 16.09 MeV. Each time, the absolute energy of the beam is measured by a germanium detector above the tank, and the beam is directed down into the detector. The electron beam is produced in the accelerator at a frequency of 60 Hz, with an

average occupancy of 0.1 electrons/spill, to minimize the number of events with more than a single electron per beam spill. An additional cut during data analysis is used to remove the rare remaining events with two or more electrons per spill.

The LINAC events are passed through the same reconstruction routines used for the solar neutrino analysis, and the energy, vertex position, and direction of the event are extracted. A sample of Monte Carlo (MC) LINAC events is also created using the detector simulation. The LINAC data is then compared to the MC data, and the detector simulation routines are tuned according to the results of this comparison. The comparison of the reconstructed event energies is shown in Fig. 3.16 for the 7 LINAC electron energies. Both the data and the MC energy distributions are fitted with a Gaussian curve. The peak energy of the data distribution is taken as the measure of the energy scale, and the 1σ width of the fit as the energy resolution at that beam energy. The deviation between the data and the MC in the peak energy ($\frac{data-MC}{data}$) is calculated for each energy and then combined into a single averaged number. This difference and all the uncertainties add up to less than 1%.

The position and direction resolution is obtained from the same LINAC data as well. The vertex position resolution is defined as the size of the sphere that contains 68% of the reconstructed event vertices, and the direction (angular) resolution as the opening angle relative to the electron injection direction that contains 68% of the reconstructed directions. The energy, position, and direction resolutions of the SK detector obtained from the LINAC data are shown in Tab. 3.3 for all 7 electron energies. The 1σ uncertainties quoted in the table are only the statistical uncertainties in the Gaussian fit to the data distribution (such as those in Fig. 3.16).

More detailed description of the LINAC calibration methods can be found in Ref. [14] and [16].

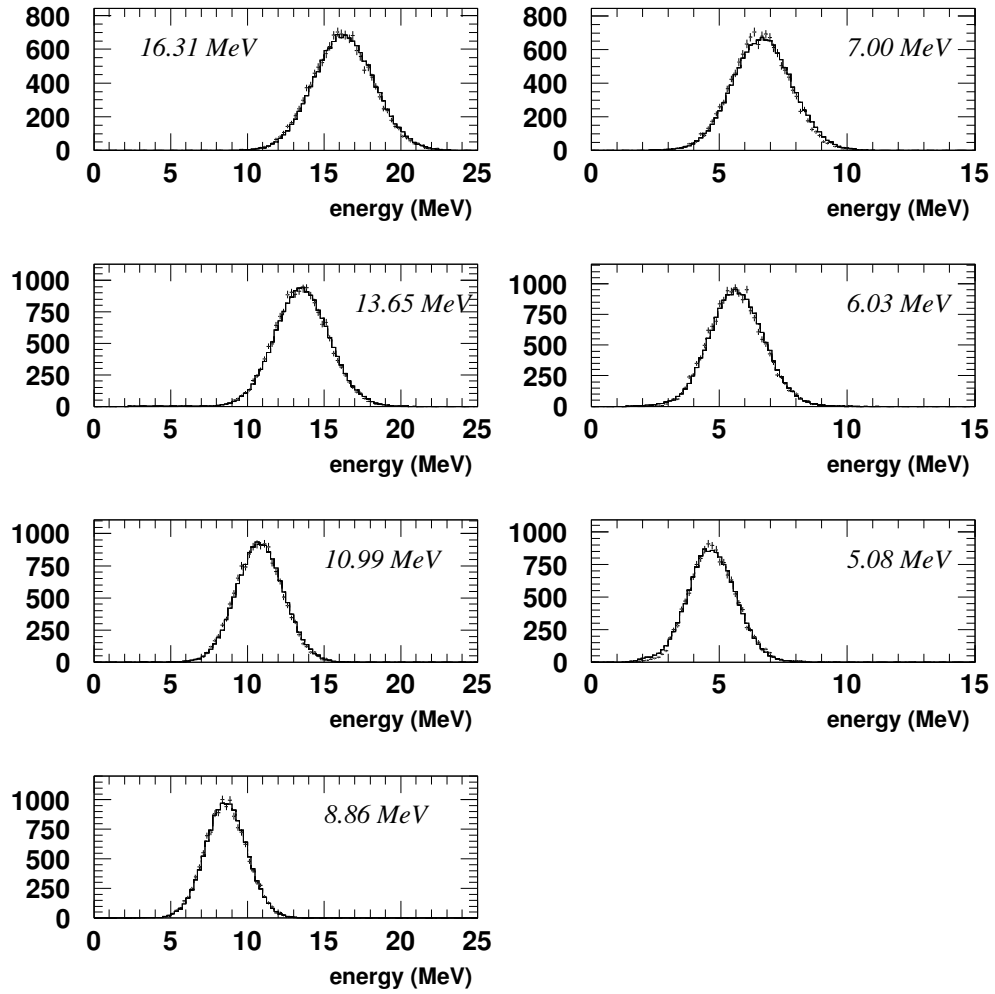


Figure 3.16: Reconstructed energy distributions for LINAC data (points) and MC (line) at 7 electron energies at the beam position $(x,z)=(-12m,+12m)$.

Table 3.3: Energy, position, and direction resolutions from LINAC data.

Energy (MeV)	Energy Resolution (%)	Position Resolution (cm)	Direction Resolution (°)
4.89	21.4±0.2	178.8±0.5	36.8±0.1
5.84	18.5±0.1	132.7±0.4	34.5±0.1
6.79	17.9±0.1	107.8±0.2	32.0±0.1
8.67	16.3±0.1	85.2±0.2	28.4±0.1
10.78	14.8±0.1	72.9±0.1	25.3±0.1
13.44	13.7±0.1	64.6±0.2	22.5±0.1
16.09	12.7±0.1	59.7±0.1	20.5±0.1

DTG Calibration

Because of the large size of the LINAC, only a few vertex positions and a downward direction of the electrons can be studied. Because of these limitations of the LINAC, the DTG (deuterium-tritium neutron generator) is used as a complementary calibration tool to the LINAC. The DTG is much smaller and more mobile. It is capable of injecting into the detector a stationary “ball” of 14.2 MeV neutrons, which excite ^{16}O into ^{16}N in the SK water. The ^{16}N then beta-decays with a half life of 7.13s, and produces gamma rays and electrons at a few well-defined energies (6.129 MeV [66.2%], 7.116 MeV [4.8%], 8.872 MeV [1.06%], none [28.0%]). These decay events are then used for energy calibration. The isotropy of the ^{16}N decay provides a good check for direction dependence of the energy scale. Because of its mobility, it can be used in all parts of the detector and thus provide a good check for position dependence of the energy scale.

The DTG is a MF Physics A-211 neutron generator, consisting of the pulse forming electronics and the accelerator head, enclosed in a stainless steel cylindrical

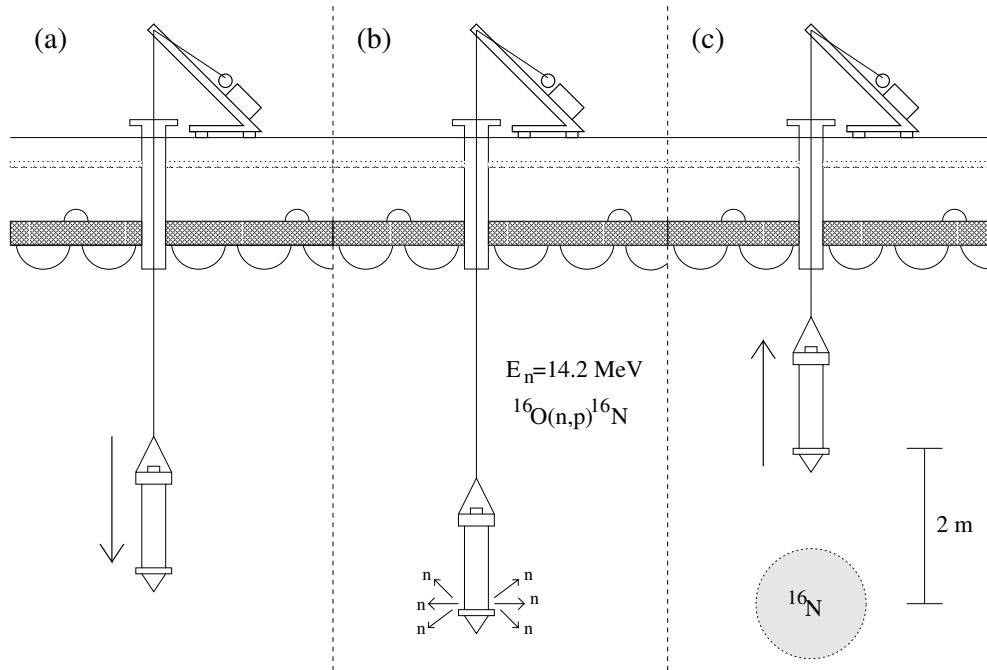


Figure 3.17: A schematic view of the operation of the DTG data taking cycle: (a) The DTG is lowered in to a position, (b) a pulse of neutrons is released, (c) the DTG is withdrawn 2 m and data is collected.

housing. The steel cylinder is attached by a cable to a crane on top of the tank, and can be lowered into the detector through one of numerous calibration holes throughout the detector top. See Fig. 3.17 for an illustration of the DTG operation. The DTG is placed in the desired position in the tank, a pulse of 14.2 MeV neutrons is emitted, and the DTG is retracted 2 m to minimize the interference of the housing on the events.

A pulse of ~ 3 million neutrons is generated by accelerating deuterium and tritium ions and colliding them with a fixed metal hydrate target in the accelerator head containing equal parts of deuterium and tritium. The neutrons are created by the following reaction:



The created neutrons then travel a mean distance of 20 cm before they generate

^{16}N in the water (by exciting ^{16}O), thus making a stationary “ball” of unstable ^{16}N atoms. The DTG is retracted as soon as the pulse is generated, and it takes about 10s to retract it 2 m. In that time 60% of the ^{16}N atoms will decay. No data is taken during this time, to avoid contamination. Once the DTG is fully retracted, data is taken from the decay of the remaining ^{16}N atoms. This cycle is repeated 25 times for each position, creating a sample of $\sim 300,000$ ^{16}N events.

The collected DTG data are submitted to the same reconstruction routines as the solar neutrino data. Due to the high number of the ^{16}N events, no special background subtraction is needed. The total contribution of the natural background to this data sample is $\ll 0.1\%$. For each DTG position, a sample of ^{16}N events is created by a MC simulation, and the events are reconstructed in the same way. The input to the MC is the known branching ratio of the ^{16}N decay, including corrections for nuclear recoil, the nuclear Coulomb field, finite nuclear corrections, Dirac wave function corrections, and atomic screening.

The energy distributions obtained from these reconstructed events from both the data and the MC samples are fitted with a Gaussian (5.5-9.0 MeV) and the peak energies are found for each position. These numbers are used as a measure of the energy scale deviation by defining the quantity $\frac{\text{data}-\text{MC}}{\text{data}}$. The global energy deviation result is obtained as a position-weighted average of all the deviations, and shown in Fig. 3.18. The agreement between data and MC is excellent.

The position and direction dependence of the absolute energy scale is also measured with the DTG data. The position dependence of the energy scale is obtained as a function of r and z by performing a position-weighted average over r and z , respectively. The direction dependence of the energy scale is obtained by dividing the data samples for each DTG position into subsamples based on the event directions, and then performing a position-weighted average over all positions, for each direction. This is done as a function of both zenith angle and azimuthal angle. The

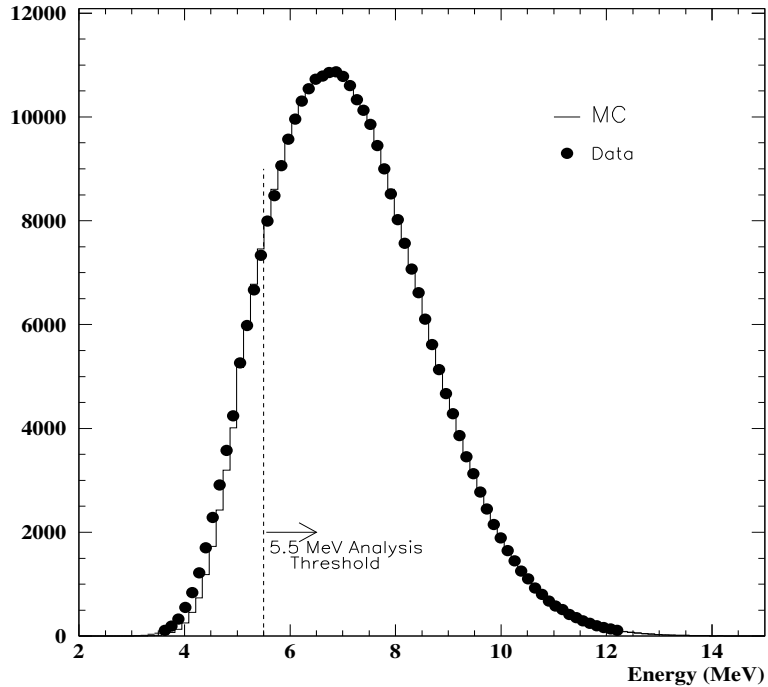


Figure 3.18: The position-weighted average energy spectrum for data (points) and MC (line), for the DTG energy calibration.

measured position and direction dependence of the absolute energy scale is used in the official solar neutrino analysis, and they are both measured to be $< 1\%$ (see Fig. 3.19 and 3.20). More detailed description of the DTG calibration methods can be found in Ref. [19].

Calibration with Nickel-Californium

Originally designed for absolute energy scale calibration, the nickel-californium calibration source is now used only as a supplement to the LINAC and DTG calibration, because of limitations due to uncertainties in the branching ratios and neutron absorption cross sections for different Ni isotopes. The source emits gamma rays by the thermal capture of neutrons on nickel wire ($\text{Ni}(n,\gamma)\text{Ni}^*$). The emitted gamma rays range in energy from 6.1 to 9.0 MeV, and are used mainly for evaluation of systematic errors and measuring trigger efficiency.

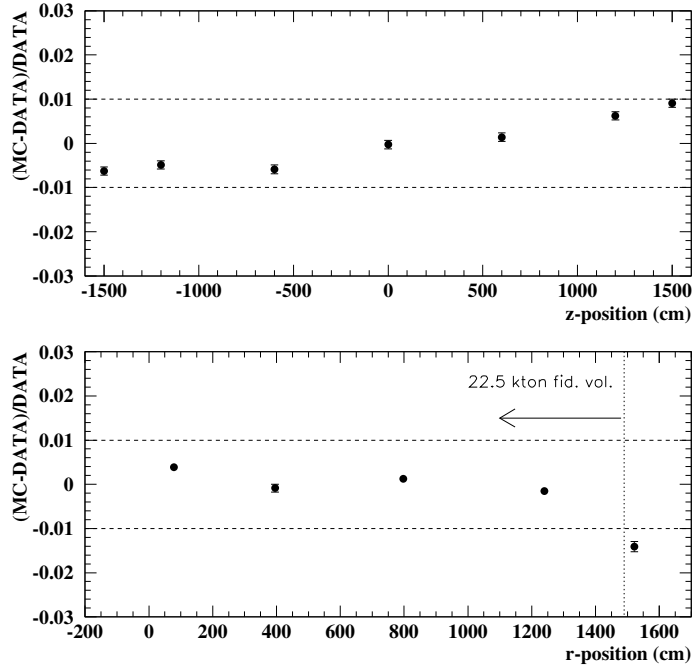


Figure 3.19: Position dependence of the energy scale as a function of z and r , measured by the DTG.

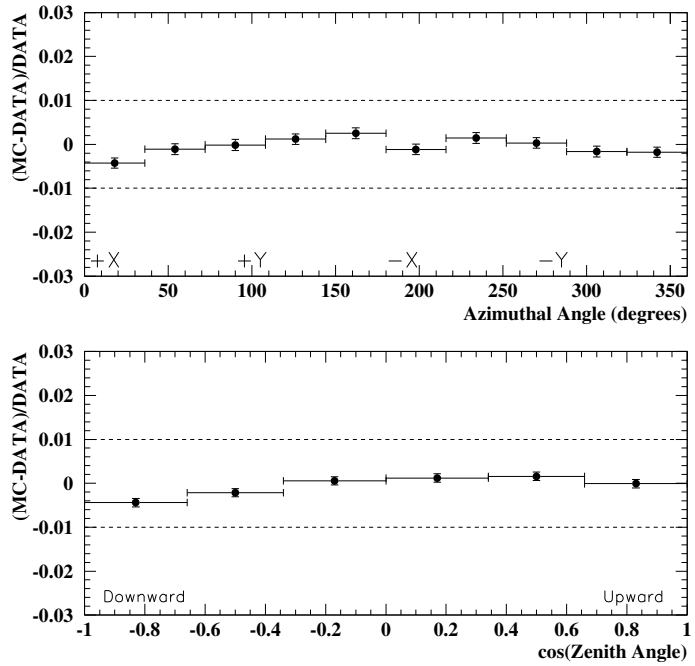


Figure 3.20: Azimuthal and zenith angle dependence of the energy scale as measured by the DTG.

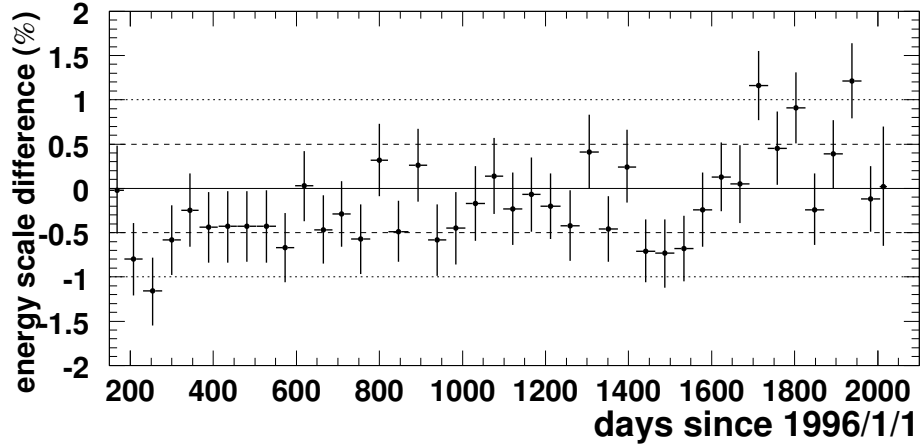


Figure 3.21: Time stability of the energy scale measured by spallation events.

Calibration with Cosmic Ray Muons μ -e Decay

Cosmic ray muons provide another way of calibrating the energy scale of the detector and checking its time and direction dependence. The muons produce two kinds of events in SK. Through-going cosmic ray muons spall oxygen nuclei and create other unstable, radioactive nuclei which subsequently decay, creating electrons and γ -rays in the energy range 3~21 MeV (spallation events). Muons with low enough energy stop in the detector (stopping muons) and decay into an electron, producing μ -e decay events in the energy range 3~70 MeV (Michel electron spectrum) with the average energy of ~ 37 MeV.

Both of these kinds of events are produced uniformly in time, position, and direction, and therefore, can be used as a check for time and direction dependence of the energy scale. The spallation events (with energies relevant for the solar neutrino analysis) are binned and the energy scale is plotted as a function of time. The time variation of the energy scale as measured by the spallation events is generally within $\pm 1\%$ (Fig. 3.21). The zenith angle variations of the energy scale is measured in a similar way, and it is less than $\pm 0.5\%$ (Fig. 3.22). More detailed description of the cosmic ray muon calibration methods can be found in Ref. [14].

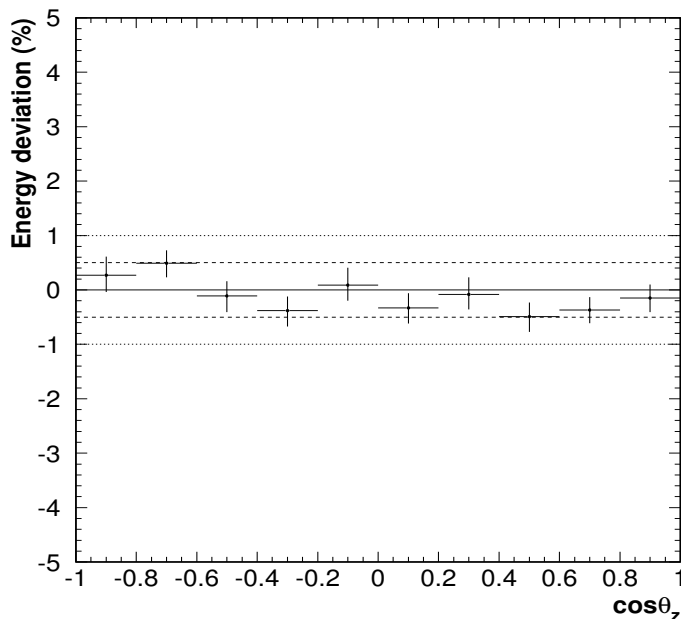


Figure 3.22: The zenith angle dependence of the energy scale as measured by spallation events.

3.3.4 Trigger Efficiency Calibration

It is important to understand the trigger efficiency of the detector, in order to be confident that events are not being randomly discarded because of some problems with the trigger mechanism. The DTG and the nickel-californium calibration sources are used to measure the trigger efficiency as a function of energy. During the calibration, an external, lower trigger of the energy threshold of -150 mV (~ 14 hits) is turned on. This trigger is low enough to ensure a 100% efficiency in the lowest energies, where the LE and SLE triggers become inefficient. The trigger efficiency, as a function of energy, is determined simply by the ratio of the number of events that passed the LE/SLE trigger to the number of events that passed the -150 mV trigger.

The measured trigger efficiency of the LE, SLE1, SLE2, and SLE3 triggers is shown in Fig. 3.23. The SLE1, SLE2, and SLE3 refer to the first three SLE threshold levels (see Sec. 3.2.5). The LE trigger becomes $\sim 100\%$ efficient above 6.5 MeV, while

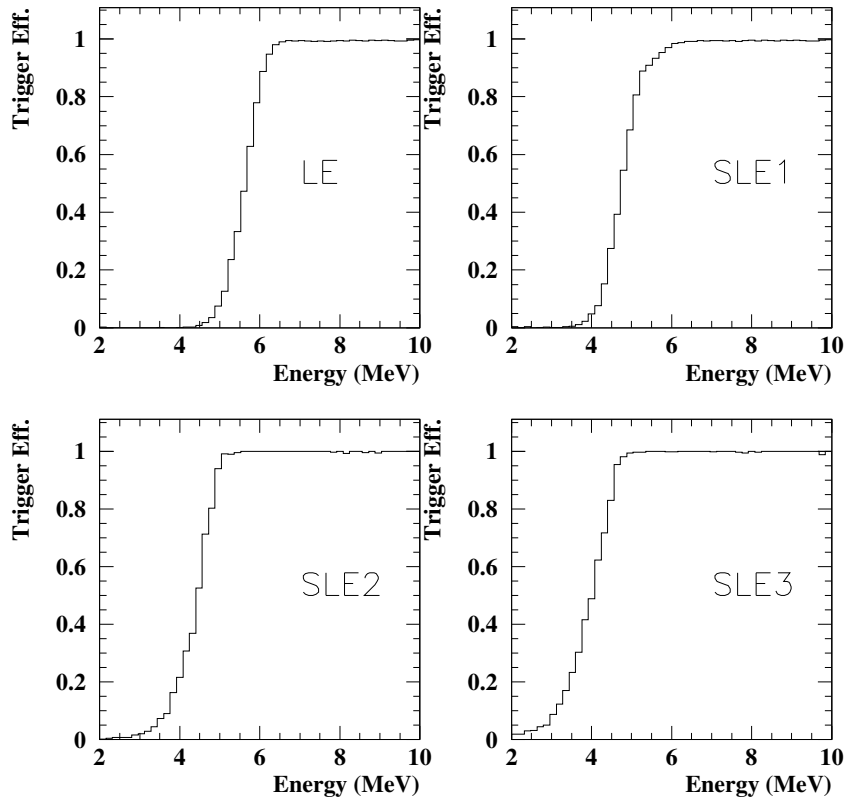


Figure 3.23: The trigger efficiency of the LE trigger and the intelligent trigger (SLE1, SLE2, and SLE3).

the latest SLE trigger reaches 100% efficiency below 5.0 MeV. This 5.0 MeV value is the energy threshold adopted in the solar neutrino analysis.

Chapter 4

Solar Neutrino Signal Extraction at SK

Having understood in depth the physical meaning of the detector's electronic signals resulting from neutrino-electron interactions in the detector, we can extract actual physical data from these saved signals. This is done offline and the process involves multiple steps. First, each event (i.e. the electron resulting from the neutrino's ES interaction) needs to be fully reconstructed. Since most events in the data sample are due to background activity, the second step in obtaining the solar neutrino signal is reducing the number of background events as much as possible. Even after the data are maximally reduced, there still remain many background events in the sample, and therefore, the signal has to be obtained with a statistical method. Thus, a MC simulation of solar neutrino events is generated, and finally, the final data set is fit to this simulated data set. The obtained solar neutrino signal is, therefore, not chosen on an event-by-event basis, but rather is the event distribution that most likely fits the simulated solar neutrino signal.

4.1 Event Reconstruction

Reconstructing each electron event involves obtaining the electron's originating position (in order to eliminate background events near the walls and check for uniformity of the event distribution), its direction (to be compared with the direction to the sun),

and its energy (to be related to the energy of the neutrino).

There are actually two kinds of events considered in the solar neutrino analysis. The events with less than the total of 1000 p.e. in all hit PMTs are treated as neutrino-scattered electrons, while the ones with more than 1000 p.e. are assumed to be cosmic ray muons and are only used in cutting out spallation background events.

4.1.1 Vertex Reconstruction

The position of the neutrino-electron interaction (i.e. the vertex of the event) is determined from the relative timing information of each hit PMT. This is done in two steps. First, the most likely PMT hits are selected as the signal hits; then the vertex position that best represents the timing of all of the selected hits is determined by minimizing the timing residuals of each hit PMT. The timing residual is the hit time of each hit PMT after it has been corrected for the photon travel time from the vertex position to the PMT. In an ideal case of a point vertex, the timing residual for each hit PMT is zero.

The most likely hits for the event are selected by initially finding the 200 ns time window (during the event time) with the most hits. An example of the time distribution of all hit tubes during an event is shown in Fig. 4.1. Times t_1 and t_4 are the *start* and *stop* times of the event, and times t_2 and t_3 are the time boundaries of the 200 ns window which contains the maximum number of hits (N_{sig}). The number of background hits (N_{bg}) is estimated from the hits outside of this 200 ns window, and the significance of the window $\left(\frac{N_{sig}-N_{bg}}{\sqrt{N_{bg}}}\right)$ is calculated. This significance was checked for progressively smaller windows, inside the initial 200 ns window, and the one with the highest significance is used in the vertex fit.

The best vertex position of the event is obtained by a fit of the selected signal hits to different vertex positions. An initial, coarse grid of vertices is defined for the entire volume of the ID, and at each position the *goodness of fit* (gof) is calculated

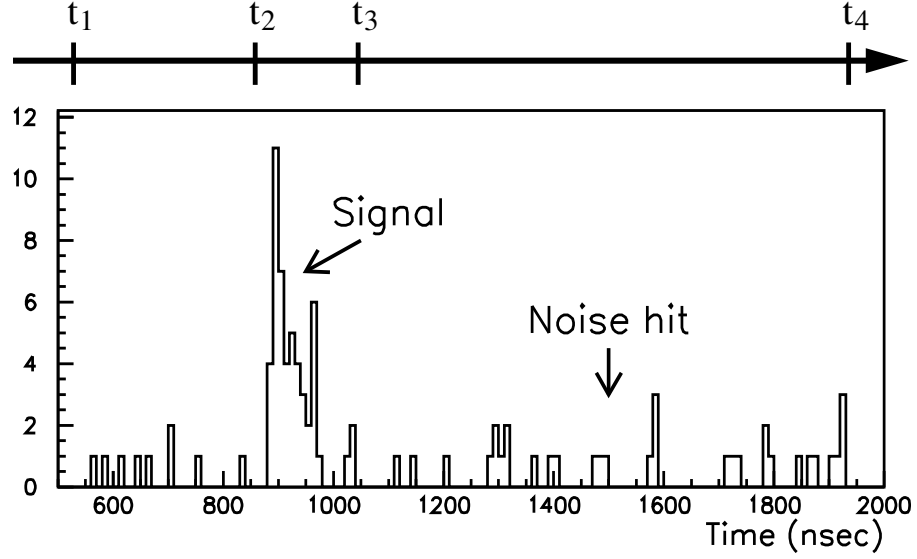


Figure 4.1: An illustration of the selection process of a typical solar neutrino candidate event.

using the timing information from all the selected hits:

$$\text{gof} = \frac{1}{N_{sel}} \sum_{i=1}^{N_{sel}} \exp\left(\frac{-t_i^2}{2\sigma_t^2}\right), \quad (4.1)$$

where N_{sel} is the number of selected signal hits, t_i is the residual time of each hit PMT, and σ_t is the timing resolution of the PMTs (5 ns). The gof has a value between 0 (bad fit) and 1 (good fit), and a typical gof distribution of LINAC events is shown in Fig. 4.2. After the vertex grid position with the highest gof value is chosen, a finer grid is defined around this best-fit position, and the fitting procedure is repeated. The final vertex position with the highest gof value is taken as the fitted vertex of the event. The vertex (position) resolution is measured by the LINAC calibration system (Sec. 3.3.3), and is found to be ~ 73 cm for 10 MeV electrons.

More details of the vertex reconstruction method can be found in Ref. [18].

4.1.2 Direction Reconstruction

Once the most optimal vertex position is found for an event, the direction of the electron is reconstructed using the conical pattern of the Cherenkov light emitted

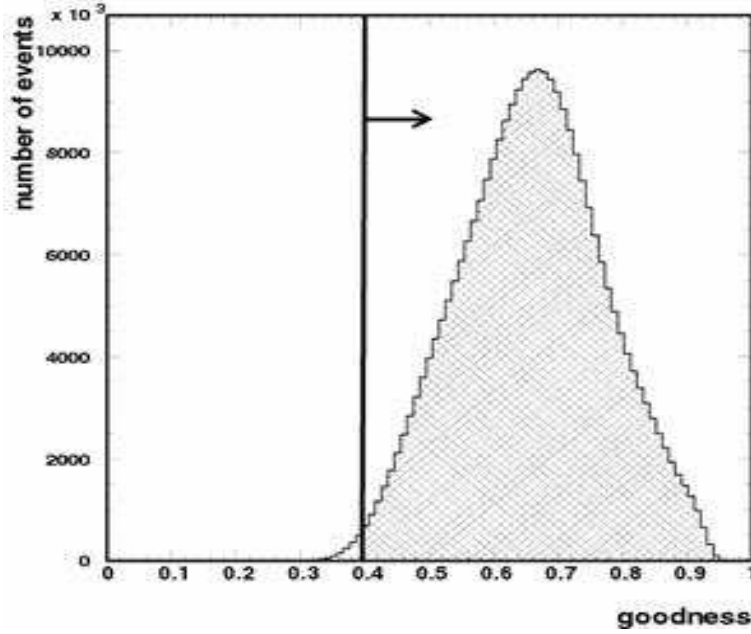


Figure 4.2: Distribution of goodness of fit values for electron events. The cut value of 0.4 is shown (see Sec. 4.2.2).

due to the electron. This is done by checking different trial electron directions about the vertex and maximizing a likelihood function based on the photon directions to the hit PMTs:

$$\mathcal{L}(dir) = \sum_i \log[f(\cos\theta_{dir})]_i \frac{\cos\theta_i}{a(\theta_i)}. \quad (4.2)$$

The quantity θ_{dir} is the angle between the trial direction and the direction from the vertex to the i^{th} hit PMT. The function f is the relative probability distribution that a Cherenkov photon is emitted at a given angle relative to the direction of the electron. This distribution is shown in Fig. 4.3(a), and is generated by a MC simulation of 10 MeV electrons. The distribution peaks at 42° and it features broad tails stemming from multiple Coulomb scattering of the electron and scattering of Cherenkov light in the water. The quantity θ_i is the angle between the direction normal to the i^{th} hit PMT and the direction of the incident photon (direction to the vertex). The function $a(\theta_i)$, shown in Fig. 4.3(b), is a correction factor for the

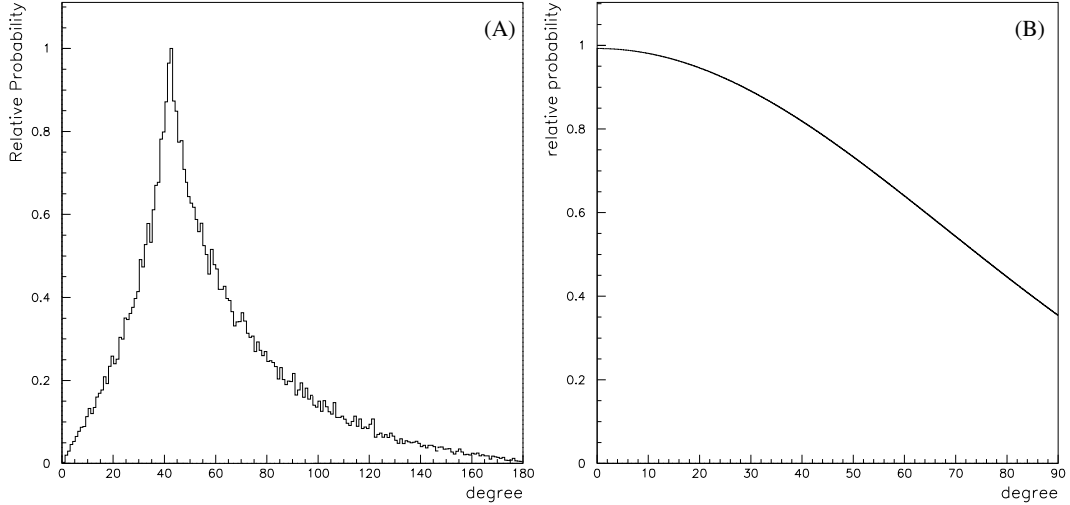


Figure 4.3: (a) Relative probability distribution $f(\cos\theta_{dir})$ of Cherenkov photon directions with respect to the electron direction; (b) angular acceptance correction ($a(\theta_i)$) used for the PMTs as a function of the photon incident angle.

acceptance of the PMT photocathode as a function of the photon incident angle.

The most likely direction of the recoil electron is chosen by varying the trial direction in successively smaller steps until the direction that maximizes this L likelihood function is found. This direction is taken as the reconstructed direction of the event. The direction resolution is measured with the LINAC calibration system, and is found to be $\sim 25^\circ$ for 10 MeV electrons.

More details of the direction reconstruction method can be found in Ref. [18].

4.1.3 Energy Reconstruction

After obtaining the vertex position and the direction of the event, the energy of the event (i.e. the recoil electron's energy) is reconstructed. Instead of using the information of the deposited charge on each PMT, at Super-Kamiokande we use the total number of hit PMTs in the calculation of the energy. The main reason for this is that roughly 6 photoelectrons are collected per MeV of energy. This means that in the energy range relevant to the ^8B solar neutrino analysis at SK ($5 \sim 20$ MeV),

there will be very few PMTs collecting more than a single photoelectron during any event. Therefore, in order to avoid the difficulties associated with the poor charge resolution ($\sim 50\%$) of PMTs near the single p.e. level as well as the small changes in the collected charge from electronic noise, the total number of hits, N_{hit} , is used as the energy quantity.

The total number of hits, N_{hit} , is determined by counting all the hits whose timing residuals, calculated in the vertex reconstruction, fall within a 50 ns window (sometimes N_{hit} is referred to as N_{50} , for this reason). This is done in order to minimize the contamination of the signal with noise hits. The N_{hit} is then corrected for the known detector, position, and time dependent effects (these include light attenuation in water, PMT dark noise, multiple photoelectrons, geometrical acceptance), and a quantity N_{eff} is constructed.

The N_{eff} is defined as follows:

$$N_{eff} = \sum_{i=1}^{N_{hit}} \left[(X_i + \epsilon_{tail} - \epsilon_{dark}) \frac{N_{all}}{N_{oper}} S(\theta_i, \phi_i) \exp\left(\frac{r_i}{\lambda(run)}\right) G_{kek}(i) \right], \quad (4.3)$$

and the various components of the N_{eff} are:

- X_i is the expected number of photoelectrons in a hit PMT, based on the occupancy of the nearest neighbor PMTs. The occupancy is the ratio ($x_i = \frac{n_i}{N_i}$) of the number of hit tubes in the neighboring 3×3 PMT patch to the number of alive PMTs that could have been hit (N_i). The value X_i is then calculated using Poisson statistics and the assumption of a uniform light level over the 3×3 PMT patch:

$$X_i = \begin{cases} \ln[(1 - x_i)^{-1}], & x_i < 1 \\ 3.0, & x_i = 1. \end{cases} \quad (4.4)$$

The value at $x_i = 1$ is obtained by extrapolation.

- ϵ_{tail} is a correction to N_{hit} for the reflected light outside of the 50 ns time window. The number of hits is calculated in a 100 ns window, and the correction

is defined as:

$$\epsilon_{tail} = \frac{N_{100} - N_{50}}{N_{50}}. \quad (4.5)$$

- ϵ_{dark} is a correction to N_{hit} for the dark noise during the 50 ns time window. It is defined as:

$$\epsilon_{dark} = \frac{N_{alive} R_{dark} 50 \text{ ns}}{N_{50}}, \quad (4.6)$$

where N_{alive} is the number of alive PMTs, and R_{dark} is the measured average dark noise rate for the current run.

- $\frac{N_{all}}{N_{oper}}$ is a correction for the number of dead PMTs in the detector as a function of time. N_{all} is the total original number of PMTs in the ID (11,146), and N_{oper} is the number of operational PMTs during the current run.
- $S(\theta_i, \phi_i)$ is the effective photocathode area of each hit PMT as a function of the photon's incident direction angles, θ_i and ϕ_i . The present ϕ asymmetry is caused by the shadowing of nearest neighbor PMTs at large values of θ .
- $\exp\left(\frac{r_i}{\lambda(run)}\right)$ is a correction for light attenuation as the photon travels a distance r_i from the vertex to the PMT. The relative water transparency, $\lambda(run)$, is measured weekly using the decay electrons of stopping cosmic ray muons (see Sec. 3.3.2).
- G_{kek} is a quantum efficiency correction factor for the PMTs. This correction comes from the fact that 375 PMTs (the so-called KEK PMTs) were manufactured before the main set of PMTs, and were found to have slightly higher quantum efficiency. Thus a correction factor must be applied:

$$G_{kek} = \begin{cases} 0.833, & \text{for 375 KEK PMTs} \\ 1.000, & \text{for all other PMTs.} \end{cases} \quad (4.7)$$

The N_{eff} defined in this way is designed to return a uniform value over the entire fiducial volume and all run periods.

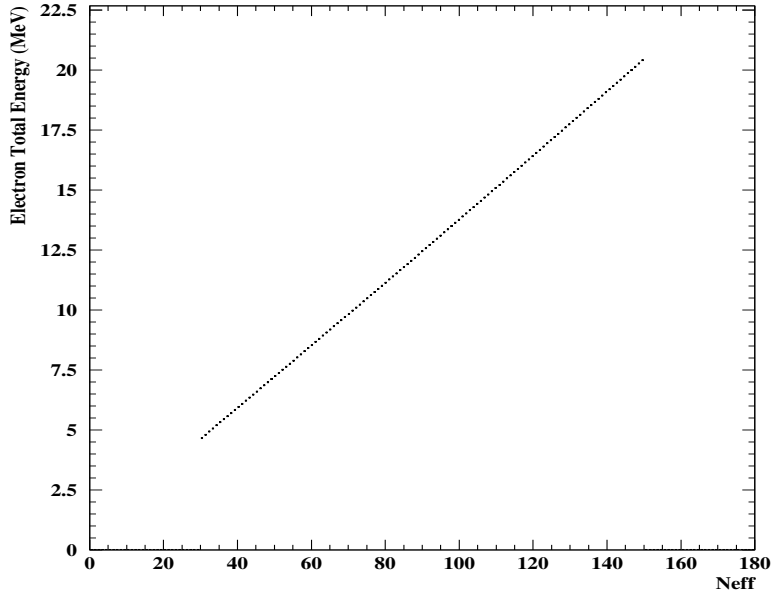


Figure 4.4: The N_{eff} -to-energy translation function obtained by a LINAC-tuned MC simulation.

The final step in reconstructing the event energy is to convert the N_{eff} value into electrons total energy. The N_{eff} -to-energy translation function is obtained by a special MC simulation of mono-energetic electrons tuned with the results from the LINAC energy calibration (see Sec. 3.3.3), and is shown in Fig. 4.4. All 7 electron energies from LINAC (see Fig. 3.16) are used in the tuning, and the position dependence of the energy calibration is checked with the DTG and Nickel calibration, and decay electrons from cosmic ray muons. The tuned MC simulation very faithfully reproduces the LINAC calibration data. The largest deviation of the MC peak energy from the LINAC data for any electron energy and LINAC position is 1.3%. The largest deviation in energy resolution is 4.7%. The energy resolution was measured to be 14.8% for 10 MeV electrons.

Some more details about the energy reconstruction method can be found in Ref. [18].

4.1.4 Muon Track Reconstruction

Cosmic ray muons pass through the detector at an average rate of ~ 2 Hz. As they travel in the water, they can interact with an ^{16}O nucleus, and produce radioactive spallation products. The decays of these spallation products often resemble the solar neutrino events, and represent the dominant contribution to the background in the solar neutrino data sample at energies above 7 MeV. Fortunately, these background events have a strong temporal and spatial correlation to the path of the parent muon, and can, therefore, be tied rather efficiently to the muon track and thus removed from the data set by a likelihood analysis (see Sec. 4.2.3).

In order to later perform this spallation background reduction, all muons found at SK are fitted with a muon track fitter, which determines the entry and exit points of the muon, as well as its track through the water. The entry point of the muon is identified as the earliest cluster of in-time hit PMTs, during a muon event. The exit point is identified as the largest cluster of high-charge PMT hits, since the Cherenkov cone gets progressively smaller as the muon approaches the wall. The muon track is simply a straight line between the entry and exit points. This simple reconstruction algorithm works well for $\sim 85\%$ of the muons. The muon track resolution is measured with a MC simulation to be 67 cm.

The various algorithms of the reconstruction of cosmic ray muons (such as “muboy”) are described in much more detail in Ref. [14], [18], and [20]. The muon track fitters are designed to fit through-going muons, stopping muons, and multiple muons.

4.1.5 SLE Reconstruction Tools

With the introduction of the SLE triggered events (events below 6.5 MeV) to the solar neutrino data sample, additional reconstruction tools had to be developed to reconstruct these low energy electron events and separate them from low energy background. These two new vertex reconstruction tools are the new goodness cut

and clusfit.

New Goodness Cut

The new goodness cut is designed to separate the true electron Cherenkov ring-like events from the background events that have small, tightly spaced clusters of hit PMTs, presumably originating from gamma ray activity near the PMT glass. These background events produce PMT hits very close in position and time, and are often reconstructed inside the fiducial volume, because the original vertex fitter has little power to differentiate between widely separated trial vertex positions. True electron events inside the fiducial volume produce PMT hits with a noticeable separation in position and time, and only the true vertex will return a good fit.

The new goodness cut exploits this fact, and makes use of an additional fit to a $10\text{ m} \times 10\text{ m}$ grid of vertex positions, perpendicular to the fitted direction of the event, with the original fitted vertex in the center of the new grid. The same “gof” value (see Sec. 4.1.1) is again calculated at each trial vertex point, and a goodness fraction (“goodfrac”) is calculated:

$$\text{goodfrac} = \frac{N[\text{gof}_i > (\text{gof}_o - 0.2)]}{N_{tot}}, \quad (4.8)$$

where gof_i is the goodness of fit value for each new vertex grid point, gof_o is the goodness of fit value of the original vertex, N is the number of grid points with $\text{gof}_i > (\text{gof}_o - 0.2)$, and N_{tot} is the total number of grid points. The value of this “goodfrac” is used in the new goodness cut in removing these background events (see Sec. 4.2.4).

Clusfit

Clusfit is simply another vertex reconstruction algorithm, different from the original one. Using a different hit selection method gives non-physical, background events

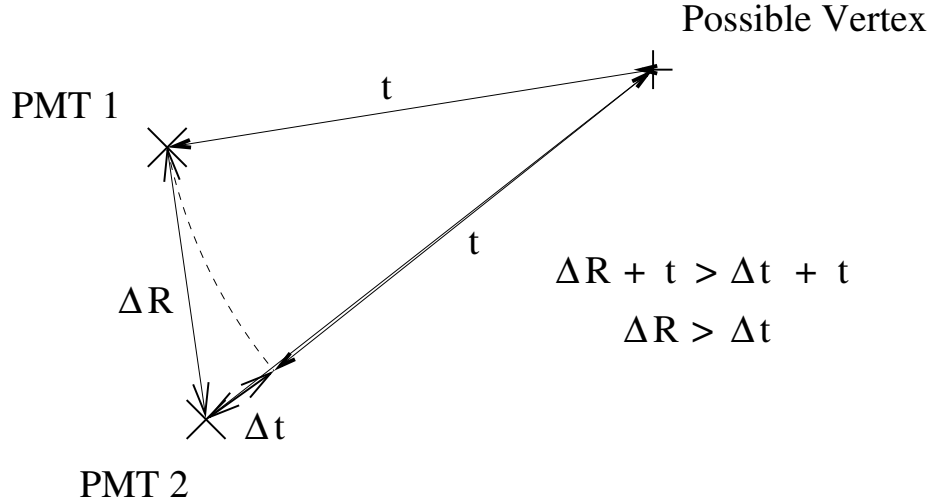


Figure 4.5: Triangle relation between pairs of hit PMTs used in clusfit. The pair is considered correlated if the relation $\Delta R > \Delta t$. A constant light speed of 21.6 cm/ns is assumed.

another chance to be fit outside of the fiducial volume. Good electron events inside the fiducial volume will most likely reconstruct in the same position, so adding another fitter provides an additional separation between physical and background events.

The hit selection method is similar to the SLE online vertex fitter (see Sec. 3.2.5). First, a causality check is performed on all hits, and only the hits within 1250 cm and 35 ns of any other hit are selected. Next, each hit is paired with another event and the pair is only kept if it satisfies the triangle relation shown in Fig. 4.5. The relation states that the spatial separation of the two hits (ΔR) must be greater than the difference in their hit times (Δt), assuming a constant light speed of 21.6 cm/ns. The largest set of these mutually correlated hit pairs is used in the clusfit vertex grid fitter.

The grid fit is similar to the original vertex fit, with the grid points arranged in a cylindrical pattern, providing more opportunities for the vertex to be fitted outside of the fiducial volume. Progressively smaller grid sizes are used until a final

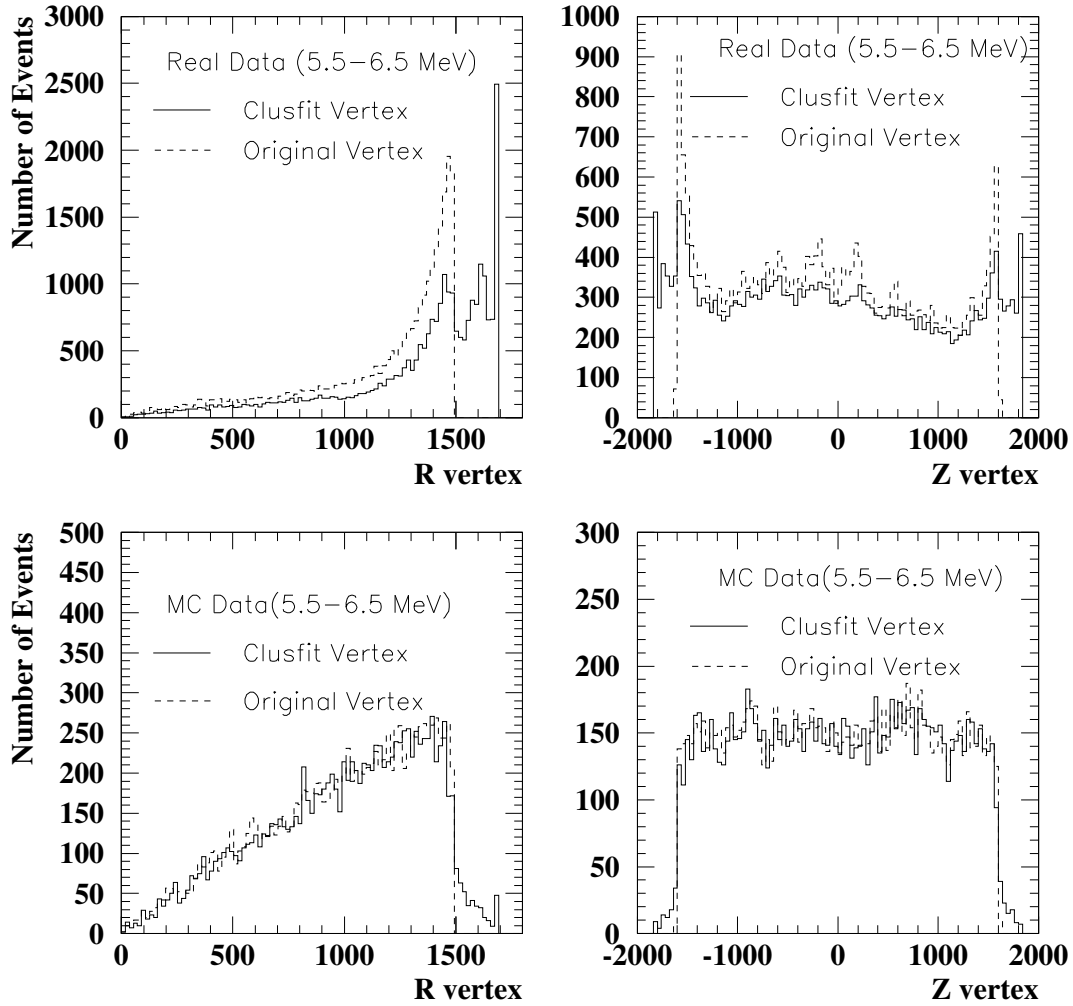


Figure 4.6: A comparison of the vertices reconstructed by clusfit and by the original vertex fitter. Both real events and MC simulated events are shown for electron energies between 5.5 and 6.5 MeV.

reconstructed vertex position is found.

Fig. 4.6 shows a comparison of the vertex positions reconstructed by the clusfit and the original vertex fitter. The comparison is shown as a function of r and z position coordinates, and features both the real solar neutrino candidate data set and its MC simulation. Only events that were fitted by the original vertex fitter inside the fiducial volume are shown in the comparison. It is clear from the figure that clusfit fits a good number ($\sim 25\%$) of the background data events outside of the fiducial volume, while it leaves the MC distributions (i.e. the physical events)

virtually unaffected ($<5\%$). The clusfit vertex distribution is used in the clusfit cut in order to remove some of this non-physical background (see Sec. 4.2.4).

4.2 Data Reduction

Most of the reconstructed events in the data set of solar neutrino candidate events come from background sources and need to be removed from the final data sample, before a physical signal can be extracted. This background removal is done at SK in three main steps. The first step of data reduction is removing the “obvious” background events, such as electronic noise, “flashing” PMTs, poorly fit events, events that triggered the OD (signaling an incoming charged particle), and events outside of the fiducial volume (2 m from the walls). On their way through the detector, the very energetic, cosmic-ray muons create many radioactive, unstable elements, which decay and produce events that sometimes closely mimic solar neutrino events. These are removed in the second step by essentially removing any event that happens within a certain volume and time of the muon track. The final reduction step is removing events that didn’t fit carefully determined properties of known good events, such as goodness of vertex fit, resemblance of gamma-rays from the surrounding rock, and further fiducial volume considerations.

The final data sample, events remaining after all the reduction steps have been performed, is reduced from the initial data set by $\sim 99.83\%$. Although most of the background in the data is removed in these reduction steps, there still remains a considerable amount of background events in the data sample, mostly due to radioactive decay of radon in the water and the surrounding rock.

4.2.1 Organization of the Data

At SK, all data events are collected into runs. Runs are the most basic sets of events, with a maximum time period of 24 hours. They are started and stopped manually and are incremented each time either something is done with the detector (calibration, etc.) or there is any break in the normal data acquisition. The runs are subdivided into subruns, which last for 60 – 900s (depending on the trigger rate), and are started and stopped automatically by the online DAQ system.

A good run is defined as normal data acquisition period lasting longer than 5 min. A good subrun must last at least 30s, because shorter subruns occur usually at the end of a run and may contain incomplete events. Furthermore, the rate of events identified as coming from flashing PMTs, electronic noise, or incomplete PMT data must not exceed a set threshold before either a run or a subrun is labeled as good. Only events from good runs and subruns are used in the data analysis and are subjected to the data reduction routines.

As was mentioned earlier (Sec. 4.1.4), there are two kinds of events considered in the solar neutrino data analysis: solar neutrino candidate events, with less than 1000 p.e. (~ 100 MeV); and cosmic ray muon candidate events, with more than 1000 p.e. Only the solar neutrino candidate events are passed through the reconstruction routines, while the muon candidate events are saved separately, reconstructed with the muon track fitter (Sec. 4.1.4), and used in the spallation events removal (Sec. 4.2.3). The separation of these two kinds of events is shown in Fig. 4.7.

4.2.2 First Reduction

The first background reduction is designed to remove the background events from electronic noise and other events that are clearly not solar neutrino candidate events.

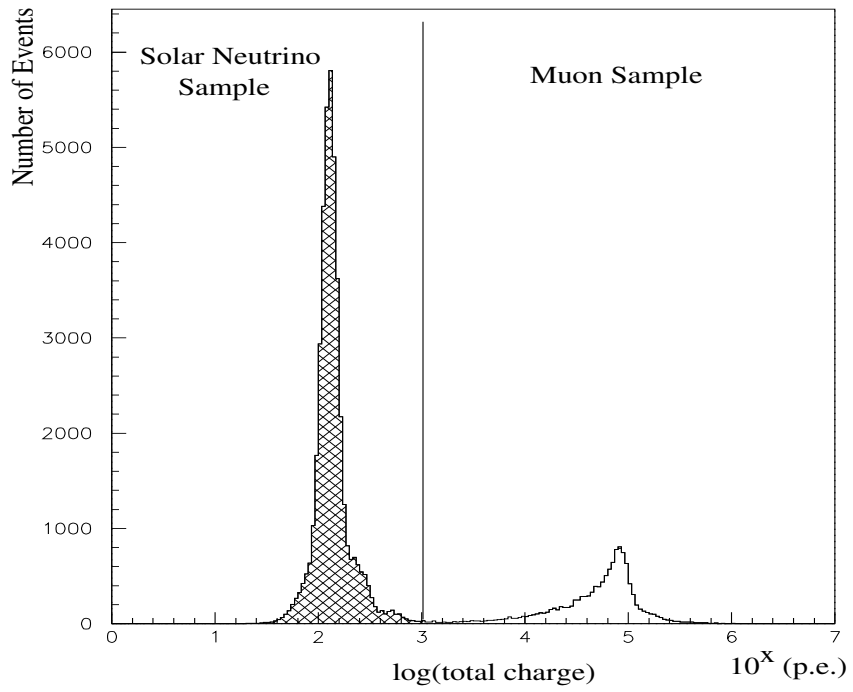


Figure 4.7: Distribution of the total charge of events in the solar neutrino data sample. Events with less than 1000 p.e. are considered to be solar neutrino candidate events; and events with more than 1000 p.e. are considered to be cosmic ray muon events.

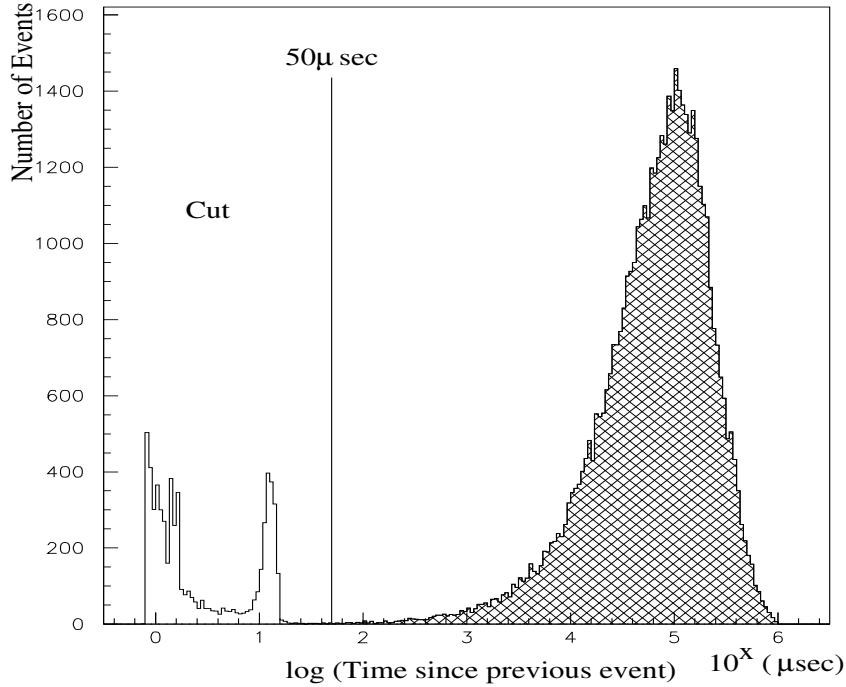


Figure 4.8: Distribution of event times since last event. The cut value of $50 \mu\text{s}$ is shown.

- **Initial online cuts.** The events marked by the online DAQ system as incomplete or ones that were collected during an ATM self-calibration cycle are immediately removed from the data sample and are not considered for further reduction. Also the events containing only a periodic trigger or veto stop/start triggers are removed.
- **Fiducial volume cut.** Events whose vertex is reconstructed (outside the 22.5 kt fiducial volume (within 200 cm of the ID walls) and the events for which the reconstruction algorithm failed are removed.
- **Time difference cut.** This cut removes events that follow too closely (within $50 \mu\text{s}$) of another event. The timing distribution of all events as a function of the time after the previous event is shown in Fig. 4.8. This removes decay electron events as well as events caused by “ringing” of the DAQ electronics, which is typically effect of the electronics after a very large event.

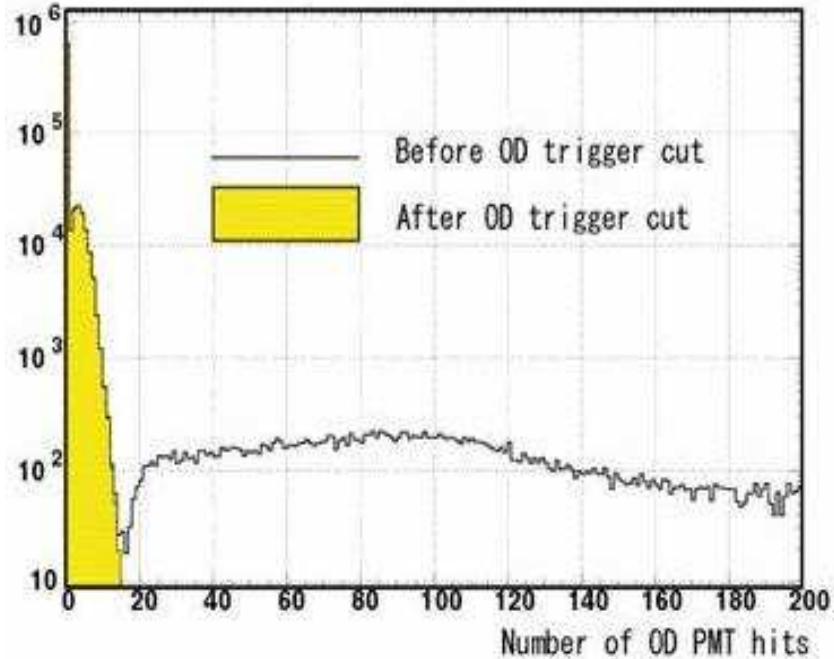


Figure 4.9: Distribution of the number of hit OD PMTs for all events.

- **OD triggered events cut.** Events triggered by the OD trigger and events with more than 20 OD PMT hits are removed, in order to prevent data contamination from entering charged particles. Fig. 4.9 shows the distribution of the number of hit OD PMTs for all events.
- **Poor fit cut.** This cut removes events with the goodness of fit (gof) value from vertex reconstruction of less than 0.4. Many background events have low gof values, and will therefore will rejected by this cut. Fig. 4.2 shows the distribution of gof values and the cut value at 0.4.
- **First electronic noise cut.** Background events from electronic noise have typically a large fraction of hit PMTs with a relatively low amount charge per PMT. If the fraction of hit PMTs with less than 0.5 p.e. per PMT channel exceeds 40% ($NSratio > 0.4$), the event is tagged as electronic noise, and is removed. Fig. 4.10 shows the distribution of the NSratio variable and the cut

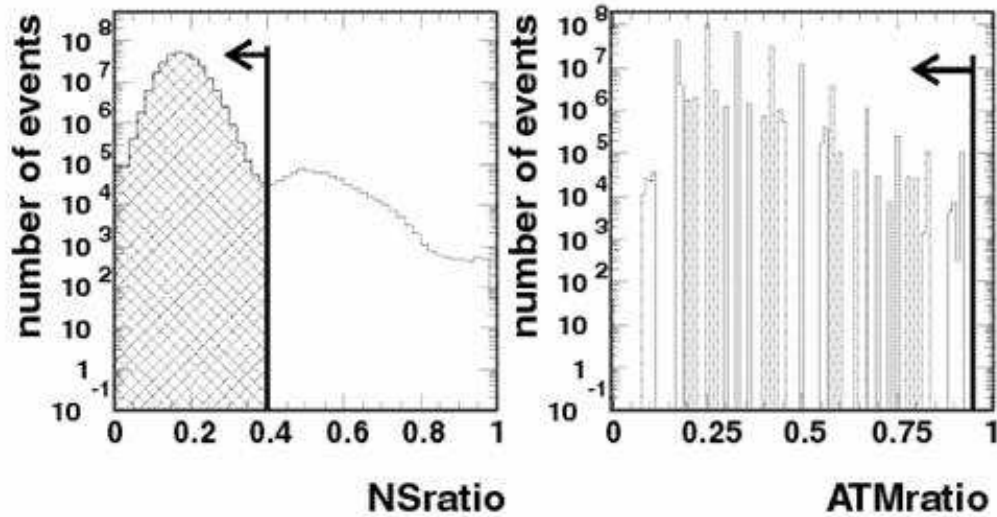


Figure 4.10: Distributions of the NSratio variable (used in the first electronic noise cut) and the ATMratio variable (used in the second electronic noise cut).

value of 0.4. One identified source of such noise events is failing fluorescent lights in electronics huts.

- **Second electronic noise cut.** Another indication that an event is electronic noise is if most of the event’s hits come from a single ATM board. The event is tagged as background, and removed, if more than 95% of the PMT hits originate in the same ATM ($\text{ATMratio} > 0.95$). Fig. 4.10 shows the distribution of the ATMratio variable and the cut value of 0.95.
- **Flasher cut.** This cut removes events which originate in “flashing” PMTs. Flashing PMTs generate an internal electrical arc which causes a flash of light. These flashing events usually have a single PMT hit with a high charge value and a cluster of hits in the neighboring PMTs. If any hit has more than 50p.e. of charge and is accompanied by 5 or more hit nearest neighbors, the event is removed. Fig. 4.11 shows the distribution of hits in the detector for a typical flasher event.

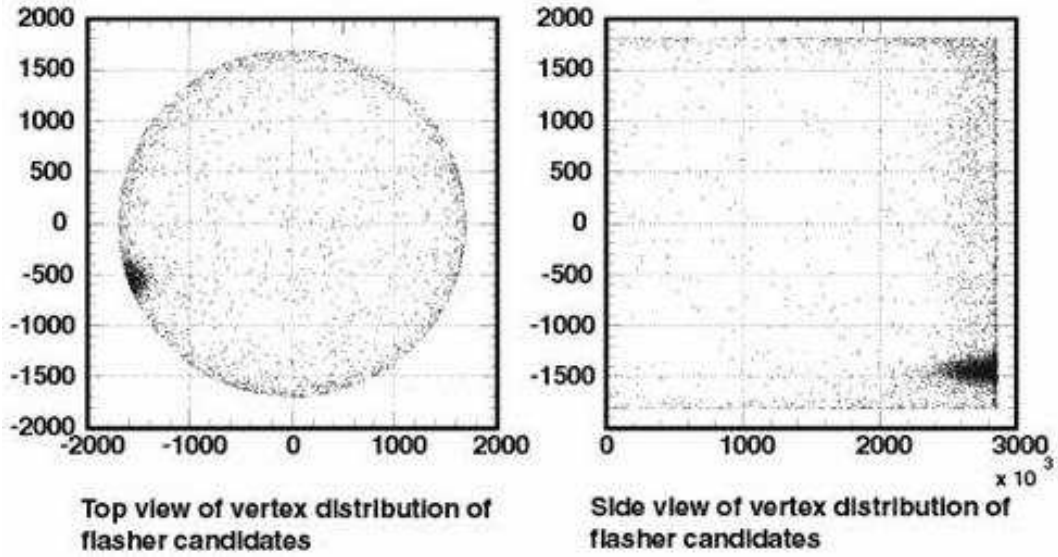


Figure 4.11: Distributions of the PMT hits in the detector for a typical flashing event.

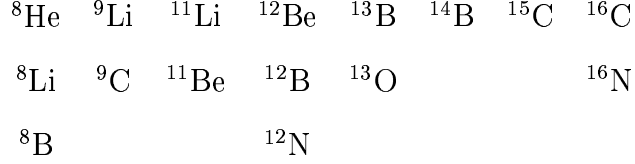
- **External flasher cut.** Events with the reconstructed vertex near the true one (i.e. good events) should have a uniform hit distribution around the reconstructed direction. On the other hand, poorly reconstructed events (reconstructed vertex far from true vertex) may have a non-uniform hit distribution. The direction variable, *dirks*, is used as the measure of this uniformity, and is obtained by a Kolmogorov-Smirnov (KS) test for the hit PMT with respect to the reconstructed direction. Any event with $\text{gof} < 0.6$ and $\text{dirks} \geq 0.25$ is removed.

4.2.3 Removal of Spallation Events

Spallation products are unstable nuclei produced by cosmic ray muons passing through the detector and interacting with an oxygen nucleus:



where X is a spallation nucleus, and it includes:



These nuclei β -decay with half-lives ranging from 8.5 ms (${}^{11}\text{Li}$) to 13.8 s (${}^{11}\text{Be}$) and produce events in the energy range of 1 \sim 20 MeV. These events represent the dominant background contribution to the solar neutrino candidate events with energies above 7 MeV. They are correlated in time and vertex position to the track of the parent cosmic ray muon, and can, therefore, be removed by a likelihood analysis.

The likelihood function used in the correlation of the spallation events to the muon track is described in detail in Ref. [21]. It assigns a likelihood value to each event, dependent upon how closely it is correlated in time and space with the muon track. It uses three correlation variables (Δl , Δt , Q_{res}) in the process:

- Δl is the closest distance from the event vertex position to the muon's reconstructed track.
- Δt is the time difference between the event and the muon track.
- Q_{res} is the residual charge of the muon as it passes through the water:

$$Q_{res} = Q_{\mu} - p(t)L, \quad (4.10)$$

where Q_{μ} is the total charge deposited in the water by the muon, $p(t)$ is the expected amount of collected charge per unit path length, and L is the total path length of the fitted muon track. The parameter p has a nominal value of 24.1 p.e./cm, and is corrected for time variations in water transparency.

This likelihood value is determined separately for muons with completely reconstructed tracks (using Δl , Δt , and Q_{res}) and muons with a failed track fit (using only Δt , and Q_{res}). Each event is compared to the previous 200 muons, and the largest likelihood value is used. Fig. 4.12 shows the distributions of these likelihood

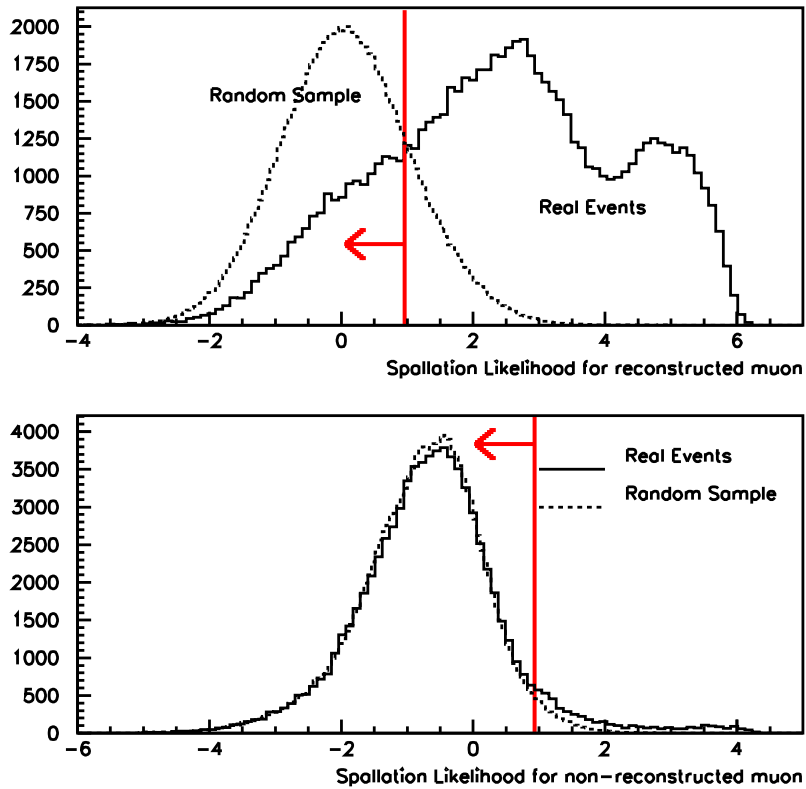


Figure 4.12: Distributions of the likelihood values for both the fitted (upper) and the unfitted (lower) muon tracks. The cut values of 0.98 and 0.92 are shown, respectively.

values for both the fitted and the unfitted muon tracks. Both plots also show a distribution of good events generated with a random vertex position in the detector. The cut value in both cases was chosen to minimize the removal of good events and maximize the removal of background. Values 0.98 and 0.92 are used in the case of a fitted and unfitted muon track, respectively. The randomly generated events are used to calculate the signal loss due to the spallation cut. The dead time that the cut effectively introduces is measured to be 21.1%.

4.2.4 Second Reduction

Due to the lowering of the energy threshold in May 1997 to 5.0 MeV for solar neutrino analysis, the background levels in the data have greatly increased. The second reduction is, therefore, designed to reduce the background at these lower energies.

- **New goodness cut.** The new vertex reconstruction algorithm and the goodfrac variable are described in Sec. 4.1.5. In the new goodness cut, events with $\text{goodfrac} > 0.2$ are removed. This cut is more than 90% efficient, while it removes $\sim 50\%$ of the background below 7 MeV.
- **Clusfit cut.** The clusfit vertex reconstruction algorithm is also described in Sec. 4.1.5. Events with the reconstructed clusfit vertex outside of the fiducial volume (200 cm of the ID wall) are removed. The clusfit cut is 90% efficient, while reducing the background below 7 MeV by 15~20%.
- **GRINGO cut.** The GRINGO cut was developed in 1998 in order to remove unknown noise events which have typically lower goodness of fit values. The GRINGO variable is defined in Fig. 4.13: define a plane perpendicular to the reconstructed direction of event; select grid points around the reconstructed vertex position as defined by Fig. 4.13 (maximum distance from vertex is 16 m); calculate goodness of fit for each grid point; calculate the difference of the goodness (Δgof) between each grid point and the vertex; count the number of grid points with Δgof above a set threshold, relative to the total number of grid points. This ratio is the GRINGO variable. Events with $\text{GRINGO} > 0.08$ are removed.

This threshold value is obtained from MC simulated solar neutrino events and by looking at the real data. In general, good events have small Δgof for close grid points and large Δgof for distant grid points, and thus have lower GRINGO values. The efficiency of the GRINGO cut is measured from the MC simulation

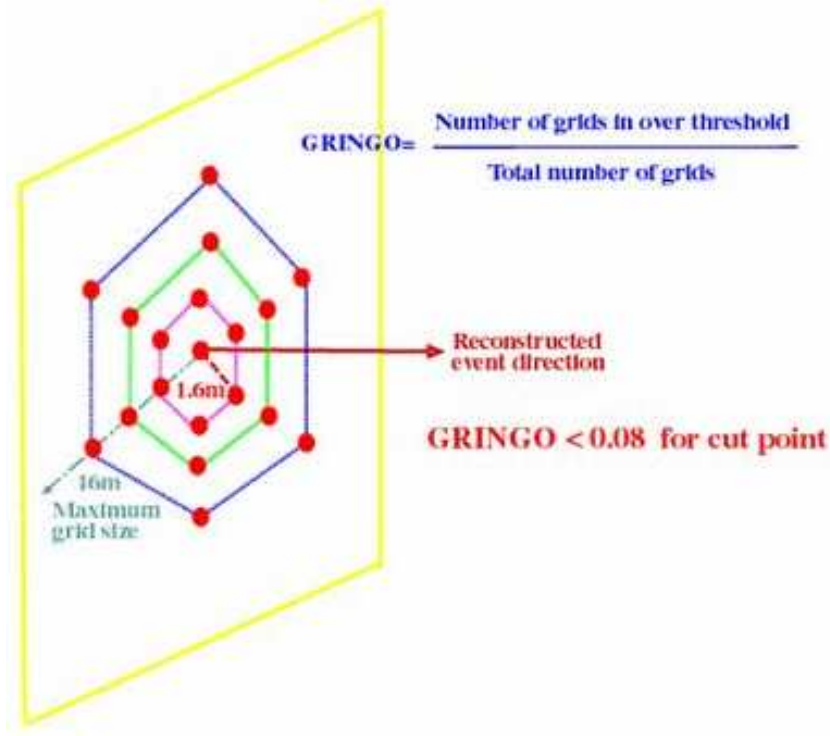


Figure 4.13: An illustration of the definition of the GRINGO variable.

to be $\sim 80\%$ at 5 MeV and close to 100% for higher energy events. The cut removes between 25% (at 5 MeV) and 90% (at 10 MeV) of the background.

- Cherenkov ring cut.** The Cherenkov ring image of an event can be smeared by the presence of γ -rays in the event. In order to estimate the validity of the reconstructed Cherenkov ring, the MC data sample (see Sec. 4.3) was used to construct a likelihood function from the angle between the reconstructed direction and the direction from the reconstructed vertex to each hit PMT. The product of all the likelihood values for all the hit PMTs is the Cherenkov ring likelihood of the event. The typical likelihood distribution from the real data is shown in Fig. 4.14. The points represent events correlated with the direction of the sun ($\cos\theta_{sun} \geq 0.8$, see Sec. 4.3.2 for the definition of $\cos\theta_{sun}$), and the histogram represents the events not correlated with the direction of the sun ($\cos\theta_{sun} < 0.8$). Events with Cherenkov ring likelihood less than -1.85

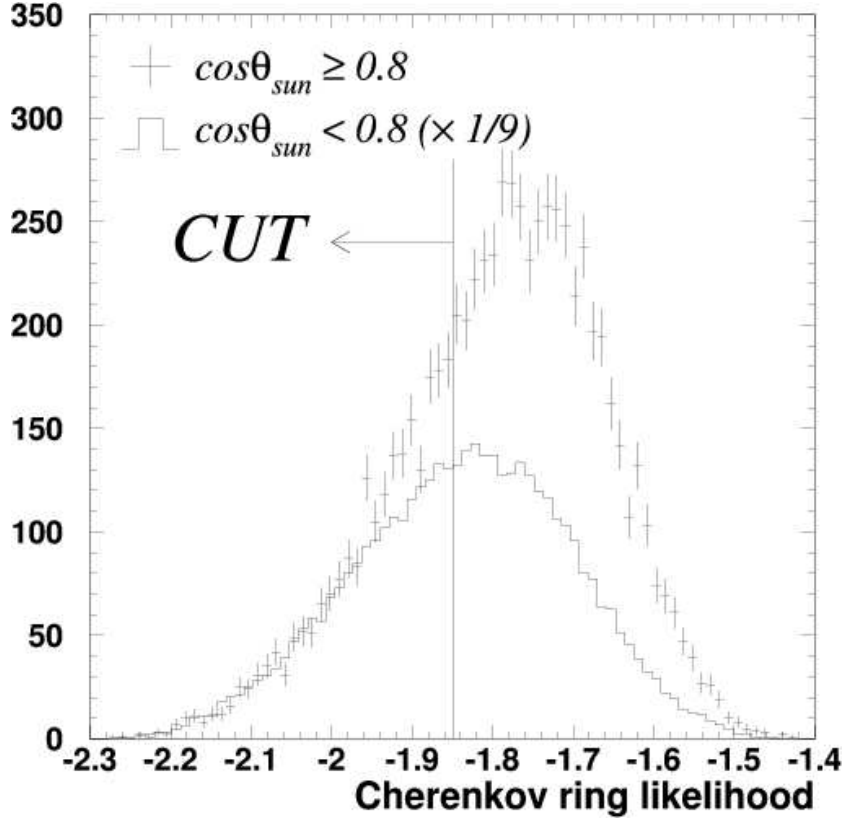


Figure 4.14: A typical Cherenkov ring likelihood distribution for sun-correlated (point) and sun-uncorrelated (histogram) events, showing the cut value of -1.85.

are removed.

- Gamma cut.** The gamma cut is a cut based on the position of the vertex and designed to remove events likely originating from the wall of the ID. The reconstructed direction of the events is traced backward from the vertex position and the distance to the wall, d_{wall} , is calculated. SLE triggered events ($E < 6.5$ MeV) with d_{wall} less than 800 cm and LE events ($E \geq 6.5$ MeV) with d_{wall} less than 450 cm are removed. This cut significantly reduces the number of background events near the ID walls, and “flattens” the directional distribution of the remaining events, making it uniform. Based on the MC simulation, the 450 cm cut is measured to be 92.2% efficient, while the 800 cm cut is 86% efficient.

4.2.5 Final Data Sample

This analysis presents results from the total SK-I period of the Super-Kamiokande experiment. For the solar neutrino analysis group, this period started with the official commencement of data acquisition on 31 May 1996, and ended on 15 July 2001, when the experiment was deliberately shut down for reparation and upgrade. The total SK-I detector livetime for the solar neutrino analysis is 1496.12 days.

The raw solar neutrino data sample for the complete SK-I time period contains 1.77×10^8 events. The data reduction process reduces this number to 2.96×10^5 events, which represents the final solar neutrino data sample. Although most of the background events are removed from the data sample by the data reduction process and the total number of events is reduced by a factor of 600, most of the remaining events still come from background sources. Fig. 4.15 shows a summary of the solar neutrino data reduction process. The energy distribution of the final data sample is considerably higher than a similar distribution from the MC simulation of the solar neutrino signal (including efficiencies). For this reason the solar neutrino signal cannot be extracted from the data on an event-by-event basis, but must be done statistically. This extraction process is described in Sec. 4.4.

In order to ensure that the data reduction process has indeed removed mostly background events and has not significantly reduced the signal beyond a mere efficiency effect, an analysis of ^{16}N events is performed with the same event reconstruction tools and the same data reduction steps. ^{16}N events occur at SK naturally, as a product of a capture of a stopping muon on an oxygen atom (one of the spallation products discussed in Sec. 4.2.3):



A fraction of the created ^{16}N is in the ground state, and beta decays with a half life of 7.13s. The rate and the energy range of these events are similar to those of the

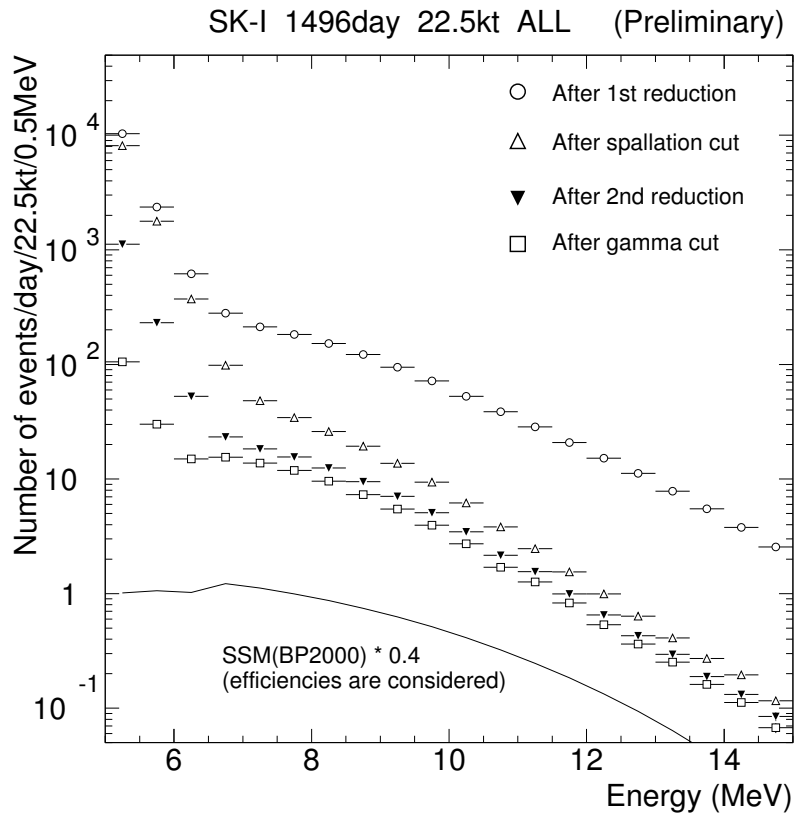


Figure 4.15: A summary of the solar neutrino data reduction.

solar neutrino events.

The expected rate of ^{16}N events is calculated in the innermost 11.5 kton fiducial volume (500 cm from the ID walls), using the measured stopping muon rate from the “muboy” muon track fitter (see Sec. 4.1.4). The measured stopping muon rate of 2530 ± 60 events/day, the muon decay lifetime in vacuum of $2.19703 \pm 0.00004 \mu\text{s}$ [22], the muon capture rate on ^{16}O of $9.747 \pm 0.006 \mu\text{s}$ [23], and the μ^- fractional occurrence (relative to $\mu^+ + \mu^-$) of 0.44 ± 0.01 [24] were used in the calculation. Further descriptions of the prediction calculation is presented in Ref. [16]. The expected rate is calculated to be 11.9 ± 1.0 events/day.

The measured ^{16}N event rate is obtained from the real data by searching for stopping muons (muon events which are not followed by a decay electron within $100 \mu\text{s}$), and selecting events within a sphere of a 335 cm radius centered at the stopping muon position and a time window of 0.1 s to 30 s following the stopping muon. A background rate is measured similarly by counting events offset in time from the stopping muon by 100 s. Both the signal and the background events are submitted to the same data reduction algorithm, excluding the spallation cut, and finally the resulting background rate is subtracted from the total resulting signal rate. Thus obtained ^{16}N event rate is measured to be 11.4 ± 0.2 events/day.

Because the measured ^{16}N rate agrees very well with the predicted rate, we conclude that SK’s data reduction removes mostly background events and does not significantly reduce the solar neutrino event rate. The data sample, therefore, represents the entire solar neutrino signal, including background, and cannot account for the measurement of a solar neutrino flux deficit by a simple “loss of signal” hypothesis.

4.3 Simulation of Solar Neutrino Events

It was mentioned earlier that SK cannot measure the solar neutrino flux directly, but detects recoil electrons from the neutrino-electron ES scattering:

$$\nu + e^- \longrightarrow \nu + e^- . \quad (4.12)$$

Furthermore, because most of the events in the final recoil electron data sample come from background sources, the extraction of the solar neutrino signal cannot be done on single electron events, but must be done statistically. For this purpose a Monte Carlo simulated data sample of pure solar neutrino recoil electron events is generated. A comparison of the shapes of the directional distributions of the simulated events to the ones of the final data sample is used as the method for obtaining the measured solar neutrino flux at SK.

A Monte Carlo simulation is performed of solar neutrinos, their ES interactions in the detector, and the detector's response to the resulting recoil electrons. The simulation uses laboratory-measured ^8B neutrino energy spectrum [25] and the neutrino-electron elastic scattering cross section [26], as well as the BP2000 [4] predictions of solar neutrino fluxes; it utilizes the GEANT detector simulator with finely calibrated detector parameters discussed above. The simulation assumes no neutrino oscillations. The result of the simulation is a background-free directional distribution of recoil electron event directions with a peak in the direction of the sun.

4.3.1 Neutrino Interaction Simulation

To correctly simulate the events at SK originating from solar neutrino ES interactions with electrons, the correct interaction cross section as well as the proper neutrino flux normalization must be obtained.

The differential neutrino-electron ES cross section, $\frac{d\sigma(E_\nu)}{dT}$, was obtained from Ref. [26] and it includes QED effects and radiative corrections. There are differences

in the form of the cross section between (ν_e, e) and (ν_μ, e) interactions. The (ν_e, e) cross section has a contribution from both the charged current and the neutral current interactions, while the (ν_μ, e) cross section has, naturally, only a contribution from the neutral current interactions. Because the simulation assumes no neutrino oscillations, and the sun produces only ν_e , only the (ν_e, e) cross section is used here.

As the ES interaction is a simple 2-body process, the kinematics of the scenario dictate that the energy of the recoil electron can have any value between zero and some T_{max} , which is given by:

$$T_{max} = \frac{2E_\nu^2}{2E_\nu + m}. \quad (4.13)$$

This relation comes from the conservation of energy and momentum principle. Having this, the total cross section can be calculated as a function of neutrino energy, E_ν , by numerically integrating the differential cross section from zero to T_{max} :

$$\sigma_{tot}(E_\nu) = \int_0^{T_{max}} \frac{d\sigma(E_\nu)}{dT} dT. \quad (4.14)$$

Fig. 4.16 shows the total (ν_e, e) and (ν_μ, e) cross section as a function of neutrino energy. These cross sections are a result of the weak interaction and are on the order of $\sim 10^{-44, -43} \text{ cm}^2$. The (ν_μ, e) total cross section is approximately an order of magnitude smaller than the (ν_e, e) total cross section.

In creating simulated recoil electrons in the detector, only ${}^8\text{B}$ neutrinos were initially considered, because only ${}^8\text{B}$ and hep neutrinos can produce events in SK's energy sensitivity range, and the predicted hep neutrino flux is an order 400 lower than the ${}^8\text{B}$ flux. The contribution from the hep neutrinos is, therefore, insignificant, and is included (and will be described below) only for completeness. The BP2000 ${}^8\text{B}$ neutrino flux of $5.05 \times 10^6 \text{ cm}^{-2}\text{s}^{-1}$ [4] was used in the simulation. Also, the terrestrially measured ${}^8\text{B}$ beta decay neutrino energy spectrum, $\lambda(E_\nu)$, from Ortiz et al. [25] is used. This spectrum is shown in Fig. 4.17 (top panel). The bottom panel of the figure shows the ratio of this spectrum to the previously published such

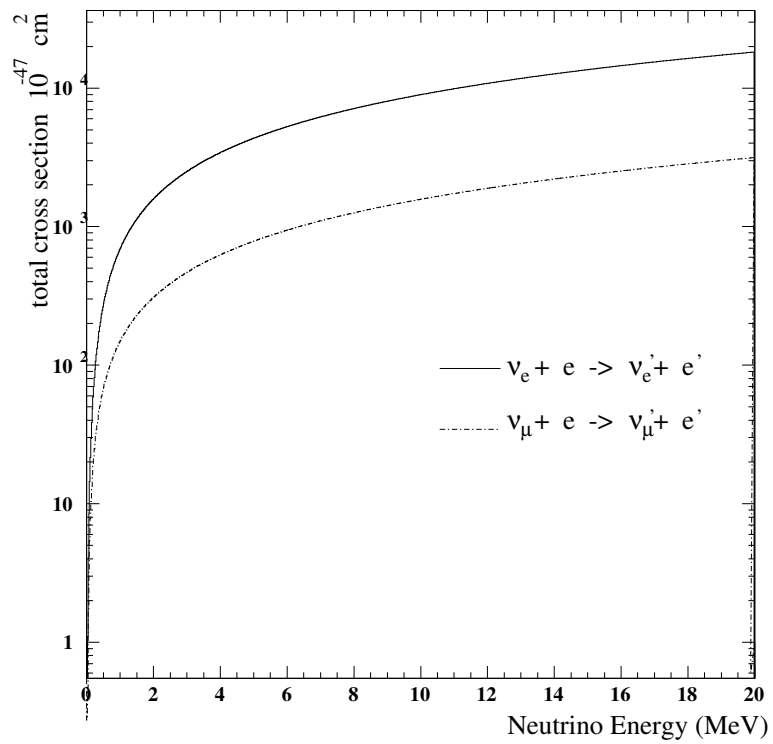


Figure 4.16: The total neutrino-electron ES cross section as a function of neutrino energy. The (ν_μ, e) total cross section is approximately an order of magnitude smaller than the (ν_e, e) total cross section.

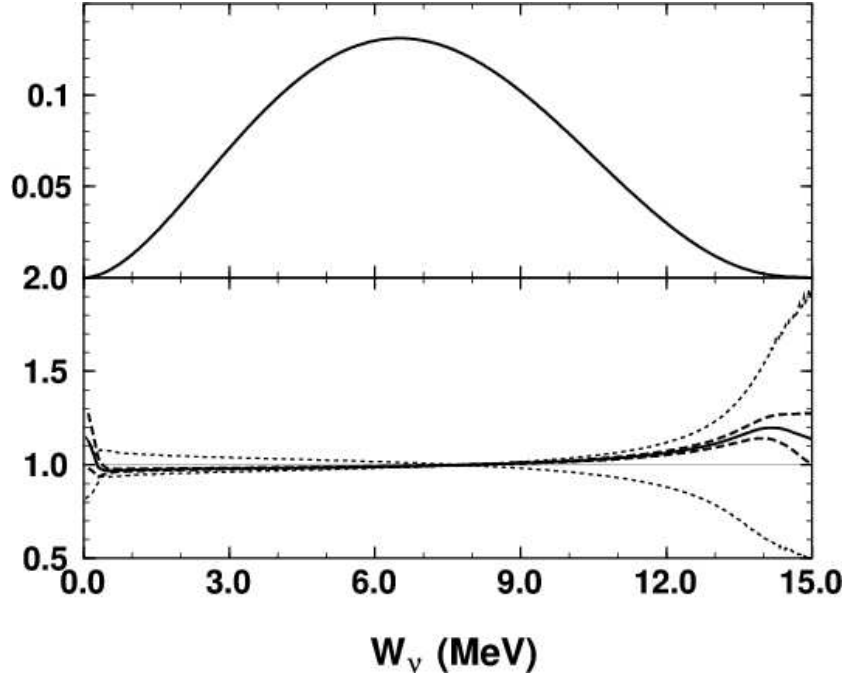


Figure 4.17: (top) The ^8B decay neutrino energy spectrum. (bottom) Ratio of this spectrum to the previously published such spectrum (see text). The dashed line represents the uncertainty in this spectrum while the dotted line is the 3σ error of the old spectrum.

spectrum by Bahcall et al. [27]. It also shows the uncertainties of the new spectrum (dashed line) and the 3σ errors of the old spectrum (dotted line). The difference in the two spectra is not very pronounced, except for the highest energies (>13 MeV).

The first step is to generate a distribution of neutrino energies according to the ^8B neutrino spectrum, $\lambda(E_\nu)$, and the total ES cross section, $\sigma_{tot}(E_\nu)$. The convolution of these two quantities, $\lambda(E_\nu) \cdot \sigma_{tot}(E_\nu)$, represents the probability that a ^8B neutrino will interact in the SK water by scattering an electron. Neutrino energies used in the simulation are then chosen from this distribution (Fig. 4.18) normalized to unity.

For each input neutrino energy, the kinetic energy of the recoil electron has to be chosen, according to the neutrino-electron ES differential cross section distribution, $\frac{d\sigma(E_\nu)}{dT}$. Fig. 4.19 shows this differential cross section for a 12 MeV neutrino.

Repeating 10 million times this process of choosing first a neutrino energy and

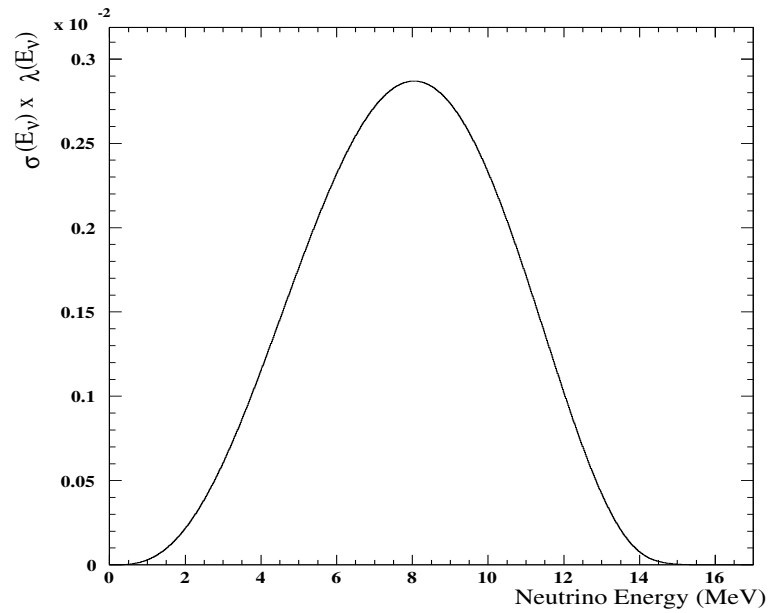


Figure 4.18: The $\lambda(E_\nu) \cdot \sigma_{tot}(E_\nu)$ distribution used for choosing the neutrino energy as the input to the simulation.

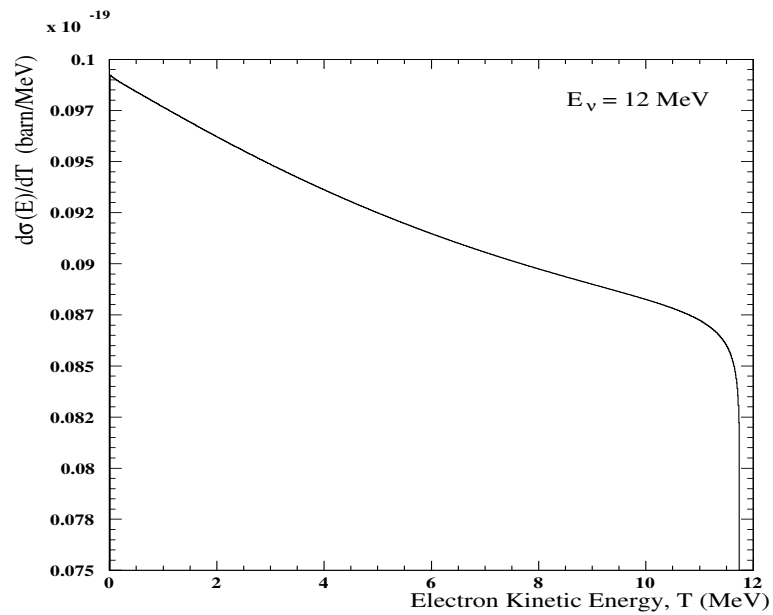


Figure 4.19: The $\frac{d\sigma(E_\nu)}{dT}$ distribution used for a 12 MeV neutrino used in choosing the electron's recoil kinetic energy. The plot is zero suppressed.

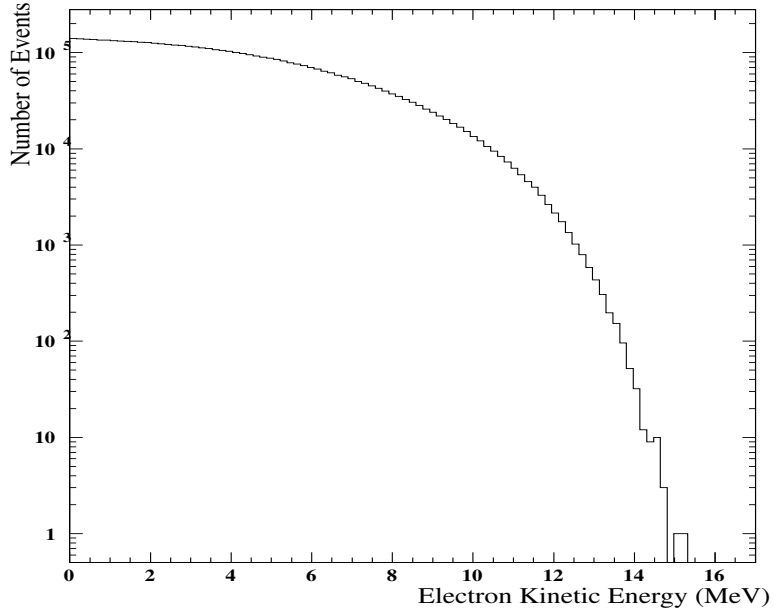


Figure 4.20: The distribution of ${}^8\text{B}$ neutrino scattered electrons as a function of the electron’s kinetic energy.

then a recoil electron energy yields a distribution of ${}^8\text{B}$ neutrino scattered electrons in the SK detector as a function of the electron’s kinetic energy (Fig. 4.20). Although the most likely neutrino scattered in the detector is ~ 8 MeV (from Fig. 4.18), the peculiar shape of the differential cross section (in Fig. 4.19) “washes” out this 8 MeV peak and creates a falling electron spectrum in Fig. 4.20.

The recoil electron distribution is normalized to the total expected recoil electron rate, N , from the BP2000 prediction of the ${}^8\text{B}$ neutrino flux ($\Phi^{b8} = 5.05 \times 10^6 \text{ cm}^{-2}\text{s}^{-1}$) and the number of electrons in the ID volume of the detector ($N_e = 1.081 \times 10^{34}$). This is accomplished by a numerical integration:

$$N = N_e \Phi^{b8} \int_0^\infty \lambda(E_\nu) \sigma(E_\nu) dE_\nu = 290.1 \text{ events/day} . \quad (4.15)$$

This is the total rate in the entire 32.4 kt ID volume for all neutrino energies ($0 \sim 15$ MeV). Thus normalized electron energy distribution in Fig. 4.20 (with a small hep contribution at the highest energies) is used as the input into the detector response simulation.

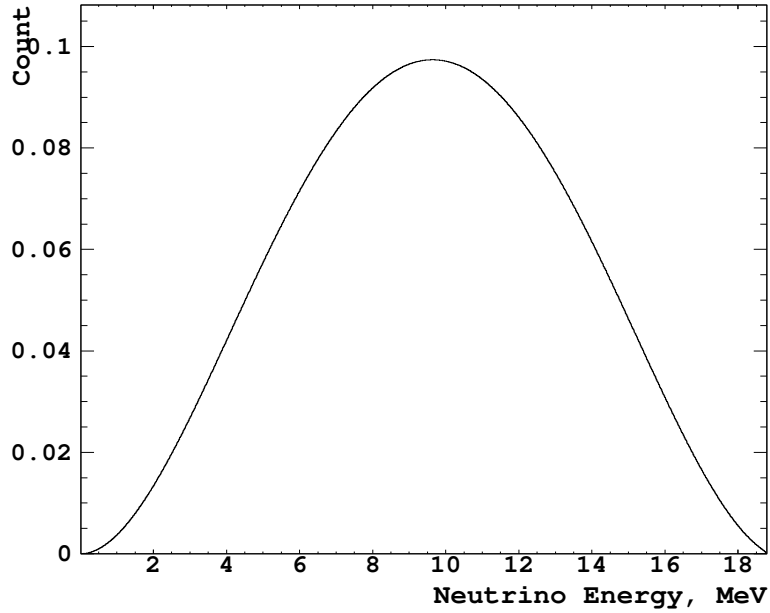


Figure 4.21: The hep neutrino energy spectrum. Note that the hep spectrum extends beyond 18 MeV, while the ^8B spectrum ends at 15 MeV.

The contribution from hep neutrinos to this electron distribution is calculated for completeness in a similar way. The hep neutrino flux of $\Phi^{hep} = 9.3 \times 10^3 \text{ cm}^{-2}\text{s}^{-1}$ [4] and the hep neutrino energy spectrum in Fig.4.21 [4] were used. The total recoil electron rate stemming from hep neutrino scattering is calculated to be 0.75 events/day, or a factor of ~ 400 smaller than the similar rate from ^8B neutrinos. Because the hep neutrino energy spectrum extends beyond 18 MeV, and the ^8B neutrino spectrum ends at 15 MeV, the recoil electron distribution will have a small contribution from hep neutrinos at the highest energies.

4.3.2 Detector Response Simulation

Once the kinetic energy of the recoil electron is chosen, the information of each simulated neutrino event is input into the SK detector MC simulation. The simulation program is designed to track the recoil electron as it travels and interacts in the detector water, to generate and track Cherenkov photons from the electron, and fi-

nally, to simulate the response of the PMTs and the electronics to these events. It is based on GEANT 3.21, a particle interaction simulation from CERN [28]. This GEANT package is capable of simulating electro-magnetic interactions at energies between 10 keV and 10 TeV. It models multiple Coulomb scattering of electrons, generation of Cherenkov light, δ -ray generation, and Bremsstrahlung photon creation, as well as propagation, scattering, and absorption of the created Cherenkov photons. For higher energy photons, the simulation includes Compton scattering and pair production.

To ensure that the simulator is properly modeling the detector and all its parts, the parameters used in the calculation (like reflectivity of PMT glass and black sheet) are tuned to their observed or theoretically predicted values, and the response of the PMTs and the DAQ electronics are tuned to reproduce the measured calibration signals from the detector.

The PMT timing resolution for single photoelectrons and the PMT collection efficiency are tuned using the LINAC calibration data. The simulated PMT timing resolution is adjusted until the vertex resolution of the MC simulation reproduces the value from the LINAC calibration. Similarly, the PMT collection efficiency is adjusted until the simulated energy scale matches the one from the LINAC data. These simulated values are in good agreement with the previous, laboratory measured ones [29]: the 78% PMT collection efficiency agrees well with the measured value of 70%.

The overall light attenuation in the water (stemming from scattering and absorption of light) is measured directly as described in Sec. 3.3.2, but the scattering to absorption ratio for Cherenkov photons is tuned to the results of the calibration. Rayleigh scattering is a dominant effect on photons with wavelengths below ~ 400 nm, while above ~ 430 nm, absorption begins to dominate the light attenuation. The ratio of these two effects is adjusted in the simulation so that the positional dependence

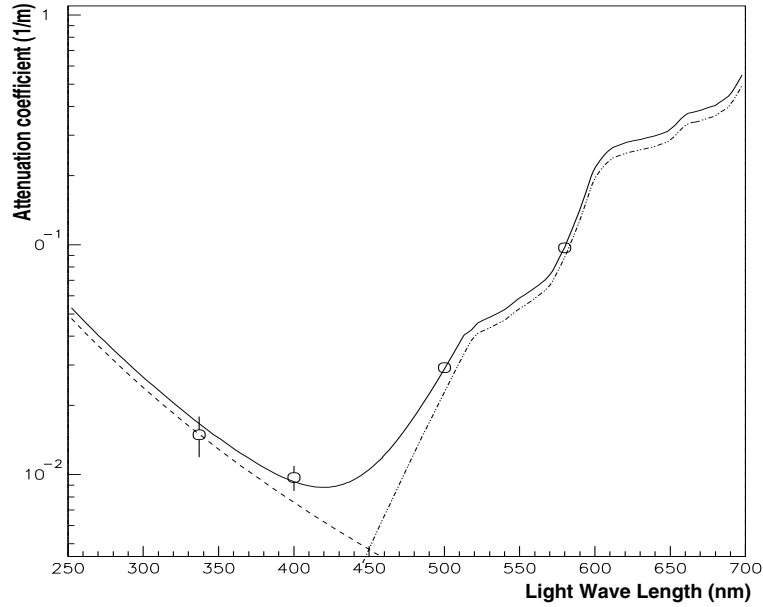


Figure 4.22: The tuned light attenuation coefficient (inverse attenuation length) as a function of wavelength. The scattering (dashed line) and the absorption (dot-dashed line) components are shown. The modeled attenuation length agrees well with the measured values (circles).

of the MC simulated events agrees with that of the LINAC events. The light attenuation of MC events is shown in Fig. 4.22. The tuned attenuation length agrees well with the measured values.

Input into the Detector Simulation

The event information that is input into the detector simulation includes the electron kinetic energy, its time, direction, and vertex position. The times of electron events are simulated so as to match the entire livetime of the real SK data, because the position of the sun is used in determining the direction of the electron. For each simulated minute of livetime, the known position of the sun in the sky is used to calculate the local direction of the parent solar neutrino. From the nature of the ES interaction, the direction of the electron is generated from the chosen neutrino energy

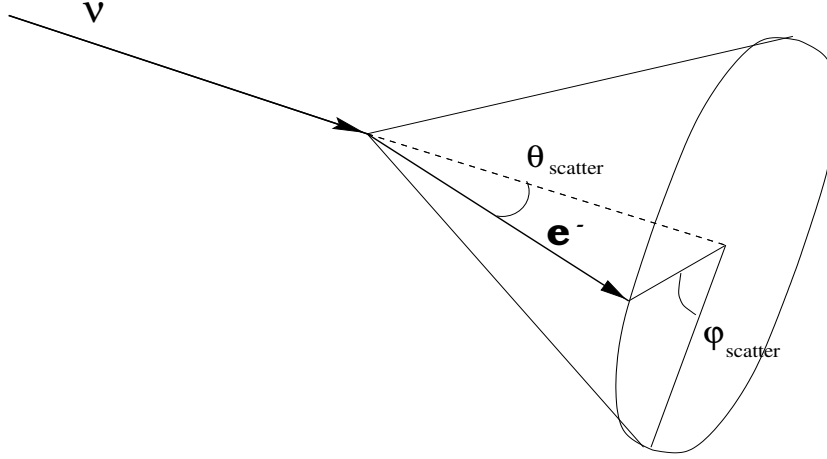


Figure 4.23: An illustration of the neutrino-electron ES interaction and the definitions of the event direction variables.

(E_ν) and the kinetic energy of the electron (T), by a simple kinematic relation:

$$\cos\theta = \frac{1 + \frac{m}{E_\nu}}{\sqrt{1 + \frac{2m}{T}}}. \quad (4.16)$$

This relation is illustrated in Fig. 4.23, where the angle, θ , is defined as the angle between the direction of the neutrino and the direction of the recoil electron. The angle, ϕ , is chosen at random. The vertex position is also chosen as a random location in the entire 32.4 kt ID volume. The whole ID is used for input vertex locations instead of the fiducial volume (22.5 kt), to account for the possible asymmetries due to misreconstruction of vertex positions near the edge of the fiducial volume.

In addition, the number of the dead PMTs and the relative water transparency at any given time were both input for each event, in order to ensure that the simulation models the real data as closely as possible. To prevent the statistical uncertainties from limiting the accuracy of the results, 50 times the number of expected real data events were generated in the simulation (i.e. 10^7 total MC events).

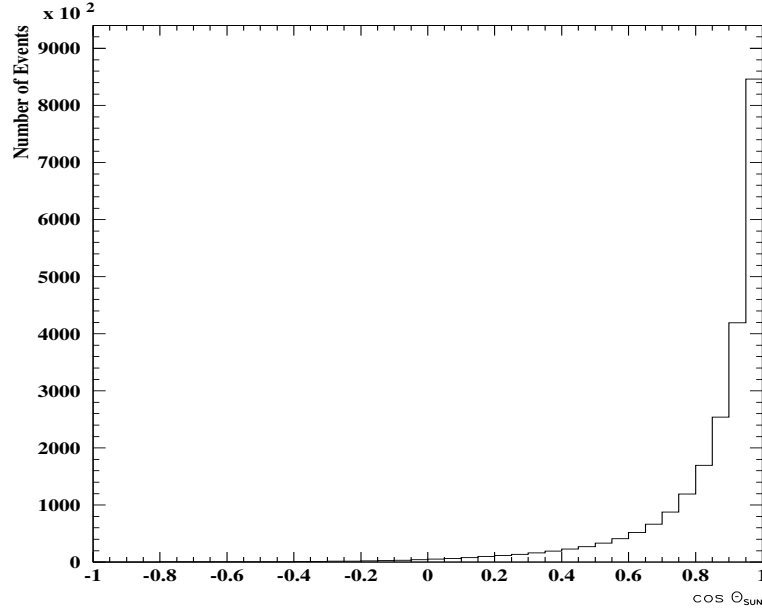


Figure 4.24: The directional distribution of the MC simulated solar neutrino events, used in the extraction of the real solar neutrino signal at SK. Note that $\cos\theta_{sun}$ of 1.0 corresponds to the direction of the sun.

Output of the Detector Simulation

The detector simulation outputs MC events in the same format as the real data. These events are subjected to the same reconstruction algorithms and reduction steps, and finally, to a trigger simulation routine. The trigger simulation routine reproduces the SK hardware LE and SLE triggers by generating HITSUM pulses for each hit PMT in the simulated events, similarly to the description in Sec. 3.2.5. If the sum of these simulated HITSUM exceeds the threshold of either the LE or the SLE trigger (different SLE thresholds for different time periods of the simulated events), that trigger bit is assigned to the event. Only events that passed the trigger and the reduction simulation, were included in the MC event sample.

The main result from the MC simulation is the directional distribution of the simulated events, with a peak in the direction of the sun. This distribution as a function of the cosine of the difference between the event direction and the direction

of the sun ($\cos\theta_{sun}$) is shown in Fig. 4.24, for all event energies (5.0 – 20.0 MeV). The strong peak at $\cos\theta_{sun} = 1.0$ shows a clear correlation in the two directions. The actual expected MC event rate is obtained by normalizing this distribution by the expected ^8B neutrino flux discussed above.

4.4 Signal Extraction Method

Because of this correlation between the direction of the recoil electron and the direction of the solar neutrino, the directional distribution from Fig. 4.24 is used in selecting solar neutrino events from the data sample. To do this, a similar angular distribution is made of the final sample events, which include background, and is fitted to the one from the MC prediction, using a maximum log likelihood method. The solar neutrino signal is chosen as the distribution of the events that best fits the MC prediction distribution. This fitting method is used to obtain the total SK event rate (translated into the $^8\text{B}+\text{hep}$ neutrino flux), the event energy spectrum, the asymmetry in the day vs. night flux (stemming from the idea that some of the ν_e that have oscillated into $\nu_{\mu,\tau}$ can oscillate back into ν_e in the earth’s core), and the distribution in the zenith angle (unbinned day/night asymmetry). In fitting the solar direction distributions, corrections are made for non-flat background, angular cut efficiency, and the eccentricity of earth’s orbit.

4.4.1 Likelihood Fitting

In order to extract from the final data sample the solar neutrino flux relative to the SSM prediction, a maximum log likelihood method (dubbed “solfit”) is used. The general form of the probability function for the likelihood consists of signal and background components:

$$P(E_e, \cos\theta_{sun}, x) = P_{sig}(E_e, \cos\theta_{sun}) \cdot x + P_{bg}(E_e, \cos\theta_{sun}) \cdot (1 - x), \quad (4.17)$$

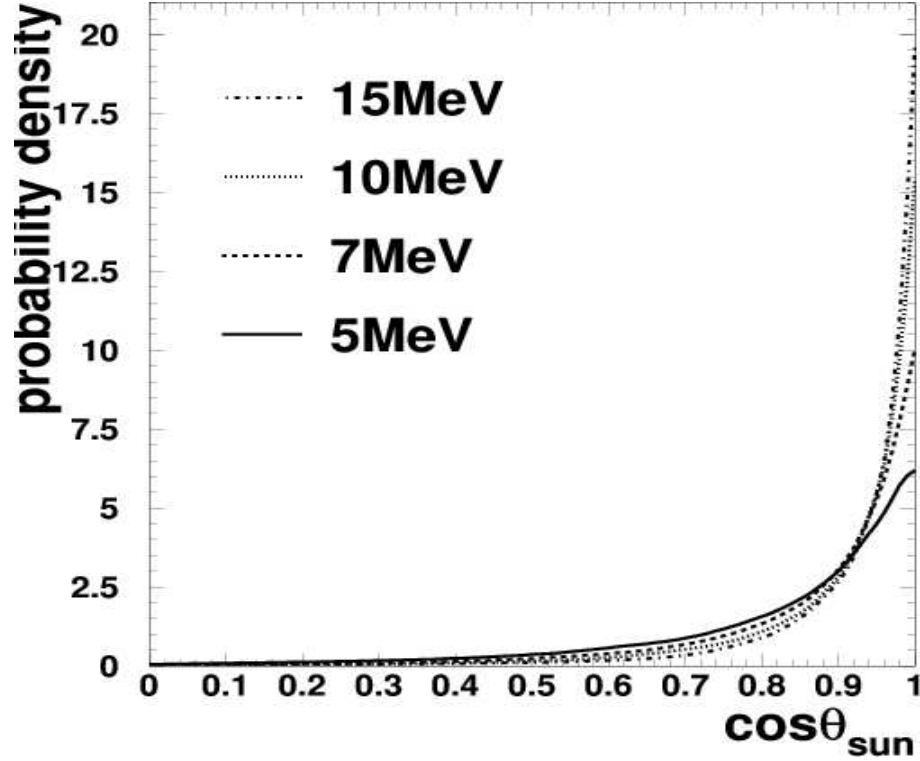


Figure 4.25: The probability density function for solar neutrino signal events, P_{sig} , at various energies.

where E_e is the recoiled electron energy, and x is the fraction of the fraction of the solar neutrino signal events relative to the observed total number of events. The probability density of the signal (P_{sig}) is obtained by a MC simulated directional distribution, similar to the one in Fig. 4.24, at various energies. Fig. 4.25 shows P_{sig} as a function of $\cos\theta_{sun}$ for electron energies of 5, 7, 10, and 15 MeV. Note the strong peak in the direction of the sun ($\cos\theta_{sun} = 1.0$).

The shape of the directional distribution of the background events (P_{bg}) is generally flat, but the asymmetries in the γ -ray background from the rock and PMT gain variations slightly distort this flatness. These small deviations from a flat background are taken into account by fitting an 8th order polynomial to a MC simulated zenith angle ($\cos\theta_z$) distribution, and transforming the fitted polynomial into a function of $\cos\theta_{sun}$. A background shape independent of the zenith angle is assumed. Fig. 4.26

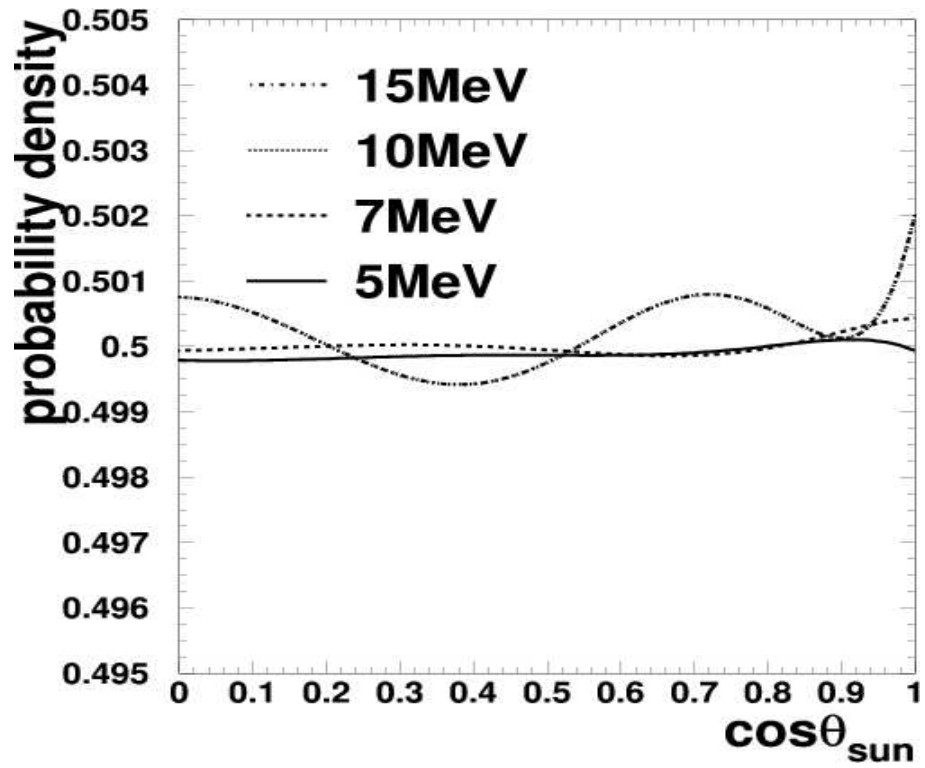


Figure 4.26: The probability density function for solar neutrino background, P_{bg} , at various energies. Note that the y-axis is zero-suppressed, and the non-linearities are only on the order of 0.2%.

shows the slight angular variations in P_{bg} as a function of $\cos\theta_{sun}$ for electron energies of 5, 7, 10, and 15 MeV. Note the extremely small scale of the y -axis.

The signal fraction, x , also differs between different electron energies. In order to accommodate this energy dependence of the signal fraction, the probability density is redefined in the following way:

$$P(E_e, \cos\theta_{sun}, x) = P_{sig}(E_e, \cos\theta_{sun}) \cdot x_i(x) + P_{bg}(E_e, \cos\theta_{sun}) \cdot (1 - x_i(x)), \quad (4.18)$$

where

$$x_i(x) = \frac{N_i^{ssm}}{N_{all}^{ssm}} \cdot \frac{N_{all}^{data}}{N_i^{data}} \cdot x, \quad (4.19)$$

and i is the index of the electron energy bin, N_i is the number of events in the i^{th} energy bin, and N_{all} is the total number of events.

From the probability density thus defined, the likelihood function is constructed:

$$\mathcal{L}(x) = \prod_{i=1}^{N_{ene}} \prod_{j=1}^{N_i} P_{ij}(E_e, \cos\theta_{sun}, x_i(x)), \quad (4.20)$$

where N_{ene} is the number of energy bins, and N_i is the number of events in the i^{th} energy bin. This likelihood function as a function of x is presented in Fig. 4.27. The number of signal events is obtained from x_{max} , the signal fraction that gives maximum likelihood:

$$N_{sig} = x_{max} \cdot N^{data}. \quad (4.21)$$

The statistical error on N_{sig} is the difference between x_{max} and x which gives 22% of maximum likelihood value: $\mathcal{L}(x_{err}) = e^{-1/2} \cdot \mathcal{L}(x_{max})$. The systematic uncertainties are explained in Sec. 4.4.3.

4.4.2 Summary of SK Signal Measurements

Using the likelihood method described above, the neutrino total flux, the day/night flux asymmetry, and the recoil electron energy spectrum, as well as an unbinned zenith angle distribution of the neutrino flux were all extracted from the SK-I final data sample (Sec. 4.2.5) and used in the present neutrino oscillation analysis.

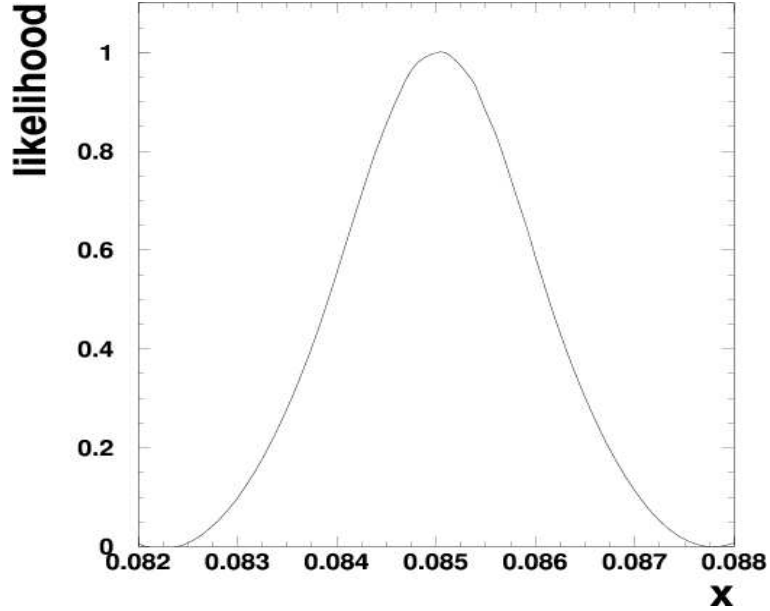


Figure 4.27: The likelihood distribution of the signal fraction, x . The value of x with the maximum likelihood is used in the extraction of the signal.

Solar Neutrino Total Flux

Fig. 4.28 shows the $\cos\theta_{sun}$ distribution of all data events from 5.0 to 20.0 MeV, as extracted by the signal extraction method. This distribution includes the solar neutrino signal as well as the background. The strong peak in the direction of the sun ($\cos\theta_{sun} = 1.0$) is used to separate the signal events from the background.

The observed total number of recoil electron events in the final data sample in the energy range 5.0 – 20.0 MeV is:

$$N_{sig} = 22387 \pm 226(\text{sta.})_{-709}^{+782}(\text{sys.}). \quad (4.22)$$

The expected number of signal event, according to the SSM prediction is:

$$N_{exp} = \sum_{i=1}^{N_{thr}} \frac{N_{red,i}}{N_{MC,i}} T_{live,i} N_{ssm} = 48173, \quad (4.23)$$

where N_{thr} is the number of trigger thresholds, i is the run period with a different SLE trigger threshold, $N_{MC,i}$ and $N_{red,i}$ are the number of MC simulated solar neutrino events in the i^{th} run period, before and after data reduction, respectively, $T_{live,i}$ is the

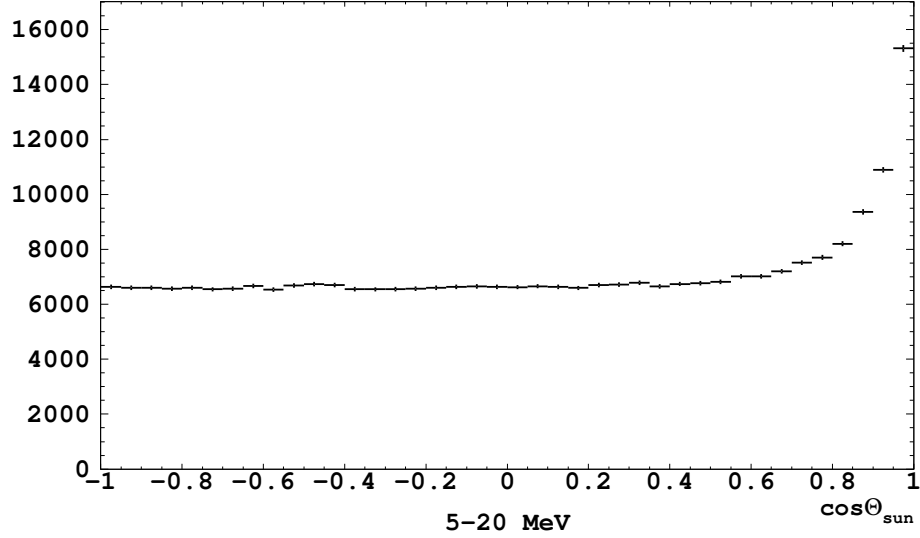


Figure 4.28: The $\cos\theta_{sun}$ distribution of events in the energy range 5.0 – 20.0 MeV, extracted for calculation of the total neutrino flux. Note the strong peak in the solar direction.

live time of the i^{th} run period, and N_{ssm} is the SSM prediction of the total number of solar neutrino recoil electrons in SK, 290.1 events/day (Eq. 4.15).

Comparing these two results, it is clear that SK, similarly to all previous experiments, measures a deficit in the solar neutrino flux:

$$\frac{DATA}{SSM} = 0.465 \pm 0.005(\text{sta.})_{-0.015}^{+0.016}(\text{sys.}). \quad (4.24)$$

Using the SSM prediction of the ^8B neutrino flux of $5.05 \times 10^6 \text{cm}^{-2}\text{s}^{-1}$, the measured ^8B neutrino flux becomes:

$$\Phi_\nu = 2.34 \pm 0.02(\text{sta.})_{-0.07}^{+0.08}(\text{sys.}) \times 10^6 \text{cm}^{-2}\text{s}^{-1}. \quad (4.25)$$

The hep neutrino flux is about a factor of 600 lower, and thus does not significantly contribute to the total measured solar neutrino flux.

Day/Night Flux Asymmetry

The day flux and the night flux of solar neutrinos are also measured separately at SK, because a possible regeneration of the solar ν_e in the earth's core would affect

the neutrino flux during night time, i.e. when the sun is on the opposite side of the earth (see Sec. 2.3.2). The day flux is defined as the flux of solar neutrinos coming toward the detector from above the local horizon; the night flux consists of neutrinos from below the local horizon.

Adopting the same method as for the total neutrino flux, the day (Φ_d) and night (Φ_n) neutrino fluxes are measured to be:

$$\begin{aligned}\Phi_d &= 2.28 \pm 0.03(\text{sta.})_{-0.07}^{+0.08}(\text{sys.}) \times 10^6 \text{ cm}^{-2}\text{s}^{-1} \\ \Phi_n &= 2.32 \pm 0.03(\text{sta.})_{-0.07}^{+0.08}(\text{sys.}) \times 10^6 \text{ cm}^{-2}\text{s}^{-1},\end{aligned}\quad (4.26)$$

or comparing them to the SSM prediction:

$$\begin{aligned}\frac{DATA}{SSM}(\text{day}) &= 0.451 \pm 0.007(\text{sta.})_{-0.014}^{+0.016}(\text{sys.}) \\ \frac{DATA}{SSM}(\text{night}) &= 0.460 \pm 0.006(\text{sta.})_{-0.015}^{+0.016}(\text{sys.}).\end{aligned}\quad (4.27)$$

This difference in the day and night solar neutrino fluxes yields a day/night flux asymmetry of:

$$A_{dn} = \frac{\Phi_d - \Phi_n}{1/2(\Phi_d + \Phi_n)} = -0.019 \pm 0.025. \quad (4.28)$$

The asymmetry is not statistically significant to be a smoking-gun evidence for neutrino oscillations, but can be used in discrimination between various neutrino oscillation scenarios (Ch. 5).

Recoil Electron Energy Spectrum

The energy dependence of the solar neutrino flux is studied through the measurement of the recoil electron energy spectrum. This measurement is obtained in the same way as the total flux and the day and night fluxes. In each of the defined energy bins, the recoil electron rate was obtained by the above described likelihood fitting method. For this analysis, a 21-bin energy spectrum was used:

5.0 ~ 14.0 MeV	...	eighteen 0.5 MeV bins
14.0 - 15.0 MeV	...	one 1.0 MeV bin
15.0 - 16.0 MeV	...	one 1.0 MeV bin
16.0 - 20.0 MeV	...	one 1.0 MeV bin.

Fig. 4.29 and Fig. 4.30 show the $\cos\theta_{sun}$ distributions of all 21 energy bins. Even when divided into 21 bins, SK's solar neutrino data still exhibits a strong peak on the direction of the sun. A distribution of events in the energy range 20.0–30.0 MeV is also shown in Fig. 4.30 for comparison. Note the absence of a peak in the solar direction in this distribution.

The measured energy spectrum as compared to the prediction of the SSM is shown in Fig. 4.31. The numerical values of the DATA/SSM ratio of the spectrum is presented in Tab. 4.1. The DATA/SSM energy spectrum is shown in Fig. 4.32. In all cases only the statistical uncertainties are shown. Fig. 4.32 clearly shows the absence of any statistically significant distortions in the energy spectrum, and thus, any smoking-gun evidence for neutrino oscillations stemming from spectral distortions.

4.4.3 Systematic Uncertainties

The systematic uncertainties associated with the solar neutrino flux measurement at SK are classified in two categories: the energy correlated uncertainties (the uncertainties affect each energy bin differently, in a correlated way) and the energy uncorrelated uncertainties (the uncertainties affect all energy bins together in the same way).

Energy Correlated Uncertainties

The systematic uncertainties in the absolute energy scale and energy resolution affect the neutrino flux measurements in all energy bins in an interdependent and corre-

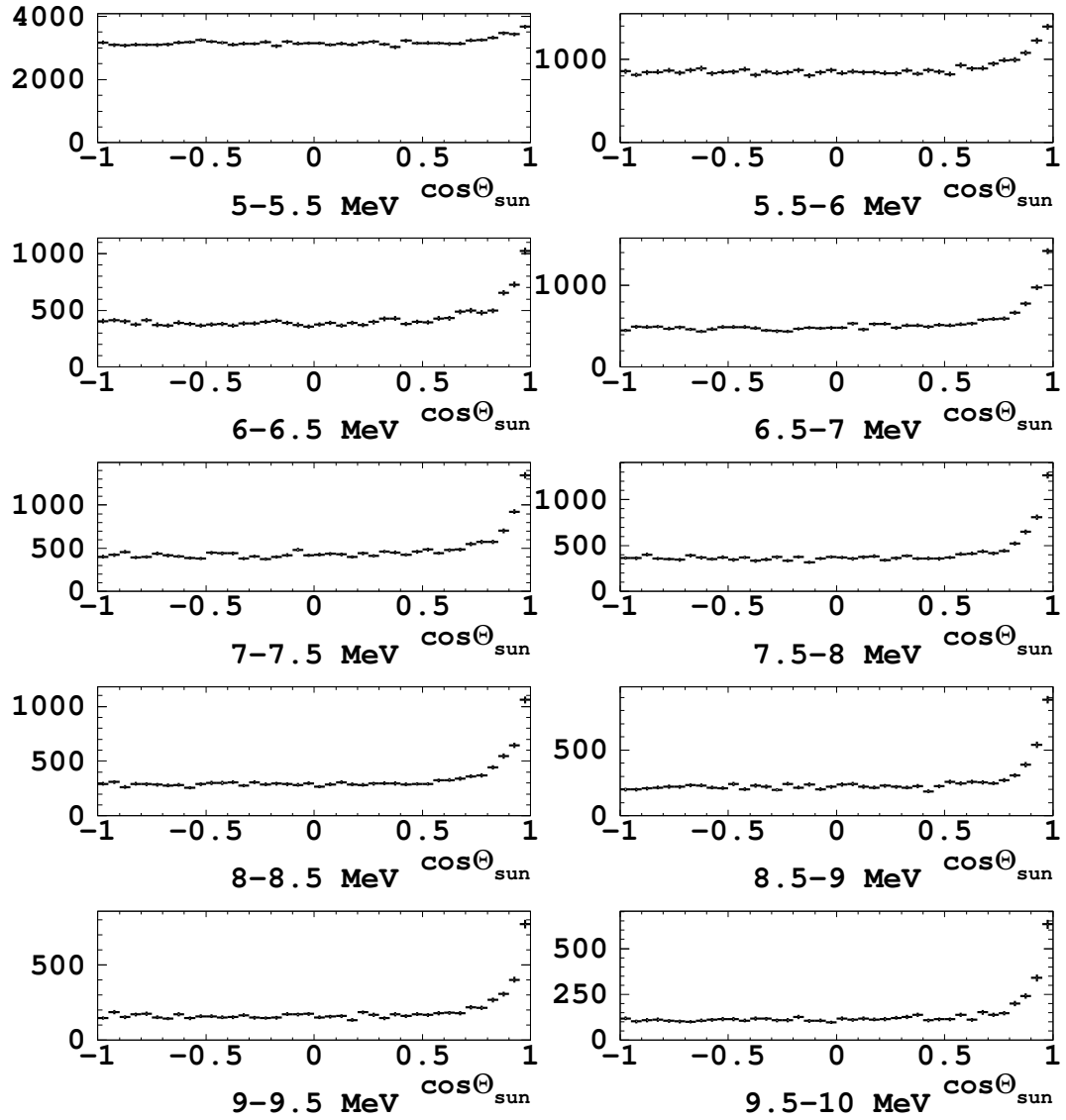


Figure 4.29: The $\cos\theta_{sun}$ distributions of events in the 10 energy bins between 5.0 and 10.0 MeV. Note the strong peak in the solar direction in all distributions.

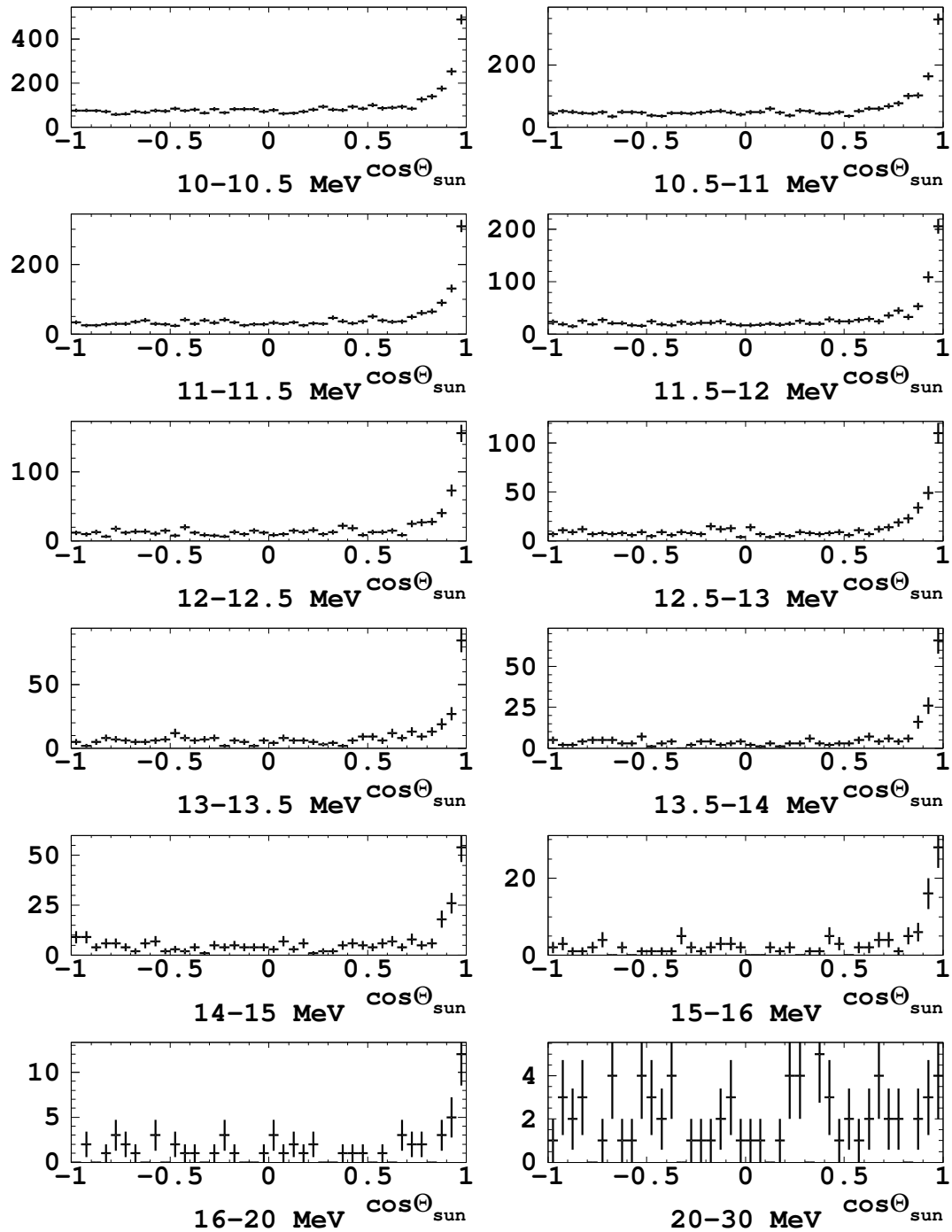


Figure 4.30: The $\cos\theta_{sun}$ distributions of events in the 11 energy bins between 10.0 and 20.0 MeV, as well as a bin of 20.0 – 30.0 MeV, which is shown for comparison. Note the absence of a peak in the solar direction in this distribution.

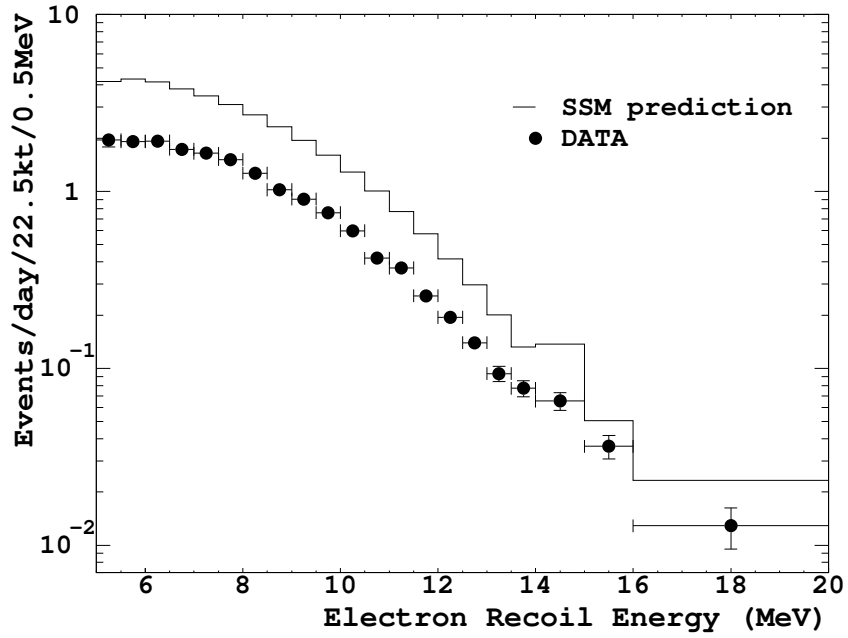


Figure 4.31: Recoil electron energy spectrum measured at SK and compared with the SSM prediction. The statistical uncertainties are also shown.

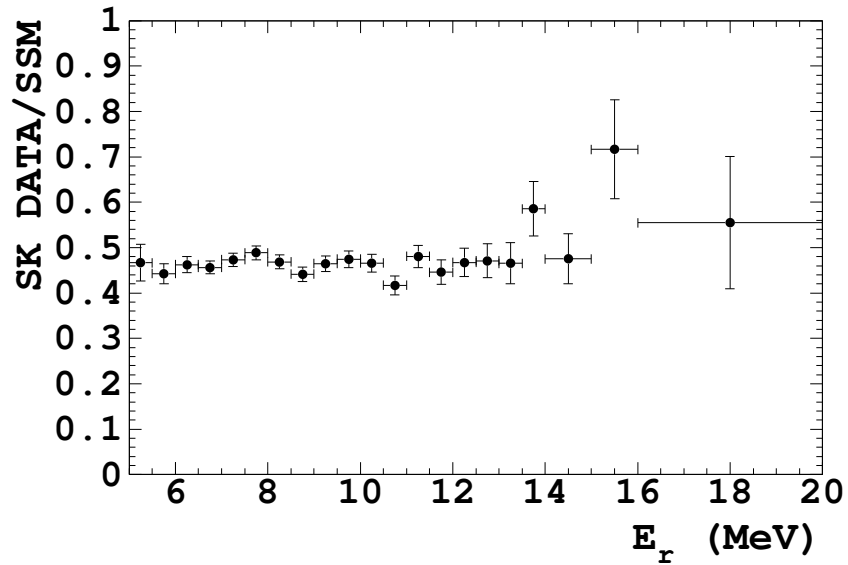


Figure 4.32: Recoil electron energy spectrum measured at SK and normalized by the SSM prediction. The statistical uncertainties are also shown.

Table 4.1: SK recoil electron energy spectrum.

Energy (MeV)	DATA (ev./day/22.5kt)	SSM (ev./day/22.5kt)	DATA/SSM (\pm stat.err.)
5.0 - 5.5	1.954 \pm 0.138	3.41	0.467 \pm 0.040
5.5 - 6.0	1.913 \pm 0.077	3.51	0.443 \pm 0.022
6.0 - 6.5	1.924 \pm 0.059	3.38	0.462 \pm 0.018
6.5 - 7.0	1.732 \pm 0.053	3.79	0.456 \pm 0.014
7.0 - 7.5	1.643 \pm 0.050	3.47	0.473 \pm 0.014
7.5 - 8.0	1.513 \pm 0.047	3.10	0.488 \pm 0.015
8.0 - 8.5	1.268 \pm 0.042	2.71	0.469 \pm 0.015
8.5 - 9.0	1.022 \pm 0.036	2.32	0.441 \pm 0.016
9.0 - 9.5	0.904 \pm 0.033	1.946	0.465 \pm 0.017
9.5 - 10.0	0.759 \pm 0.029	1.601	0.474 \pm 0.018
10.0 - 10.5	0.599 \pm 0.025	1.286	0.466 \pm 0.020
10.5 - 11.0	0.419 \pm 0.021	1.006	0.417 \pm 0.021
11.0 - 11.5	0.369 \pm 0.019	0.768	0.481 \pm 0.024
11.5 - 12.0	0.257 \pm 0.016	0.577	0.446 \pm 0.027
12.0 - 12.5	0.1943 \pm 0.0131	0.416	0.467 \pm 0.032
12.5 - 13.0	0.1395 \pm 0.0111	0.296	0.471 \pm 0.038
13.0 - 13.5	0.0934 \pm 0.0091	0.201	0.465 \pm 0.045
13.5 - 14.0	0.0772 \pm 0.0080	0.1318	0.585 \pm 0.060
14.0 - 15.0	0.0654 \pm 0.0076	0.1375	0.475 \pm 0.055
15.0 - 16.0	0.0363 \pm 0.0055	0.0506	0.717 \pm 0.109
16.0 - 20.0	0.0129 \pm 0.0034	0.0232	0.555 \pm 0.146

lated manner. This means the uncertainties have a direct effect on the shape of the observed energy spectrum.

The following are the main sources of energy correlated systematic uncertainties in the SK data:

- Uncertainty in position dep. of energy scale (by LINAC): $\pm 0.5\%$
- Uncertainty in position dep. of energy resolution (by LINAC): $\pm 2.0\%$
- Uncertainty in energy dep. of energy scale (by LINAC): $\pm 0.5\%$
- Uncertainty in energy dep. of energy resolution (by LINAC): $\pm 2.0\%$
- Uncertainty in directional dep. of energy scale (by spallation): $\pm 0.5\%$
- Uncertainty in water transparency measurement: $\pm 0.22\%$
- Uncertainty in LINAC system (for electron 8.9 MeV): $\pm 0.33\%$

The effect of all these uncertainties on the energy spectrum measurement is evaluated as follows. In order to simulate the observed energy spectrum, $\lambda(E_{obs})$ from the original spectrum, $\lambda_o(E_e)$, the following function is constructed:

$$\lambda'(E_{obs}) = \int_0^\infty \lambda_o(E_e) R(E_{obs}, E_e) \mathcal{E}(E_e) dE_e, \quad (4.29)$$

where $R(E_{obs}, E_e)$ is the energy resolution function, and $\mathcal{E}(E_e)$ is the detection efficiency. The effect of these uncertainties is estimated by varying $R(E_{obs}, E_e)$ and $\mathcal{E}(E_e)$ by the above uncertainties until the simulated energy spectrum which includes the uncertainties, $\lambda'(E_{obs})$, matches the observed energy spectrum, $\lambda(E_{obs})$. The effect of the theoretical uncertainties in the ^8B neutrino energy spectrum is estimated in the same way.

The total energy correlated uncertainty in the flux measurement is $\pm 1.9\%$, while for the day/night flux asymmetry, it is ${}_{-1.1}^{+1.2}\%$. The total energy correlated (as well as the energy uncorrelated) uncertainties for each energy bin are presented in Tab. 4.2.

Energy Uncorrelated Uncertainties

All other sources or uncertainties contribute to the energy uncorrelated systematic uncertainties:

- **Trigger efficiency.** The trigger efficiency depends on the vertex position and water transparency. The systematic uncertainties due to trigger efficiency is estimated by comparing the measured trigger efficiency to the one from the MC simulation.

For the LE trigger, the efficiency above 7.0 MeV is 100% (0% uncertainty), while the maximum deviation of the MC simulated trigger efficiency from the measured one in the energy region of 6.5 – 7.0 MeV is obtained to be ${}^{+0.4}_{-1.7}\%$. For the SLE trigger, the deviation of the MC trigger efficiency from the measured one is obtained by taking the livetime-weighted average of such deviations in the period of each of the several SLE thresholds. The maximal deviation is: ${}^{+3.2}_{-1.6}\%$ for 5.0 – 5.5 MeV, ${}^{+0.9}_{-0.5}\%$ for 5.5 – 6.0 MeV, and 0% above 6.0 MeV.

The systematic uncertainty due to the IT is studied using the Ni/Cf source, by calculating the deviation between the reduction efficiency of the IT in data and that for the Ni/Cf MC simulation at various positions in the ID. The volume average of these deviations is obtained to be: $\pm 2.8\%$ for 5.0 – 5.5 MeV, $\pm 0.7\%$ for 5.5 – 6.0 MeV, and $\pm 0.3\%$ for 6.0 – 6.5 MeV; the IT has no effect on events with energies above 6.5 MeV.

- **Data Reduction.** The systematic uncertainties due to the data reduction algorithm comes from the reduction efficiency differences between data and MC simulation. The cuts that contribute a significant systematic uncertainty due to data reduction are:

- flasher cut, obtained from spallation data: $\ll 1\%$

- fiducial volume cut, measured by Ni/Cf calibration: $\ll 1\%$
- electronic noise cuts, measured by Ni/Cf calibration: $\pm 0.7\%$
- Cherenkov ring cut, estimated by using spallation data: ${}_{-0.5}^{+1.0}\%$

The total systematic uncertainty due to data reduction is $\pm 0.85\%$ in the energy spectrum measurement, and ${}_{-1.6}^{+2.1}\%$ in the total flux measurement.

- **Spallation deadtime.** The position and time dependence of the spallation deadtime is used to simulate the spallation cut in the MC simulation. By comparing the deadtime calculated from the simulation to the one calculated from the data, the systematic uncertainty is estimated to be $\pm 0.2\%$ in total flux and $\pm 0.1\%$ in the day/night asymmetry.
- **Gamma-ray cut.** Since the gamma-ray cut is based on the reconstructed vertex position and event direction, differences in vertex or directional resolution between the data and the MC simulation (as measured by the LINAC calibration) can introduce systematic uncertainties. To estimate the size of these uncertainties, the following method is adopted:

1. Shift the reconstructed vertex and direction of events by the size of the deviations in the vertex and directional resolutions.
2. Perform the gamma-ray cut on the modified events and compare the reduction efficiency with the one from the original data.

The systematic uncertainty due to the gamma-cut is obtained to be $\pm 0.1\%$ in the energy spectrum measurement, and $\pm 0.05\%$ in the neutrino flux measurement.

- **Vertex shift.** Systematic shifts in the reconstructed vertex relative to the original vertex is studied by Ni/Cf calibration at various ID positions. The

estimated systematic uncertainty due to a vertex shift is $\pm 0.2\%$ in the energy spectrum measurement, and $\pm 1.3\%$ in the flux measurement.

- **Non-flat background.** In the calculation of the solar neutrino background in Sec. 4.4.1, we assumed that the background shape was independent of the zenith angle, θ_z . Any possible θ_z asymmetry in the background shape or in the energy scale may introduce deviations from a flat $\cos\theta_{sun}$ distribution. These deviations are treated as a systematic uncertainty and are estimated to be: $\pm 1.2\%$ for $5.0 - 5.5$ MeV, $\pm 0.4\%$ for $5.5 - 6.0$ MeV, and $\pm 0.15\%$ above 6.0 MeV. For the flux measurement, this uncertainty is $\pm 0.1\%$, and for the day/night asymmetry, it is $\pm 0.4\%$.
- **Directional resolution.** The systematic uncertainty due to directional resolution is defined as the difference between the number of signal events obtained using the simulated directional resolution and that obtained using directional resolution generated from the data. The uncertainty is estimated to be $\pm 1.0\%$ for the energy spectrum measurement, and $\pm 0.6\%$ for the flux measurement.
- **Livetime.** The systematic uncertainty stemming from the livetime calculation is evaluated from the difference in these calculations using several data samples: raw data, muon data, LE triggered data. The uncertainty is estimated to be $\pm 0.1\%$ for the flux measurement and $\pm 0.1\%$ for the day/night asymmetry; livetime calculation does not generate systematic uncertainties in the energy spectrum measurement.

The total energy uncorrelated (as well as the energy correlated) uncertainties for each energy bin are presented in Tab. 4.2.

Table 4.2: Systematic uncertainties in the energy spectrum.

Energy (MeV)	Correlated error (%)	Uncorrelated error (%)
5.0 - 5.5	+0.24 -0.18	+3.5 -2.9
5.5 - 6.0	+0.22 -0.18	+1.6 -1.6
6.0 - 6.5	+0.33 -0.34	+1.4 -1.4
6.5 - 7.0	+0.52 -0.56	+1.4 -1.4
7.0 - 7.5	+0.75 -0.80	+1.4 -1.4
7.5 - 8.0	+1.0 -1.1	+1.4 -1.4
8.0 - 8.5	+1.4 -1.3	+1.4 -1.4
8.5 - 9.0	+1.7 -1.6	+1.4 -1.4
9.0 - 9.5	+2.1 -2.0	+1.4 -1.4
9.5 - 10.0	+2.5 -2.3	+1.4 -1.4
10.0 - 10.5	+3.0 -2.7	+1.4 -1.4
10.5 - 11.0	+3.5 -3.2	+1.4 -1.4
11.0 - 11.5	+4.0 -3.7	+1.4 -1.4
11.5 - 12.0	+4.5 -4.2	+1.4 -1.4
12.0 - 12.5	+5.1 -4.8	+1.4 -1.4
12.5 - 13.0	+5.8 -5.5	+1.4 -1.4
13.0 - 13.5	+6.5 -6.2	+1.4 -1.4
13.5 - 14.0	+7.3 -7.0	+1.4 -1.4
14.0 - 15.0	+8.6 -8.4	+1.4 -1.4
15.0 - 16.0	+11 -10	+1.4 -1.4
16.0 - 20.0	+16 -14	+1.4 -1.4

Chapter 5

Solar Neutrino Oscillation Analysis

5.1 Introduction

According to the standard solar model (SSM) [4], in the energy range to which SK-I is sensitive ($5 \sim 20$ MeV), the sun produces electron neutrinos (ν_e) in its core by the decay of ${}^8\text{B}$ (${}^8\text{B}$ neutrinos, $E_\nu = 0 \sim 16$ MeV), and by the fusion of ${}^3\text{He}$ with a proton (hep neutrinos, $E_\nu = 0 \sim 19$ MeV). If the ν_e did not undergo flavor oscillations (Sec. 2.3), we would expect them to propagate to the earth unaffected, and the solar neutrino detectors, like SK, should measure the neutrino flux predicted by the SSM ($5.05 \times 10^6 \text{ cm}^{-2}\text{s}^{-1}$ [4]). However, as stated in Sec. 2.2, all previous neutrino detectors have measured a neutrino flux deficit, which suggests either a flawed experiment or neutrino oscillations. With the recent emergence of a similar flux deficit measurement from a “second generation” neutrino experiment, SK (Sec. 4.4.2), it became clear that a flaw in the neutrino detection methods is highly unlikely, and neutrino flavor oscillations are the most probable reason for the apparent deficit. The subsequent solar neutrino flux deficit measurement from SNO [30] further supported this idea.

With the intention to finally solve this long-standing puzzle and demonstrate flavor oscillations in solar neutrinos, an oscillation analysis was done with the solar neutrino signal obtained from the SK data set, as described in Sec. 4.4.2. Due to

SK's large size and, therefore, high statistics in the data, the idea was primarily to discern a possible distortion in the energy spectrum or a day/night flux asymmetry as smoking-gun evidence for oscillations of solar neutrinos. A spectral distortion would favor the SMA and VAC solutions, while a day/night flux asymmetry favors the LMA and LOW solutions. In the absence of any such smoking-gun evidence (see Sec. 4.4.2), a more involved analysis, which involves all of SK data, was performed in order to discern solar neutrino oscillations in a more indirect way.

In addition, the solar neutrino data set from SNO was used, in order to enhance the effects measured by SK. The analysis is done in two steps: a model-independent analysis, which simply demonstrates evidence for solar neutrino oscillations without considering *any* specific characteristic of an oscillation model; and a model-dependent analysis, which distinguishes between the different oscillation solutions and restricts the range of possible oscillation models.

Having described the SK detector in detail in previous chapters, a brief overview of SNO is in order.

5.1.1 Overview of SNO

Sudbury Neutrino Observatory (SNO) [30, 31] is a spherical underground water Cherenkov neutrino detector located at a depth of 6010 m of water equivalent in the INCO, Ltd. Creighton mine in Sudbury, Ontario, Canada. It uses 1 kt of ultra-pure D_2O contained in a 12 m diameter spherical transparent acrylic vessel, surrounded by ultra-pure H_2O . The entire volume is contained in a 17.8 m diameter stainless steel geodesic sphere with 9,456 20-cm PMTs mounted on the inside wall. The geodesic sphere is immersed in additional H_2O in order to provide shielding from radioactivity in the rock.

SNO is designed for detecting solar neutrinos by measuring the rate of electrons created in the neutrino-electron elastic scattering (ES), similarly to SK, as well as

electrons and neutrons created by charged-current (CC) and neutral-current (NC) inelastic scattering of solar neutrinos on deuterium:

$$\begin{aligned}
\nu_x + e^- &\longrightarrow \nu_x + e^- \quad (ES) \\
\nu_e + d &\longrightarrow p + p + e^- \quad (CC) \\
\nu_x + d &\longrightarrow \nu_x + p + n \quad (NC).
\end{aligned}
\tag{5.1}$$

The ES and NC reactions are sensitive to all neutrino flavors (ν_x), while the CC reaction is sensitive exclusively to electron neutrinos (ν_e).

The SNO solar neutrino data set used in this analysis was collected from 2 November 1999 to 28 May 2001, for a total of 306.4 days of detector live time [30]. The energy threshold in the SNO result was $T_{eff} \geq 5.0$ MeV; this includes electron events with kinetic energy $T_e \geq 5.0$ MeV and events resulting from the 6.25 MeV γ -ray from neutron capture on deuterium [30].

5.2 Model-Independent Analysis

Relying on a previous analysis of Fogli et al. [32], a comparison analysis of the ^8B solar neutrino flux measurements by SK and SNO was conducted independent of an oscillation model. SK's $\nu_{e,\mu,\tau}$ (ES) total flux measurement and SNO's ν_e (CC) flux measurement were used in the analysis. Using SNO's ν_e flux measurement we can extract the $\nu_{\mu,\tau}$ flux from SK's data. The contribution of $\nu_{\mu,\tau}$ to the total SK rate is about 1/7 of that of ν_e .

With an appropriate choice of energy thresholds, the two experiments happen to have virtually the same response function to ^8B solar neutrinos. The consequence is that we can use the two flux measurements in an analysis without considering a particular oscillation scenario and the specificities of detector characteristics. This is possible because in this analysis we assume an undistorted ^8B neutrino spectrum; significant spectral distortions are ruled out by the data. In such a case, even effects

due to the ^8B neutrino energy spectrum shape itself cancel out between the two experiments.

With the response functions being virtually the same, we can set up the following system of equations:

$$\begin{aligned}\Phi_{\text{SNO}} &= \Phi_\nu \langle P_{e-e} \rangle && (\nu_e) \\ \Phi_{\text{SK}} &= \Phi_\nu \langle P_{e-e} \rangle + \Phi_\nu \frac{\sigma_{\mu,\tau}}{\sigma_e} \langle P_{e-\mu,\tau} \rangle && (\nu_{e,\mu,\tau}),\end{aligned}\quad (5.2)$$

where Φ_ν is the true total ^8B solar neutrino flux, $\langle P_{e-e} \rangle$ is the ν_e survival probability (energy-averaged over the common SK and SNO response function), $\langle P_{e-\mu,\tau} \rangle$ is the $\nu_e \rightarrow \nu_{\mu,\tau}$ oscillation probability, and $\sigma_{\mu,\tau}/\sigma_e$ is the energy averaged cross section ratio (i.e. the ratio of SK's sensitivity to $\nu_{\mu,\tau}$ with respect to ν_e). Assuming neutrinos oscillate into only active flavors, we can write $\langle P_{e-\mu,\tau} \rangle = 1 - \langle P_{e-e} \rangle$. The assumption of only active flavor oscillations is used throughout the analysis. Eq.5.2 can be rewritten in order to extract the $\nu_{\mu,\tau}$ flux ($\Phi_{\mu,\tau}$) from the sun, which is direct evidence for neutrino oscillations ($\nu_e \rightarrow \nu_{\mu,\tau}$):

$$\begin{aligned}\Phi_{\text{SNO}} &= \Phi_e \\ \Phi_{\text{SK}} &= \Phi_e + \Phi_{\mu,\tau} \frac{\sigma_{\mu,\tau}}{\sigma_e}.\end{aligned}\quad (5.3)$$

5.2.1 Detector Response Function Equivalence

The ^8B response function with an electron kinetic energy threshold, T_{min} , of either detector is given by [33]:

$$\rho(E_\nu, T_{\text{min}}) = \frac{\lambda(E_\nu)\sigma(E_\nu, T_{\text{min}})}{\int dE_\nu \lambda(E_\nu)\sigma(E_\nu, T_{\text{min}})},\quad (5.4)$$

where $\lambda(E_\nu)$ is the ^8B neutrino energy spectrum shape, and $\sigma(E_\nu, T_{\text{min}})$ is the total neutrino scattering cross section, given by:

$$\sigma(E_\nu, T_{\text{min}}) = \int_{T_{\text{min}}} dT_r \int dT_e R(T_r, T_e) \frac{d\sigma(E_\nu, T_e)}{dT_e},\quad (5.5)$$

where T_e is the true electron kinetic energy, T_r is the electron reconstructed kinetic energy, and $R(T_r, T_e)$ is the energy resolution function of the detector. The differential cross section function ($d\sigma/dT$) for the $\nu + e$ elastic scattering (SK) was obtained from Ref. [26], and the differential cross section for the $\nu + d$ charged-current absorption from Ref. [34].

In Ahmad et al. [30], the SNO collaboration published their most recent electron kinetic energy threshold of $T_{\text{SNO}} \geq 5.0$ MeV for the charged current (CC) interaction measurement of the ν_e flux. Their corresponding energy resolution function was quoted as:

$$R_{\text{SNO}}(T_e, T_r) = \frac{1}{\sqrt{2\pi} \sigma_T} e^{-\frac{1}{2}(T_r - T_e)/\sigma_T^2}$$

$$\sigma_T(T_e) = -0.0684 + 0.331\sqrt{T_e} + 0.0425 T_e . \quad (5.6)$$

Function $\sigma_T(T_e)$ was obtained from energy calibration and MC simulation [30].

In order to match the SK and SNO flux results, the appropriate energy threshold for SK has to be calculated, such that SK's corresponding response function matches SNO's published response function given above. To do this, a MC simulation of recoil electron events inside SK was performed. A total of 10^7 MC events were generated, using the ^8B and hep neutrino flux [4] and energy spectrum [25] and the ES interaction cross section [26] as the input. The GEANT detector simulator was then used to generate the energies, as measured by the detector, of electron events that passed a series of the official SK solar neutrino analysis cuts. Note that at SK we measure the total energy (E_r) of the recoil electron instead of kinetic energy (T_r), which is measured at SNO. The result of this simulation was a numerically constructed matrix of E_e vs. E_r values ($R_{\text{SK}}(E_e, E_r)$), and normalized so that each E_e slice is normalized to 1:

$$\int dE_r R_{\text{SK}}(E_e, E_r) = 1 . \quad (5.7)$$

Having both $R_{\text{SNO}}(T_e, T_r)$ and $R_{\text{SK}}(E_e, E_r)$, we can calculate both $\rho_{\text{SNO}}(E_\nu, T_{\text{min}}^{\text{SNO}})$

and $\rho_{\text{SK}}(E_\nu, E_{\text{min}}^{\text{SK}})$. In order to obtain $\rho_{\text{SNO}} = \rho_{\text{SK}}$, we vary $E_{\text{min}}^{\text{SK}}$ until the quantity

$$\delta = \int dE_\nu |\rho_{\text{SK}} - \rho_{\text{SNO}}| \quad (5.8)$$

is minimized [33]. For SNO's published kinetic energy threshold of $T_{\text{min}}^{\text{SNO}} = 5.0$ MeV, the corresponding total energy threshold of SK that equalizes the two response functions is $E_{\text{min}}^{\text{SK}} = 7.2$ MeV ($T_{\text{min}}^{\text{SK}} = 6.7$ MeV). Fig. 5.1 shows the SNO response as a function of neutrino energy (*marker*) and SK response function for various energy thresholds (*line*).

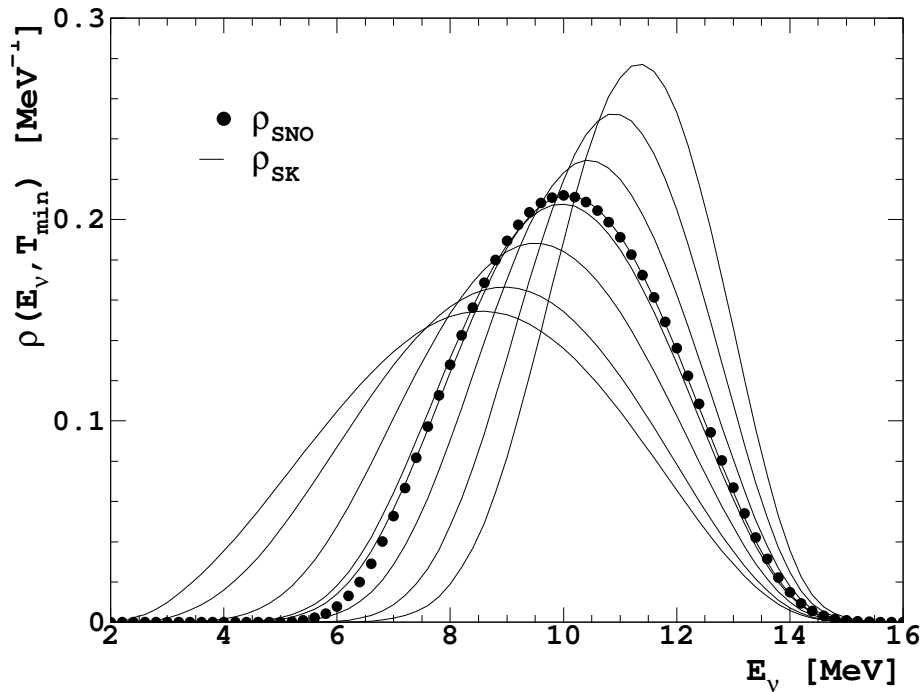


Figure 5.1: SNO response as a function of neutrino energy (*dot*) overlaid with SK response function for various SK energy thresholds (4, 5, 6, 7, 7.2, 8, 9, and 10 MeV). The two response functions match almost perfectly at $E_{\text{min}}^{\text{SK}} = 7.2$ MeV ($T_{\text{min}}^{\text{SK}} = 6.7$ MeV).

5.2.2 Flux Data Extraction

SNO's published solar ν_e flux for the $T \geq 5.0$ MeV threshold [30] is:

$$\Phi_e^{\text{SNO}} = 1.76_{-0.05}^{+0.05}(\text{sta.})_{-0.09}^{+0.09}(\text{sys.})_{-0.03}^{+0.03}(\text{theor.}) \times 10^6 \text{cm}^{-2} \text{s}^{-1}. \quad (5.9)$$

To obtain SK's total solar ν flux measured with the $E \geq 7.2$ MeV threshold, I used SK's official solar neutrino data extraction tool (solfit), which uses a maximum likelihood method to extract the solar neutrino events from the final data sample (events after all the official reduction cuts). Solfit fits the expected shape of the $\cos\theta_{sun}$ distribution of the events (cosine of the angle between the recoil electron direction and the direction of the sun) and the estimated background shape to the final data. The shapes of the $\cos\theta_{sun}$ angular distribution and the background distribution were recalculated with the new energy threshold of 7.2 MeV. The systematic uncertainties of our flux measurement also had to be re-estimated. The biggest impact of the new energy threshold was on the energy-correlated systematic uncertainties, while the energy-uncorrelated ones did not change significantly.

With the new, corrected signal extraction parameters in place, SK's total solar neutrino flux (Φ_ν) for the 7.2 MeV threshold is:

$$\Phi_\nu^{\text{SK}} = 2.313_{-0.027}^{+0.027}(\text{sta.})_{-0.093}^{+0.097}(\text{sys.}) \times 10^6 \text{cm}^{-2}\text{s}^{-1}. \quad (5.10)$$

5.2.3 Results of the Fit

From Eq. 5.2, and using the flux measurements in Eq. 5.9 and 5.10, we can define the χ^2 in the following way:

$$\chi^2 = \left(\frac{\Phi_{\text{SNO}} - \Phi_\nu P_{e-e}}{\delta\Phi_{\text{SNO}}} \right)^2 + \left(\frac{\Phi_{\text{SK}} - \Phi_\nu (P_{e-e}(1-y) + y)}{\delta\Phi_{\text{SK}}} \right)^2, \quad (5.11)$$

where $y = \sigma_{\mu,\tau}/\sigma_e$ is calculated numerically by a MC simulation of solar neutrinos. In the calculation we assumed a ${}^8\text{B}$ energy spectrum distribution for both ν_e and $\nu_{\mu,\tau}$. In both cases we simulated 10^5 $\nu + e$ elastic scattering events with proper treatment of the energetics involved. The resulting recoil electrons were then submitted to the official detector simulator, and the final events that passed all the official reduction cuts, including the 7.2 MeV total energy cut, were counted. The SK sensitivity ratio, $\sigma_{\mu,\tau}/\sigma_e$, is the ratio of the number of the final $\nu_{\mu,\tau}$ events to the number of the final

ν_e events ($N_{\mu,\tau}/N_e$). This ratio was calculated to be:

$$y = \frac{\sigma_{\mu,\tau}}{\sigma_e} = 0.152 . \quad (5.12)$$

The first step in the χ^2 fitting was to calculate the 1σ allowed regions for the Φ_ν and P_{e-e} parameters, stemming from the SK flux result and the SNO flux result, separately. This is done by breaking up the above defined χ^2 into its two parts. The result of the fit is shown in Fig. 5.2. Both best-fit points are well below $P_{e-e} = 1$, and the two 1σ regions overlap around $P_{e-e} = 0.35$ and $\Phi_\nu = 5 \times 10^6 \text{ cm}^{-2} \text{ s}^{-1}$. Note that the overlap is in the region of the total solar neutrino flux predicted by the SSM (dotted lines). This gives us confidence that the SSM prediction is valid, and that we are inferring the full flux and not missing any neutrinos.

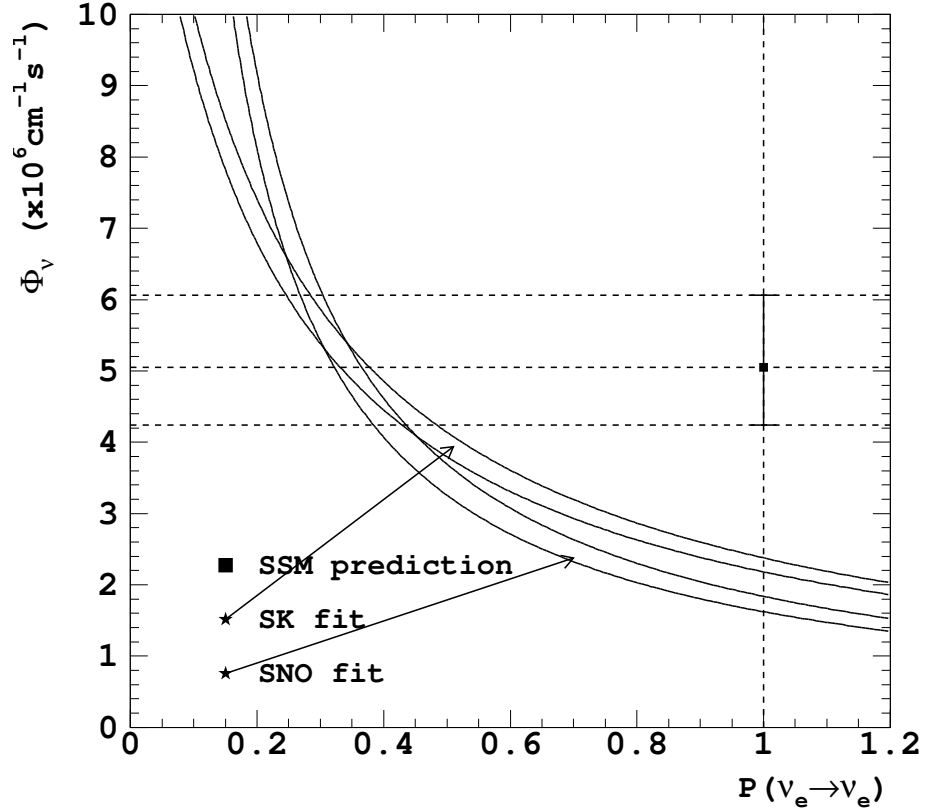


Figure 5.2: Allowed 1σ regions for the SK and SNO model-independent flux results, separately.

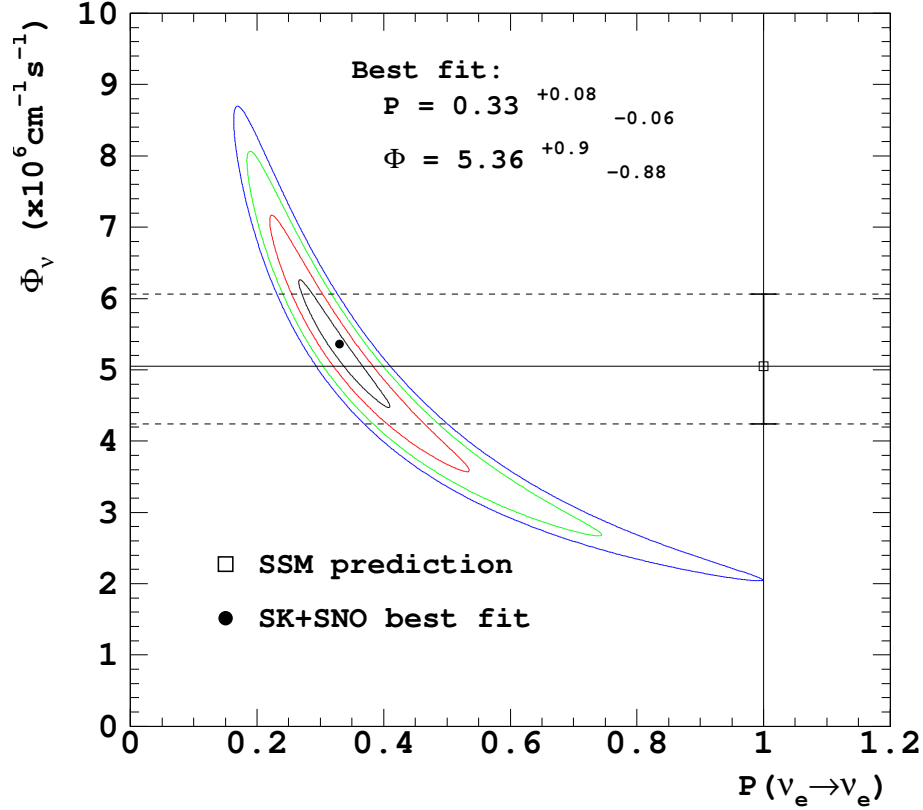


Figure 5.3: Allowed regions for the combined model-independent SK+SNO flux result. The regions shown are 1σ , 2σ , 3σ , and 3.7σ . The best-fit point is $\Phi_\nu = 5.36_{-0.88}^{+0.90} \times 10^6 \text{ cm}^{-2} \text{ s}^{-1}$ and $\langle P_{e-e} \rangle = 0.33_{-0.06}^{+0.08}$. The no-oscillation prediction of the SSM is ruled out at 3.7σ .

Fig. 5.3 presents the combined fit from Eq. 5.11. It shows the allowed regions of 1σ , 2σ , 3σ , and 3.7σ . The best-fit point of the combined analysis is:

$$\begin{aligned}\Phi_\nu &= 5.36_{-0.88}^{+0.90} \times 10^6 \text{ cm}^{-2} \text{ s}^{-1} \\ \langle P_{e-e} \rangle &= 0.33_{-0.06}^{+0.08} .\end{aligned}\quad (5.13)$$

This result is 3.7σ away from the SSM's no-oscillation scenario, while the total solar neutrino flux inferred is well within the SSM prediction.

As the final step, we used Eq. 5.3 to set up a χ^2 fit for obtaining the value of the $\nu_{\mu,\tau}$ solar flux directly:

$$\chi^2 = \left(\frac{\Phi_{\text{SNO}} - \Phi_e}{\delta\Phi_{\text{SNO}}} \right)^2 + \left(\frac{\Phi_{\text{SK}} - \Phi_e - y\Phi_{\mu,\tau}}{\delta\Phi_{\text{SK}}} \right)^2 .\quad (5.14)$$

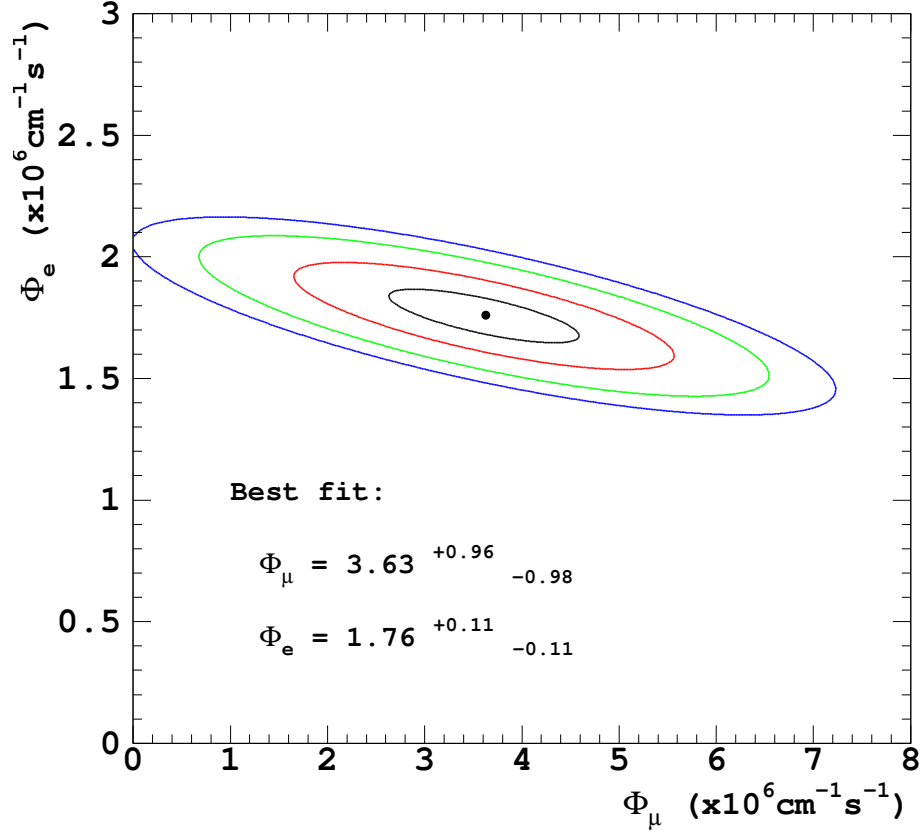


Figure 5.4: Allowed regions for the solar $\nu_{\mu,\tau}$ flux stemming from the combined model-independent SK+SNO flux result. The regions shown are 1σ , 2σ , 3σ , and 3.7σ . The best-fit point is $\Phi_{\mu,\tau} = 3.63^{+0.96}_{-0.98} \times 10^6 \text{ cm}^{-2} \text{ s}^{-1}$. This value is 3.7σ away from zero.

The result of the fit is presented in Fig. 5.4. The figure displays the same 1σ , 2σ , 3σ , and 3.7σ allowed regions, and shows that our inferred $\nu_{\mu,\tau}$ flux:

$$\Phi_{\mu,\tau} = 3.63^{+0.96}_{-0.98} \times 10^6 \text{ cm}^{-2} \text{ s}^{-1}$$

is 3.7σ away from zero.

5.3 Full, Model-Dependent Analysis

In order to fully utilize the power of all of SK's and SNO's data, a much more detailed, model-dependent oscillation analysis was done. In this case, there was no

emphasis placed on the cleverness of utilizing the data; instead, all the available data were used.

5.3.1 Detector Response Functions

In order to use the full data sets from both detectors, the correct corresponding detector response functions to ${}^8\text{B}$ and hep neutrinos had to be calculated, while considering all of the detector's specificities. The general form of a detector response function is given in Eq. 5.4 and 5.5. The detector specific properties then enter into the response function in the form of the energy resolution function, R_E (i.e. the energy resolution, σ_E):

$$\begin{aligned} R_E(E_e, E_r) &= \frac{1}{\sqrt{2\pi} \sigma_E} e^{-\frac{1}{2}(E_r - E_e)/\sigma_E^2} \\ \sigma_E/E_e &= A \oplus B/\sqrt{E_e}, \end{aligned} \quad (5.15)$$

where E_e is the recoil electron total energy, and E_r is this total energy measured by the detector (i.e. reconstructed energy).

SK's energy resolution is constructed by using the numerical matrix $R_{\text{SK}}(E_e, E_r)$ from the MC simulation described in Sec. 5.2.1. This matrix was divided into slices of 0.1 MeV in E_e , and each slice was fit with the energy resolution function R_E (from Eq. 5.15). The energy resolution, σ_E , was then fit to the result of the previous fit. Special care had to be taken in constructing the energy resolution, because there is a discontinuity in the efficiency at $E_r = 6.5$ MeV, due to the gamma-ray cut (see the section on data reduction for details). Thus, two σ_E functions were constructed:

$$\begin{aligned} \sigma_{E,1}/E_e &= \frac{0.354}{\sqrt{E_e}} & (E_r < 6.5 \text{ MeV}) \\ \sigma_{E,2}/E_e &= 0.0644 \oplus \frac{0.403}{\sqrt{E_e}} & (E_r \geq 6.5 \text{ MeV}). \end{aligned} \quad (5.16)$$

The results of the σ_E fits are shown in Fig. 5.5.

SNO's published energy resolution (expressed in terms of electron kinetic energy) from Eq. 5.6 is used.

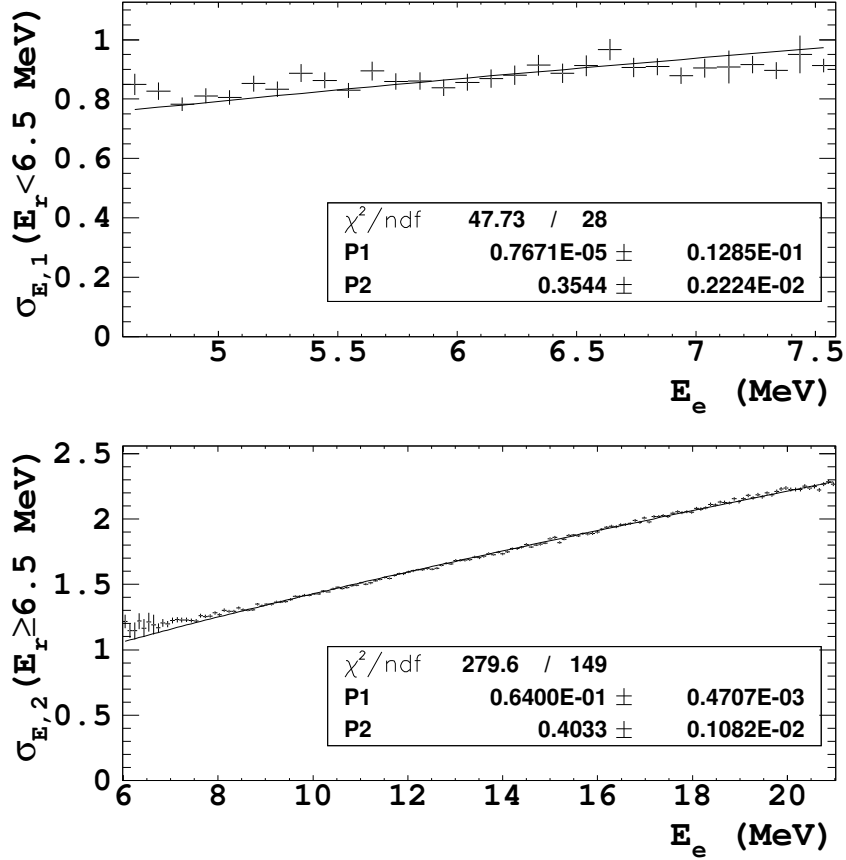


Figure 5.5: SK energy resolution for $E_r < 6.5$ MeV (*upper*) and for $E_r \geq 6.5$ MeV (*lower*).

5.3.2 Oscillation Predictions and Data Measurements

With the proper understanding of the detector's response to solar neutrinos, the predictions of the following quantities were calculated from specific neutrino oscillation models (as described in Sec. 2.3):

- SK's 21-bin energy spectrum shape
- SK's day/night flux asymmetry
- SK's unbinned zenith angle distribution (includes total rate)
- SNO's 17-bin energy spectrum shape with total rate

Each prediction is a basic convolution of the ^8B and hep neutrino flux (Φ_ν) [4] and energy spectrum (λ) [25], the oscillation probability at the detector (P), the

interaction cross section for the ES, CC, and NC processes ($d\sigma/dE_e$) [26, 34], and the detector energy resolution function (R_E):

$$R(E_r) = \Phi_\nu \int \int \lambda(E_\nu) P(E_\nu) \frac{d\sigma(E_\nu)}{dE_e} R_E(E_e, E_r) dE_e dE_\nu. \quad (5.17)$$

The difference between the different predicted quantities is merely in the way this basic rate prediction is organized and binned.

The oscillation probability was calculated separately for oscillations in vacuum (see Sec. 2.3.1) and for oscillations inside the sun and the earth (MSW effect, see Sec. 2.3.2). The radial dependence of the sun’s electron density was included in the calculation.

Oscillation Predictions

The prediction of the SK 21-bin recoil electron total energy spectrum shape was created by first calculating the rate, R , as a function of the reconstructed energy, and then binning it into 21 bins (as defined in Sec. 4.4.2)). The SSM spectrum prediction was also made for SK in a similar way (with $P = 1$), and the final spectral shape prediction was used as PRED/SSM.

The prediction of SNO’s 17-bin electron kinetic energy spectrum shape was made similarly, by first calculating the ES, CC, and NC contributions to the total rate, R (using the relevant cross sections and SNO’s energy resolution), adding them together, and then binning R into 17 bins (16 bins of 0.5 MeV between 5.0 and 13.0 MeV, and 13.0 – 14.0 MeV). Again, the SSM spectrum prediction was also made (with $P = 1$), and a ratio PRED/SSM was constructed. However, since SNO’s NC rate is independent of the oscillation model, SNO’s spectral shape includes the ratio of CC/NC, and thus implicitly includes the total rate (i.e. SNO’s PRED/SSM spectral shape is dependent on the neutrino total flux, unlike SK’s spectral shape).

The prediction of SK’s day/night flux asymmetry was made by calculating R for the “day” live times (i.e. when the sun was above the horizon) and for the “night”

live times (i.e. when the sun was below the horizon) and combining them into an asymmetry quantity (Eq. 4.28).

An unbinned zenith angle distribution is a much more powerful tool for discerning a day/night flux asymmetry than the simple asymmetry quantity, A_{dn} , because it considers solar neutrino events one at a time. Its prediction was not independently calculated, but only in conjunction with the two spectral predictions. The way this was done is described below (Sec. 5.3.4).

Data Measurements

All of the aforementioned oscillation predictions were calculated separately for both ^8B and hep neutrinos. All SSM predictions were calculated by adding the ^8B and hep contributions together (see Sec. 5.3.4).

The same four quantities were also obtained from SK and SNO data sets. SK's spectral shape distribution (DATA/SSM) was obtained by the standard solar neutrino signal extraction tool (solfit), described in Sec. 4.4. It is presented in Fig. 5.6. The absolute measured SK recoil electron energy spectrum is shown in Tab. 4.1 along with its SSM prediction.

SNO's spectral shape (DATA/SSM) was constructed by adding SNO's published absolute day and night spectra [30] and normalizing them by the aforementioned SSM prediction. The resulting spectral shape for SNO is shown in Fig. 5.7. Note the "bump" at the lower end of the spectrum. This is due to the fact that while the CC contribution to the total event spectrum is decreased by the oscillations, the NC contribution (which includes all neutrino flavors and peaks at ~ 5 MeV [30]) remains unaffected. Therefore, when taking the ratio DATA/SSM, the bins near 5 MeV will have an apparent excess of events. The absolute measured SNO energy spectrum is shown in Tab. 5.1 along with its SSM prediction. These numerical values are obtained from the SNO web page [35], and cast into the appropriate units.

Table 5.1: SNO energy spectrum.

Energy (MeV)	DATA (ev./day)	SSM (ev./day)	DATA/SSM (\pm stat.err.)
5.0 - 5.5	1.380 ± 0.080	2.389	0.577 ± 0.034
5.5 - 6.0	1.277 ± 0.067	2.418	0.528 ± 0.028
6.0 - 6.5	1.151 ± 0.063	2.323	0.495 ± 0.027
6.5 - 7.0	0.980 ± 0.057	2.166	0.453 ± 0.027
7.0 - 7.5	0.904 ± 0.055	1.993	0.454 ± 0.027
7.5 - 8.0	0.694 ± 0.048	1.814	0.382 ± 0.026
8.0 - 8.5	0.527 ± 0.042	1.624	0.325 ± 0.026
8.5 - 9.0	0.577 ± 0.043	1.418	0.407 ± 0.031
9.0 - 9.5	0.395 ± 0.036	1.199	0.329 ± 0.030
9.5 - 10.0	0.359 ± 0.034	0.977	0.367 ± 0.035
10.0 - 10.5	0.271 ± 0.030	0.766	0.353 ± 0.039
10.5 - 11.0	0.235 ± 0.028	0.577	0.407 ± 0.048
11.0 - 11.5	0.157 ± 0.023	0.416	0.377 ± 0.054
11.5 - 12.0	0.085 ± 0.017	0.287	0.296 ± 0.058
12.0 - 12.5	0.062 ± 0.014	0.189	0.328 ± 0.075
12.5 - 13.0	0.059 ± 0.014	0.119	0.493 ± 0.116
13.0 - 20.0	0.039 ± 0.011	0.163	0.240 ± 0.069

SK's day/night flux asymmetry value ($A_{dn} = -0.019 \pm 0.025$) was obtained by extracting the total day and night fluxes (R_d and R_n) with solfit, and combining them into Eq. 4.28.

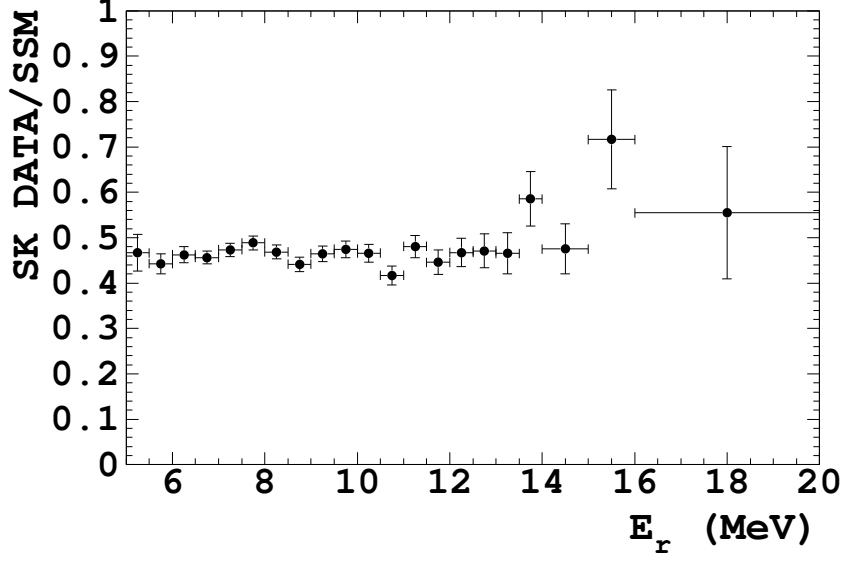


Figure 5.6: SK recoil electron total energy spectral shape used in the analysis.

5.3.3 SK Fit Results

A χ^2 function was then constructed using various combinations of these quantities obtained both from the data and the theoretical prediction. First, the SK spectral shape, day/night asymmetry and total rate were used in the SK-only fit. The three basic elements of this initial χ^2 fit are:

$$\begin{aligned}
 \chi_{\text{SK}}^2 &= \sum_{i=1}^{21} \frac{(d_i^{\text{SK}} - B f_i^{\text{SK}} p_i^{\text{b8}} - H f_i^{\text{SK}} p_i^{\text{hep}})^2}{\sigma_i^2} + (\delta_\lambda)^2 + (\delta_S^{\text{SK}})^2 + (\delta_R^{\text{SK}})^2 \\
 \chi_{dn}^2 &= \frac{(d_{dn} - p_{dn}^{\text{b8}})^2}{\sigma_{dn}^2} \\
 \chi_R^2 &= \frac{(d_R - B p_R^{\text{b8}} - H p_R^{\text{hep}})^2}{\sigma_R^2},
 \end{aligned} \tag{5.18}$$

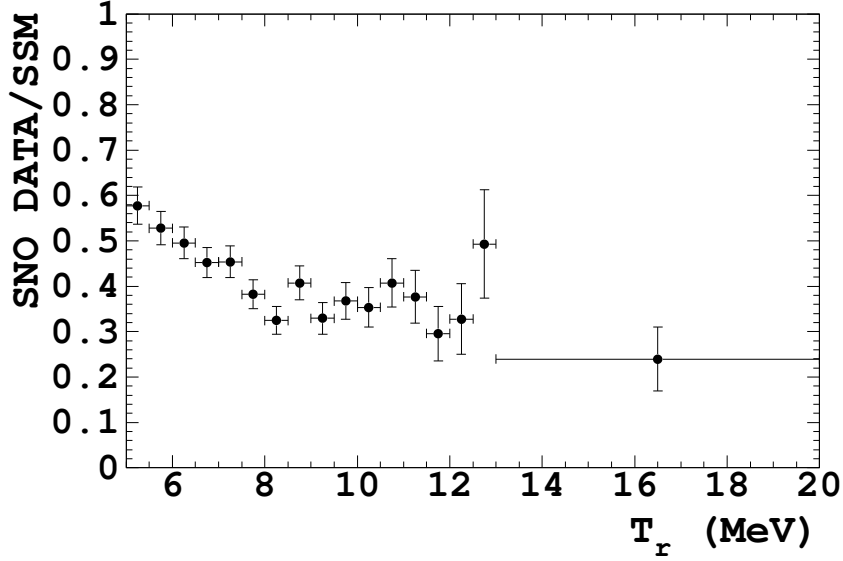


Figure 5.7: SNO kinetic energy event spectral shape used in the analysis. Note that SNO’s spectral shape implicitly includes the total neutrino rate.

where d_i and p_i are the SK spectral bins obtained from the data and the prediction, respectively:

$$d_i = \frac{\text{DATA}_i}{b8_i^{ssm} + \text{hep}_i^{ssm}}, \quad p_i^{b8, \text{hep}} = \frac{\{b8, \text{hep}\}_i^{osc}}{b8_i^{ssm} + \text{hep}_i^{ssm}}. \quad (5.19)$$

B and H are the parameters for the total ${}^8\text{B}$ and hep fluxes, respectively. The ${}^8\text{B}$ flux was constrained to the SSM prediction ($1.00_{-0.16}^{+0.20} \times \text{SSM}$) in this initial SK fit, but was kept free subsequently; the hep flux was kept free throughout the analysis. The spectral shape uncertainties (σ_i) are only the statistical uncertainties, which are uncorrelated between the energy bins. The σ_{dn}^2 and σ_R^2 quantities are the total statistical and systematic uncertainties for the day/night flux asymmetry and the total rate, respectively.

For the energy spectral shape, special care had to be taken in order to account for energy-correlated systematic errors. This was done by introducing free parameters for the ${}^8\text{B}$ spectral shape (δ_λ), detector’s energy scale (δ_s), and detector’s energy res-

olution (δ_r) into the fit. The function f_i was then constructed with these parameters:

$$f_i = \begin{cases} d_i \geq (p_i^{b8} + p_i^{hep}), & (1 + \delta_\lambda \varepsilon_i^{\lambda^+}) \times (1 + \delta_s \varepsilon_i^{s^+}) \times (1 + \delta_r \varepsilon_i^{r^+}) \\ d_i < (p_i^{b8} + p_i^{hep}), & (1 - \delta_\lambda \varepsilon_i^{\lambda^-}) \times (1 - \delta_s \varepsilon_i^{s^-}) \times (1 - \delta_r \varepsilon_i^{r^-}) . \end{cases} \quad (5.20)$$

The ε quantities are experimentally determined shapes of the three energy-correlated quantities. They were obtained by varying each of the three quantities independently by 1σ , and measuring the effect these variations had on the energy spectrum. For SK's data, this was done by using the signal extraction tool, solfit, in the extraction of the energy spectrum. The δ parameters are expressed in the units of the 1σ uncertainty, and were varied in steps of 0.1σ in the range of $\pm 10\sigma$, in order to find the best-fit values of the energy-correlated systematic uncertainties. In the day/night flux asymmetry, the hep prediction is insignificant, and was therefore ignored. Subsequently, the B parameter drops out of the ${}^8\text{B}$ prediction of the asymmetry.

In order to incorporate the total energy-uncorrelated systematic uncertainty of the energy spectrum (i.e. the systematic uncertainty that affects all the energy bins together, in the same way), the χ_{SK}^2 was first minimized and then a Taylor expansion performed around the χ_{min}^2 :

$$\begin{aligned} \chi_{\text{SK}}^2(B_o, H_o) &= [\chi_{\text{SK}}^2]_{\text{min}} + \frac{1}{2} \begin{pmatrix} B - B_o \\ H - H_o \end{pmatrix}^T \alpha C \begin{pmatrix} B - B_o \\ H - H_o \end{pmatrix} \\ &= [\chi_{\text{SK}}^2]_{\text{min}} + \frac{1}{2} \alpha \left[\sum_{i=1}^{21} \frac{(p_i^{b8})^2}{\sigma_i^2} (B - B_o)^2 + \sum_{i=1}^{21} \frac{(p_i^{hep})^2}{\sigma_i^2} (H - H_o)^2 + \right. \\ &\quad \left. + 2 \sum_{i=1}^{21} \frac{(p_i^{b8} p_i^{hep})}{\sigma_i^2} (B - B_o)(H - H_o) \right] \end{aligned}$$

B_o and H_o are the best-fit parameters from the original fit, and B and H are the new free parameters. Finally, the SK-only χ^2 function was constructed from all the SK components:

$$\chi_{\text{SKonly}}^2 = \chi_{\text{SK}}^2(B_o, H_o) + \chi_{dn}^2 + \chi_R^2 . \quad (5.21)$$

The result of the SK fit is shown in Fig. 5.8, which shows the allowed and excluded regions in the Δm^2 vs. $\tan^2\theta$ oscillation parameter space from this fit. The overall

best-fit solution (χ^2_{min}) was first found, and then the contour map was made by calculating the $\Delta\chi^2$ at each point with respect to the minimum. The 1σ (black, $\Delta\chi^2 \leq 4.61$) and the 95% c.l. (red, $\Delta\chi^2 \leq 5.99$) contours are allowed regions, while the 3σ (green, $\Delta\chi^2 \leq 11.83$) contours are excluded regions of this fit. This same method was used in all subsequent similar plots.

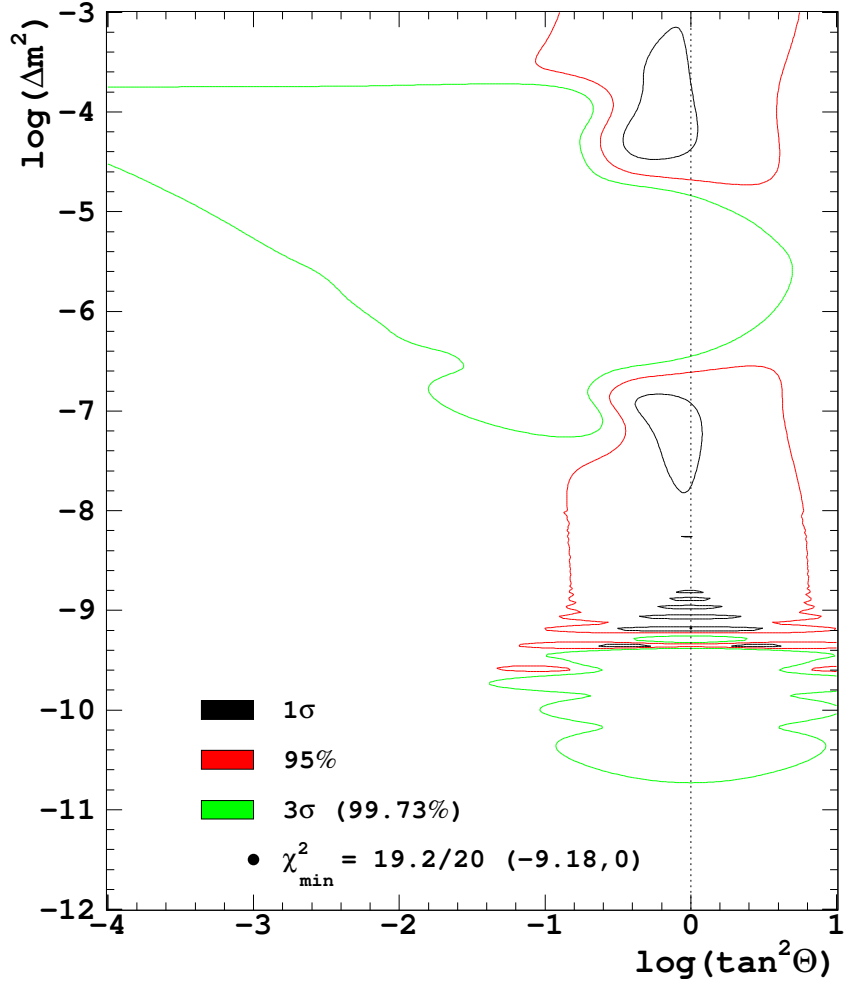


Figure 5.8: The χ^2 fit map of oscillation parameters for the SK energy spectral shape, simple day/night flux asymmetry, and total rate (constrained to the SSM prediction). The 1σ (black) and the 95% c.l. (red) contours are allowed regions, while the 3σ (green) contours are excluded regions.

At 1σ and 95% c.l., the SK fit alone picks out the LMA and LOW solutions, as well as traces of the VAC and quasi-VAC (a region between VAC and LOW) regions.

See Sec.2.4 for the definitions of the various solution regions. The flat spectral shape (as compared to the SSM prediction) combined with the non-existence of any significant day/night flux asymmetry rules out (at 3σ) the large parameter region for $-7 < \log(\Delta m^2) < -4$. Parts of the VAC region with the highest mixing angle are also ruled out at 3σ .

Although it does not greatly restrict the oscillation parameter space, the SK fit gives important hints on the tendencies of the oscillation models. Its significance lies in the ability to discern with great precision the lack of spectral fluctuations and day/night flux asymmetry.

The best-fit oscillation model ($\chi_{min}^2 = 19.2/20$ d.o.f.) is in the VAC region: $\Delta m^2 = 9.2 \times 10^{-10}$ eV², $\tan^2\theta = 1.0$. The ⁸B and hep neutrino fluxes obtained from this best-fit model are $0.80 \times \text{SSM}$ and $1.8 \times \text{SSM}$, respectively. Besides restricting (at 95% c.l.) the oscillation parameter space to the LMA, LOW and VAC regions, the SK fit also gives important hints on the general tendencies of the oscillation models. Its significance includes the ability to discern with great precision zero spectral fluctuations and zero day/night flux asymmetry.

5.3.4 SK+SNO Fit Results

The addition of SNO's spectral information to the SK fit significantly improves the oscillation result. A χ^2 function for the SNO spectral shape is defined similar to the one for SK (χ_{SK}^2 , from Eq.5.18):

$$\chi_{SNO}^2 = \sum_{j=1}^{17} \frac{(d_j^{SNO} - B f_j^{SNO} p_j^{b8} - H f_j^{SNO} p_j^{hep})^2}{\sigma_j^2} + (\delta_\lambda)^2 + (\delta_S^{SNO})^2 + (\delta_R^{SNO})^2. \quad (5.22)$$

All the components of the χ_{SNO}^2 function correspond to the similar ones of the χ_{SK}^2 function. SNO's ε values (which enter into the f_j functions similar to Eq.5.20) were taken from Ref.[36], and they result from the total systematic uncertainty of the energy spectrum. There is no distinction between the energy-correlated and energy-

uncorrelated systematic uncertainties in the SNO energy spectrum measurement [30].

The SNO spectral shape χ^2 component is then combined with the SK spectral shape and day/night asymmetry components, into the SK+SNO total χ^2 function:

$$\chi_{\text{SK+SNO}}^2 = \chi_{\text{SK}}^2 + \chi_{\text{SNO}}^2 + \chi_{dn}^2 . \quad (5.23)$$

The ${}^8\text{B}$ flux was kept free in the SK+SNO fit and all subsequent fits. The free parameter for the ${}^8\text{B}$ neutrino spectral shape systematic uncertainty, δ_λ , was used as the same parameter in both χ_{SK}^2 and χ_{SNO}^2 .

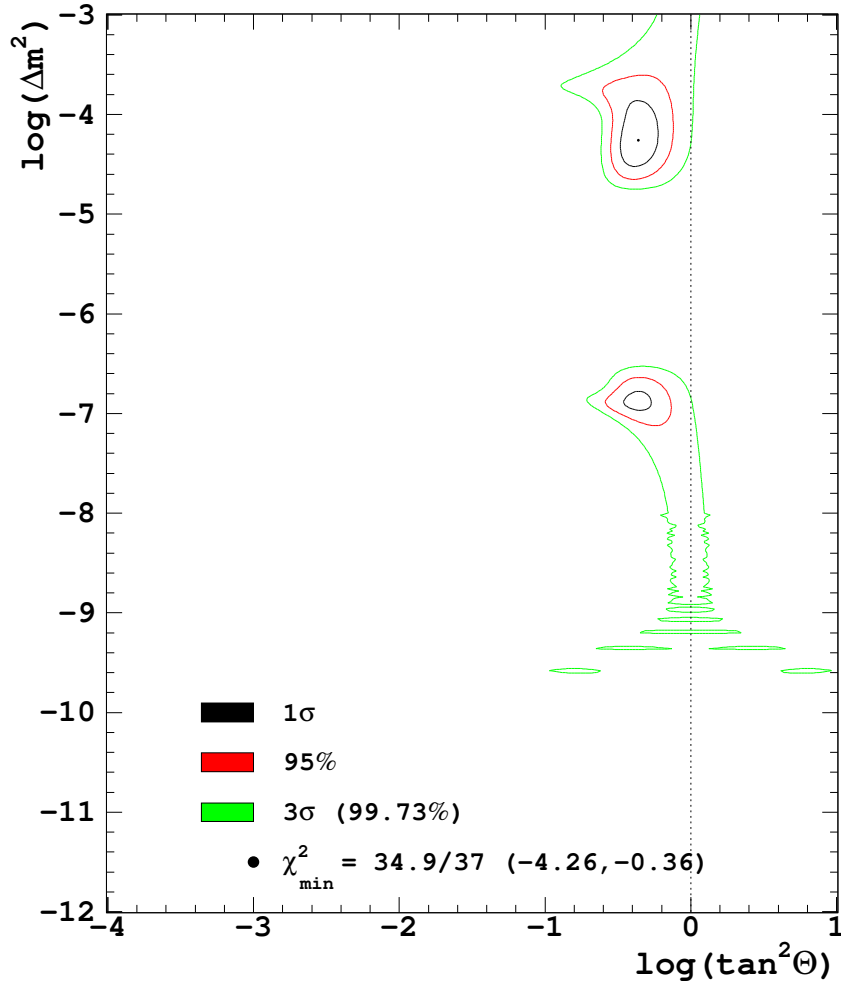


Figure 5.9: The χ^2 fit map of oscillation parameters for the SK and SNO energy spectral shapes and the SK day/night flux asymmetry.

The result of this SK+SNO fit is shown in Fig. 5.9. This fit is relatively restrictive

of the range of possible parameters: the only allowed regions at 3σ are the LMA and LOW regions, and small traces of the quasi-VAC region. The best-fit point ($\chi^2_{min} = 34.9/37$ d.o.f.) is in the LMA region: $\Delta m^2 = 5.5 \times 10^{-5} \text{ eV}^2$, $\tan^2\theta = 0.44$. The ^8B and hep neutrino fluxes obtained from this best-fit oscillation model are $1.09 \times \text{SSM}$ and $0.29 \times \text{SSM}$, respectively.

Replacing the simple day/night flux asymmetry in the previous fit with the full, unbinned zenith angle distribution of the neutrino flux, presents the SK+SNO solar neutrino oscillation final result. In order to avoid event correlations between energy and zenith angle bins (i.e. double counting of SK events), the zenith distribution fit is done only in accordance with the fit first obtained for the SK and SNO spectral shapes alone ($\chi^2_{\text{SK}} + \chi^2_{\text{SNO}}$). The parameters for the SK energy scale, SK energy resolution, and ^8B spectral shape obtained from the $\chi^2_{\text{SK}} + \chi^2_{\text{SNO}}$ fit were used in the unbinned zenith angle fit.

The zenith fit was done with the same fitting tool that is used in the solar neutrino data extraction (solfit). In this fit, each SK event, with its proper energy and direction, was considered individually, i.e. the event distribution used was unbinned. A log likelihood that the event is a solar neutrino signal event was calculated for each SK event and integrated into a total likelihood number. One integral likelihood number was obtained while considering the matter effect of the earth's interior on the oscillations (i.e. with the day/night effect "turned on") and one while ignoring any matter effects in the earth (i.e. with the day/night effect "turned off"). Then $-\frac{1}{2}$ of the difference of the two resulting likelihood values was added to the initial χ^2 :

$$\chi^2_{\text{SK+SNO,final}} = \chi^2_{\text{SK}} + \chi^2_{\text{SNO}} - \frac{1}{2}(\mathcal{L}_{dn} - \mathcal{L}_o). \quad (5.24)$$

The $\Delta\chi^2$ map of this SK+SNO final fit is shown in Fig. 5.10. Now the LMA solution is the only allowed region at 96.4% c.l., and the LOW solution is ruled out at 98.9% c.l. The no-oscillation scenario is ruled out at the 6.0σ level. The best-fit ($\chi^2 = 33.8/36$ d.o.f.) neutrino oscillation model obtained from the fit to all the SK

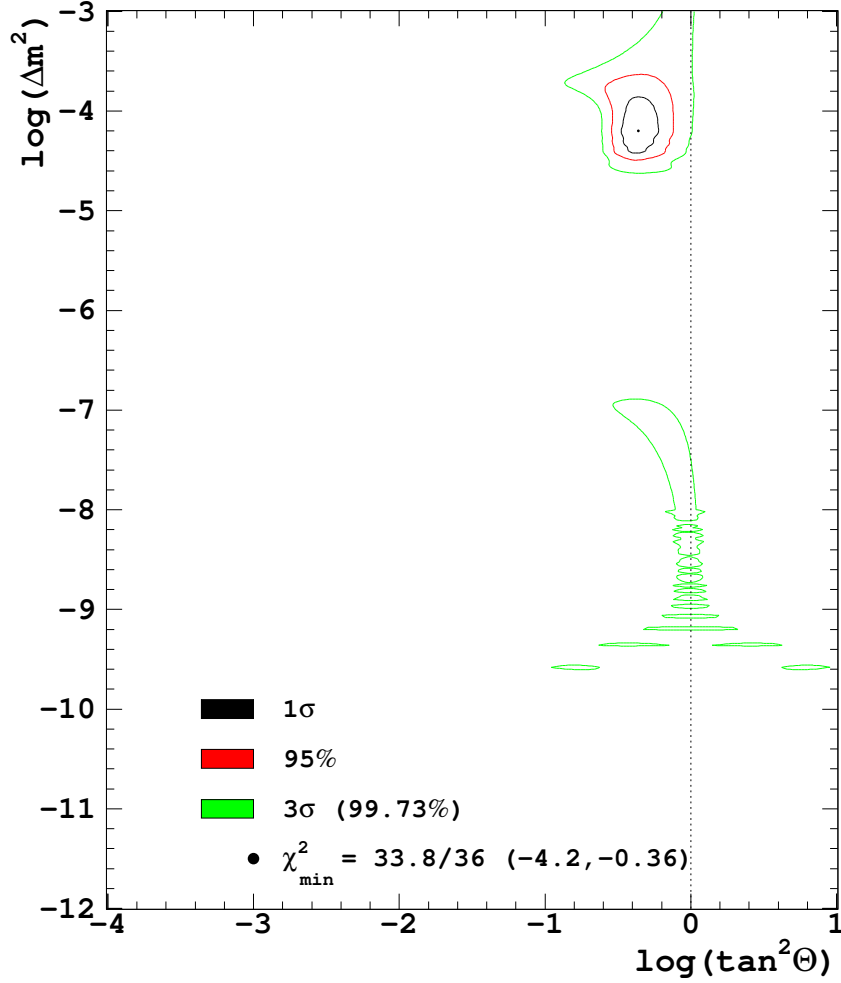


Figure 5.10: The χ^2 fit map of oscillation parameters for the SK and SNO energy spectra and SK zenith angle distribution.

and SNO data is:

$$\begin{aligned}
 \Delta m^2 &= 6.3_{-2.5}^{+7.5} \times 10^{-5} \text{ eV}^2 \\
 \tan^2 \theta &= 0.44_{-0.9}^{+0.14} \\
 \Phi_{b8} &= 1.08 \times \text{SSM} \\
 \Phi_{hep} &= 0.29 \times \text{SSM} .
 \end{aligned} \tag{5.25}$$

The uncertainties given on Δm^2 and $\tan^2 \theta$ are the extreme values of the two parameters in the 1σ region (black) in Fig. 5.10 around the χ^2_{\min} point. No errors can be given for the Φ_{b8} and Φ_{hep} parameters, because they were not scanned through a

range of values, but were, rather, analytically minimized.

5.3.5 Global Fit Result

Finally, adding the total neutrino rate information from the radio-chemical experiments (chlorine and gallium) to the SK+SNO final result, yields the global solar neutrino oscillation solution. The χ^2 function was the global fit then becomes:

$$\chi_{global}^2 = \chi_{SK+SNO,final}^2 + \chi_{Cl+Ga}^2, \quad (5.26)$$

and the $\Delta\chi^2$ map for the fit is shown in Fig. 5.11. Now the LMA region is the only believed global solution and is favored at 99.78% c.l., or just over 3σ . The no-oscillation scenario is ruled out at over 10σ in this case. The best-fit ($\chi^2 = 37.8/38$ d.o.f.) global solar neutrino solution is:

$$\begin{aligned} \Delta m^2 &= 6.0_{-2.4}^{+4.0} \times 10^{-5} \text{ eV}^2 \\ \tan^2\theta &= 0.40_{-0.07}^{+0.10} \\ \Phi_{b8} &= 1.12 \times \text{SSM} \\ \Phi_{hep} &= 0.30 \times \text{SSM}. \end{aligned} \quad (5.27)$$

The calculated uncertainties on Δm^2 and $\tan^2\theta$ are somewhat smaller than in the SK+SNO case, but the best fit point has not moved significantly. The best-fit values of the ^8B and hep neutrino fluxes are also only slightly shifted.

5.3.6 Adding the KamLAND Rate

The final chapter in the solar neutrino oscillation story is adding the recent anti-neutrino oscillation result from KamLAND [37]. KamLAND is a liquid scintillator neutrino detector in the same Kamioka mine in Japan. It is designed to detect anti-neutrinos from various Japanese nuclear reactors. It uses the inverse beta decay interaction ($\bar{\nu}_e + p \rightarrow e^+ + n$) in the detection of the anti-neutrinos, and its energy

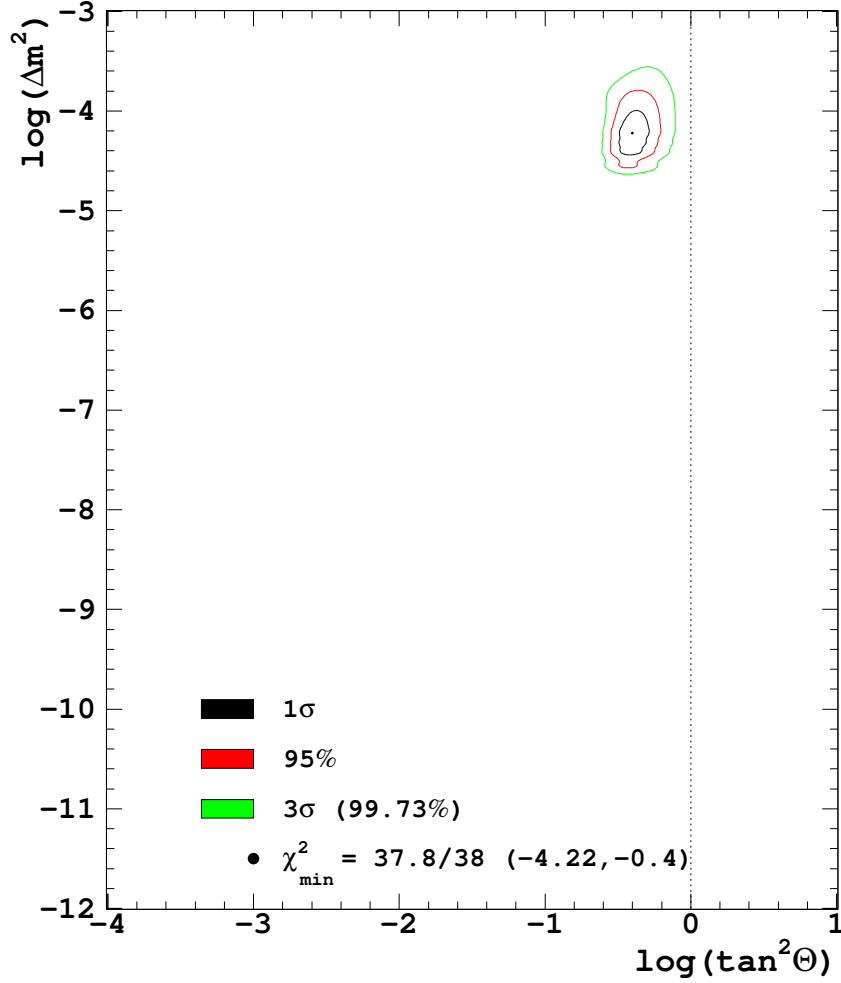


Figure 5.11: The $\Delta\chi^2$ map of oscillation parameters for the solar neutrino global fit (SK + SNO + zenith + Ga + Cl).

threshold is 1.8 MeV. The $\bar{\nu}_e$ flux at KamLAND is dominated by several reactors at an average distance of ~ 180 km.

It was shown by the KamLAND collaboration that the total measured $\bar{\nu}_e$ rate is smaller than the expected rate from the uranium and plutonium sources of the reactors [37]. The explanation, again, is neutrino oscillations. Fig. 5.12 shows the total rate fit of KamLAND data to the prediction of reactor anti-neutrino oscillations at the flux-averaged distance of 1.7433×10^5 m. Overlaid in the figure is the solar neutrino global result from Fig. 5.11. The oscillation probability and event rate were calculated by using the reactor $\bar{\nu}_e$ energy spectrum, $\lambda(E_\nu)$, given in Ref. [37], and

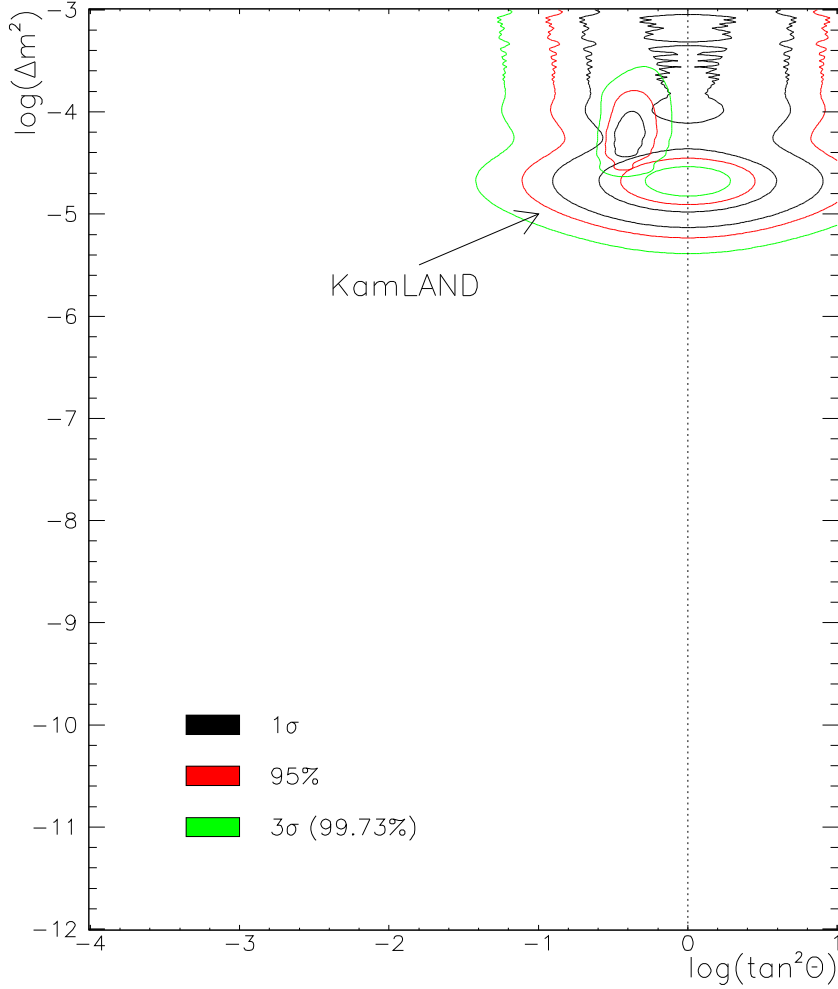


Figure 5.12: The $\Delta\chi^2$ map of oscillation parameters for the reactor neutrino oscillation fit of KamLAND rate, overlaid with the solar neutrino global result.

considering a simple anti-neutrino oscillation scenario in vacuum:

$$P_{\bar{\nu}_e \rightarrow \bar{\nu}_e} = 1 - \sin^2 2\theta \sin^2 \left(\frac{1.27 \Delta m^2 [\text{eV}^2] L_{ave} [\text{m}]}{E_\nu [\text{MeV}]} \right) \quad (5.28)$$

$$R = \int \lambda(E_\nu) P(E_\nu) dE_\nu.$$

In the figure, the KamLAND allowed regions are overlaid with the solar neutrino global result from Fig. 5.11. It is clear from the figure that the LMA parameter region is the only viable oscillation solution.

With the assumption that flavor oscillations in the anti-neutrino sector are equivalent to those in the neutrino sector, we can combine the two results. Adding the

KamLAND total rate fit to the solar neutrino global fit further narrows down the range of possible oscillation parameters, as shown in Fig. 5.13. The figure shows the neutrino oscillation $\Delta\chi^2$ map where the KamLAND rate fit χ^2 was added to the χ^2 of the solar neutrino global fit. Note that the range of the oscillation parameters in the figure is “zoomed in” from all previous similar figures.

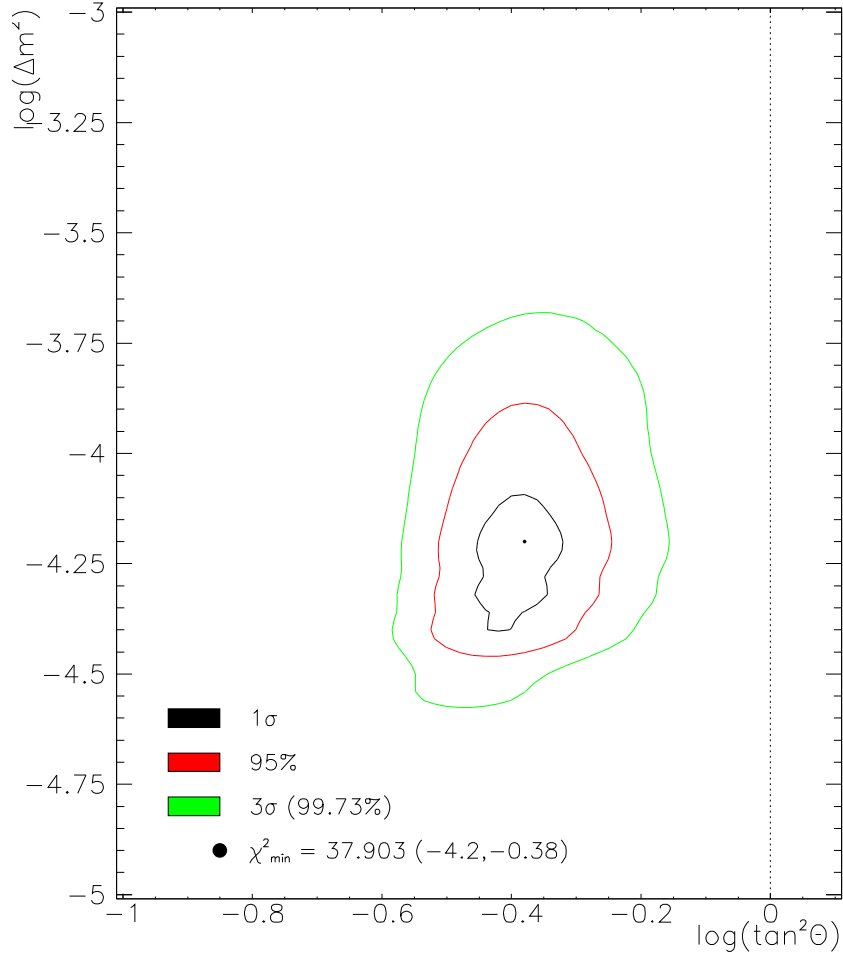


Figure 5.13: The $\Delta\chi^2$ map of the combined oscillation fit of the solar neutrino global result and the reactor anti-neutrino rate result.

The best-fit ($\chi^2 = 37.6/39$ d.o.f.) oscillation model is: $\Delta m^2 = 6.3_{-2.5}^{+3.2} \times 10^{-5} \text{ eV}^2$ and $\tan^2\theta = 0.42_{-0.09}^{+0.06}$, which is very similar to the best-fit model from the solar neutrino global fit. The figure shows that the LMA parameter region is greatly restricted and all of the other possible regions disappear at 99.99996% c.l., or 5.1σ .

5.3.7 Final Solar Neutrino Oscillation Result

Besides the total rate prediction, the KamLAND collaboration has also released a combined oscillation fit result from the total rate and the energy spectrum shape of the reactor anti-neutrinos. The $\Delta\chi^2$ map of the oscillation parameters from this KamLAND combined fit is shown in Fig. 5.14. This map was not calculated in this work, but was obtained directly from Ref. [38].

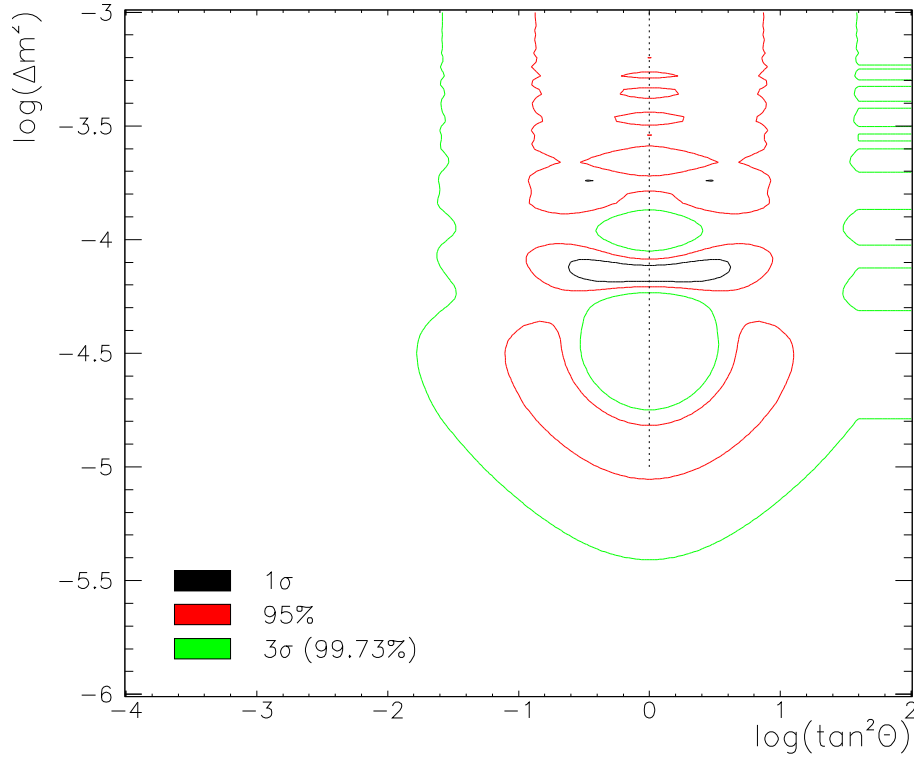


Figure 5.14: The total reactor anti-neutrino oscillation fit from KamLAND.

Simply adding the χ^2 values from this KamLAND combined fit to the χ^2 of the solar neutrino global $\Delta\chi^2$ map from Fig. 5.11, provides an improvement from the last result (Fig. 5.13) and yields the *final solar neutrino oscillation result*. The $\Delta\chi^2$ map of this final result is shown in Fig. 5.15. As shown in the figure, the previous LMA region has now been divided into LMA1 (upper) and LMA2 (lower). At 95% c.l., only the LMA2 region is allowed. This final result, thus, very tightly restricts the possible parameter range for solar neutrino oscillations, assuming the equivalence in

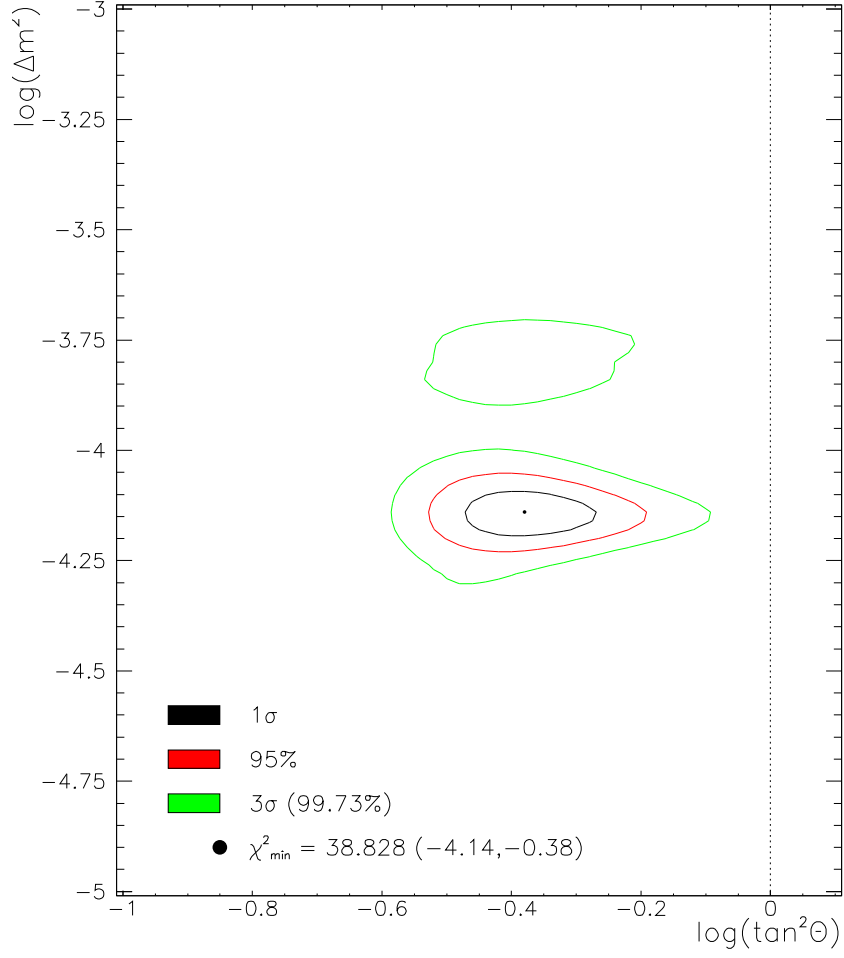


Figure 5.15: The $\Delta\chi^2$ map for the oscillation fit of the combination of the solar neutrino global result and the combined reactor anti-neutrino fit result (including total rate and spectral shape).

oscillations between the neutrino and anti-neutrino sectors.

The final solar neutrino oscillation best-fit solution is:

$$\begin{aligned}
 \Delta m^2 &= 7.2_{-0.6}^{+0.7} \times 10^{-5} \text{ eV}^2 \\
 \tan^2\theta &= 0.42_{-0.05}^{+0.11} \\
 \Phi_{b8} &= 1.12 \times \text{SSM} \\
 \Phi_{hep} &= 0.30 \times \text{SSM}.
 \end{aligned} \tag{5.29}$$

The 1σ range of the Δm^2 parameter has been significantly lowered from the global

solar result, while the similar range for $\tan^2\theta$ has remained similar. The best-fit ${}^8\text{B}$ and hep neutrino fluxes are identical to those in the global solar result, because naturally, they were not allowed to vary in the KamLAND fit. It is worth noting that the adding additional information to the SK+SNO fit has not shifted the best-fit oscillation model; it has only successively restricted the ranges of the allowed oscillation parameter values.

Finally, using this final best-fit oscillation model (Eq. 5.29), we can calculate the predictions for the solar neutrino fluxes for all of the existing solar neutrino detectors. This prediction is shown in Tab. 5.2, compared with the flux measurement as well as its SSM prediction for each detector. The Cl and Ga rate measurements, uncertainties and SSM predictions were taken from Tab. 2.3. SK's ${}^8\text{B}$ flux measurement and total uncertainty was taken from Eq. 4.25. SNO's ${}^8\text{B}$ flux measurement was calculated by integrating the total energy spectrum obtained from Ref. [30]. The total uncertainty of the SNO rate was calculated from the statistical and systematic uncertainties of the three contributions to SNO's total rate (CC, NC, ES) in Ref. [30]. For each detector, the model predictions were calculated for the dominant neutrino flux, shown in parentheses. As the table clearly shows, the final best fit solar neutrino oscillation model predicts the measured neutrino fluxes for each solar neutrino experiment, and completely resolves the solar neutrino puzzle.

A prediction of the distortions in the energy spectrum was also made with the final solar neutrino oscillation model. Fig. 5.16 shows these two predictions overlaid with the data. The top plot is for SK and the bottom for SNO. The figure shows that the best-fit model predicts minimal spectral distortions. The day/night flux asymmetry predicted for SK by this model is $A_{dn} = -0.015$, which is not statistically discernable with SK. Both of these predictions are consistent with the SK measurements.

Table 5.2: Neutrino flux predictions of the final best-fit solar neutrino oscillation model.

Solar experiment	BP2000 prediction	Flux measurement	$\Delta m^2 = 7.2 \times 10^{-5}$ $\tan^2 \theta = 0.42$
Chlorine (^8B)	$7.6^{+1.3}_{-1.1}$	2.56 ± 0.23	2.54
Gallium (pp)	128^{+9}_{-7}	74.7 ± 5.0	74.0
SK (^8B)	$5.05^{+1.01}_{-0.81}$	2.34 ± 0.08	2.24
SNO (^8B)	$5.05^{+1.01}_{-0.81}$	2.22 ± 0.11	2.03

NOTE.—The units for the chlorine and gallium rates are SNU, while for the SK and SNO rates the units are $10^6 \text{ cm}^{-2}\text{s}^{-1}$.

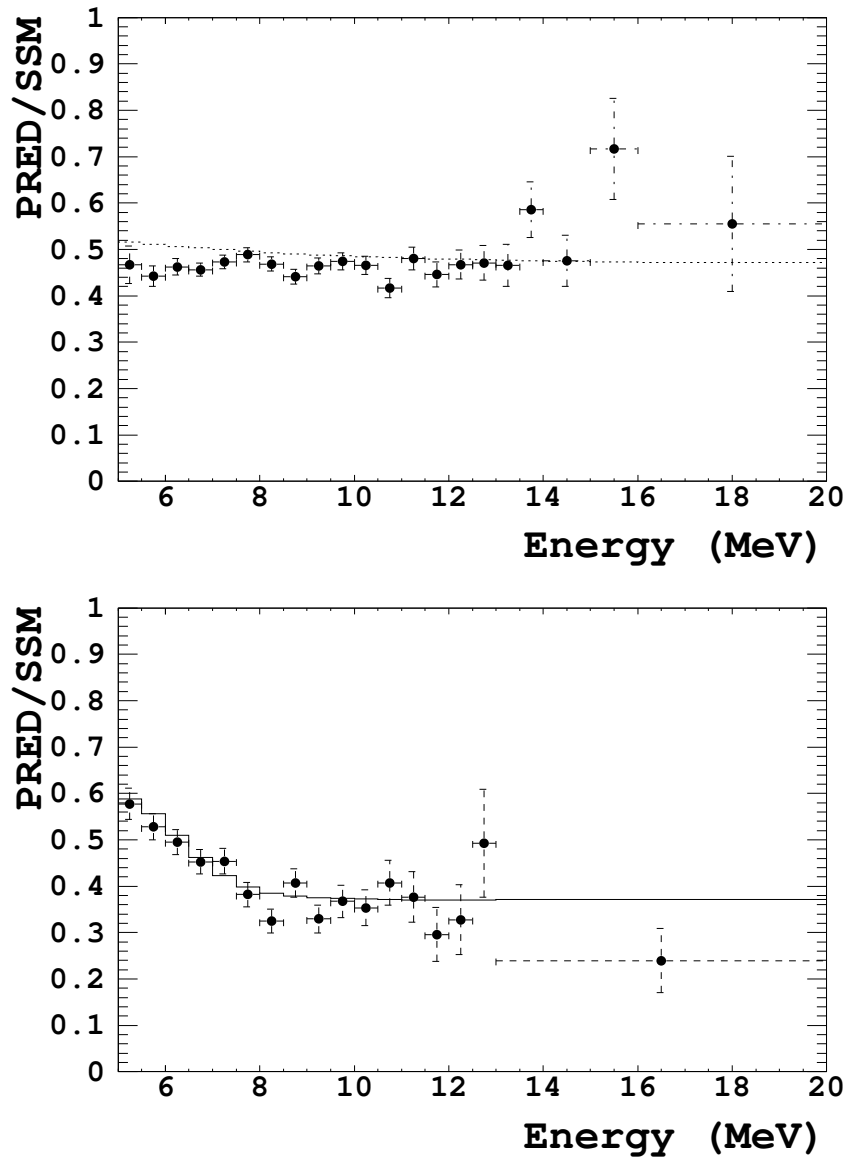


Figure 5.16: The predictions of the spectral distortions from the final solar neutrino oscillation model, obtained from the combined fit of the solar neutrino global result and the combined reactor anti-neutrino result (including total rate and spectral shape). The top plot shows SK spectrum and the bottom plot shows SNO spectrum

Chapter 6

Summary and Conclusions

After three decades of theories, experiments, and speculations, the famous, long-standing, experimentally well-established solar neutrino puzzle has finally been solved. What at first seemed like a deficit in the measured solar neutrino flux, has now become the conclusive evidence for solar neutrino flavor oscillations and, thus, further evidence for neutrino's finite mass.

The first evidence for neutrino flavor oscillations came from the Super-Kamiokande's analysis of the atmospheric neutrino data in 1998 [3], but through solar oscillation analyses presented in this work and others, it has now been shown that a similar flavor oscillation effect is responsible for decreasing the ν_e flux from the sun. While all previous experiments measured only ν_e , the modern neutrino detectors, like SK and SNO, capable of measuring all neutrino flavors, detected the full flux predicted by the Standard Solar Model [4]. This new result is, therefore, a confirmation of not only neutrino's finite mass, but also of the validity of the theoretical solar model.

Super-Kamiokande first made an attempt to discover smoking-gun evidence for solar neutrino flavor oscillations ($\nu_e \leftrightarrow \nu_\mu$) through distortions in the neutrino energy spectrum (due to the energy dependence of the oscillation probability) and an asymmetry in the day and night neutrino fluxes (due to the MSW effect in the earth's core). The lack of such strong evidence necessitated a more involved analysis and a

combination of all existing experimental results, with a goal of restricting the possible range of oscillation parameters (mass squared difference and neutrino mixing) to a single viable solution.

Firstly, a clever combination of SK's total ($\nu_e + \nu_\mu + \nu_\tau$) rate and SNO's ν_e rate demonstrates, independent of an oscillation model, that neutrino oscillations in fact decrease the ν_e flux, by some of the ν_e oscillating to ν_μ or ν_τ , and create an apparent solar neutrino deficit. Secondly, the combination of the full SK and SNO data sets further favors neutrino oscillations as the explanation of the apparent deficit and limits the range of possible oscillation models to the LMA solution (at 96.4% c.l.). This SK+SNO combination rules out the no-oscillation scenario at 6.0σ . Thirdly, the global solar neutrino result, obtained by adding results from all current solar neutrino experiments, firmly establishes the solar neutrino oscillation scenario as reality (no-oscillations ruled out at over 10σ), and more tightly restricts the oscillation parameter space (LMA is favored at 99.78% c.l.). The prediction of the Standard Solar Model is also confirmed by this global result: the resulting flux of ^8B neutrinos is $1.12_{-0.12}^{+0.12} \times \text{SSM}$. Finally, adding the anti-neutrino oscillation result from KamLAND to the solar neutrino global result confirms the solar result and restricts even further the LMA oscillation parameter range. The final best-fit oscillation model, which includes all of the solar neutrino and reactor anti-neutrino data, is: $\Delta m^2 = 7.2 \times 10^{-5} \text{ eV}^2$ and $\tan^2\theta = 0.42$.

With the theory of solar neutrino flavor oscillations being firmly established as the explanation of the apparent solar neutrino flux deficit, the field of solar neutrino research is perhaps all but closed. All that remains is further independent confirmation of the current result, and a higher level of precision in the measurements, which is obtained by more statistics. But besides virtually concluding the solar neutrino field, the present result has one other very important accomplishment, and that is opening the door further for physics beyond the standard model. What was started

first by the Super-Kamiokande atmospheric neutrino result is now established further by the solar neutrino result: the fact that all the experimental results point to, and the reality that no one can any longer ignore, is that neutrinos have a finite mass and that there is a need for a more comprehensive theory of particle physics beyond the standard model, that would systematically incorporate this new paradigm.

Bibliography

- [1] R.N. Mohapatra, P. B. Pal, Massive Neutrinos in Physics and Astrophysics, second edition, Singapore: World Scientific Publishing (1998).
- [2] J.N. Bahcall, Neutrino Astrophysics, New York: Cambridge University Press (1989).
- [3] Y. Fukuda, et al., Phys. Rev. Lett. 81, 1562 (1998).
- [4] J.N. Bahcall, M.H. Pinsonneault, and S. Basu, ApJ 555, 990 (2001); many numerical tables from the paper can be found at: <http://www.sns.ias.edu/jnb/>
- [5] J.N. Bahcall, S. Basu, and M.H. Pinsonneault, Phys. Lett. B 433, 1 (1998); J.N. Bahcall, M.H. Pinsonneault, Rev. Mod. Phys. 67, 781 (1995); J.N. Bahcall, M.H. Pinsonneault, Rev. Mod. Phys. 64, 885 (1992).
- [6] B.T. Cleveland et al., ApJ 496, 505 (1998).
- [7] K.S. Hirata et al., Phys. Rev. D 44, 2241 (1991); Y. Fukuda et al., Phys. Rev. Lett. 77, 1683 (1996).
- [8] M. Koshiba, ICRC 2003 (invited talk), Tsukuba, Japan.
- [9] J.N. Abdurashitov et al., Phys. Lett. B 328, 234 (1994); J.N. Abdurashitov et al., Phys. Rev. C 60, 055801 (1990); J.N. Abdurashitov et al., J.Exp.Theor.Phys. 95 181-193 (2002).

- [10] W. Hampel et al., Phys. Lett. B 388, 364 (1996);
P. Anselmann et al., Phys. Lett. B 342, 440 (1995);
M. Altmann et al., Phys. Lett. B 490 16 (2000).
- [11] E.G. Adelberger et al., Review of Modern Physics 70, 1265 (1998).
- [12] N. Hata and P. Langacker, Phys. Rev. D 50, 632 (1994);
N. Hata and P. Langacker, Phys. Rev. D 56, 6107 (1997).
- [13] S. Fukuda et al., Nucl. Instrum. Methods Phys. Res. Sect. A 501, 418 (2003).
- [14] Matthew S. Malek, *A Search for Supernova Relic Neutrinos*. PhD Thesis, State University of New York, Stony Brook, 2003.
- [15] Becker-Szendy, R. et al. 1995, ApJ, 444, 415
- [16] Erik K. Blaufuss, *Study of the Energy Spectrum of Solar Neutrinos Above 5.5 MeV*. PhD Thesis, Louisiana State University, 2000.
- [17] Nobuyuki Sakurai, *Constraints of the neutrino oscillation parameters from 1117 day observation of solar neutrino day and night spectra in Super-Kamiokande*. PhD Thesis, ICRR, University of Tokyo, 2000.
- [18] Yusuke Koshio, *Study of Solar Neutrinos at Super-Kamiokande*. PhD Thesis, ICRR, University of Tokyo, 1998.
- [19] E.K. Blaufuss et al., Nucl. Instrum. Meth. A 458, 638 (2001).
- [20] Zoa Conner, *A Study of Solar Neutrinos Using the Super-Kamiokande Detector*. PhD Thesis, University of Maryland, 1997.
- [21] Hirokazu Ishino, *Measurement of the Solar Neutrino Spectrum at Super-Kamiokande*. PhD Thesis, University of Tokyo, 1999.

- [22] C. Caso et al., The European Physical Journal C 3, 1 (1998).
- [23] T. Suzuki, D.F. Measday, and J.P. Roalsvig, Phys. Rev. C 35, 2212 (1987).
- [24] S. Matsuno et al., Phys. Rev. D 29, 1 (1984).
- [25] C.E. Ortiz et al., Phys. Rev. Lett. 85, 2909 (2000).
- [26] J.N. Bahcall, M. Kamionkowski, A. Sirlin, Phys. Rev. D 51, 6146 (1995).
- [27] J.N. Bahcall et al., Phys. Rev. C 54, 411 (1996).
- [28] GEANT Detector Description and Simulation Tool, *Cern Program Library W5013* (1994).
- [29] A. Suzuki et al., Nuclear instruments and Methods A 329, 299 (1993).
- [30] Q.R. Ahmad et al., Phys. Rev. Lett. 89, 011301 (2002).
- [31] The SNO Collaboration, Nucl. Instr. and Meth. A 449, 172 (2000).
- [32] G.L. Fogli, E. Lisi, D. Montanino, A. Palazzo, Phys. Rev. D 64, 093007 (2001).
- [33] F.L. Villante, G. Fiorentini, E. Lisi, Phys. Rev. D 59, 013006 (1998).
- [34] K. Kubodera, S. Nozawa, Int. J. Mod. Phys. E 3, 101 (1994);
<http://www.sns.ias.edu/~jnb/>
- [35] <http://www.sno.phy.queensu.ca/sno/prlwebpage/>
- [36] G.L. Folgi et al., Phys. Rev. D 66, 053010 (2002).
- [37] K. Eguchi et al., Phys. Rev. Lett. 90, 021802 (2003).
- [38] A. Ianni, J.Phys. G29, 2107 (2003).